國立臺灣大學物理學研究所

博士論文

Department of Physics

College of Science

National Taiwan University

Doctoral Dissertation

以電漿波導為基礎所發展的多波長與注入放大Ｘ光雷射

Development of Multi-Line and Seeded Waveguide-Based Soft X-Ray Lasers

林秉勳

Ping-Hsun Lin

指導教授：汪治平 博士

陳賜原 博士

林俊元 博士

Advisor: Jyhpyng Wang, Ph.D.

Szu-Yuan Chen, Ph.D.

Jiunn-Yuan Lin, Ph.D.

中華民國 99 年 1 月

January, 2010


國立臺灣大學
敦品勵學・愛國愛人

Development of Multi-Line and Seeded Waveguide-Based Soft-X-Ray Lasers

Ping-Hsun Lin

January 26, 2010


國立臺灣大學
敦品勵學・愛國愛人

國立臺灣大學（碩）博士學位論文
口試委員會審定書

以電漿波導為基礎所發展的多波長與注入放大 X 光雷射

Development of Multi-Line and Seeded Waveguide-Based Soft X-Ray Lasers

本論文係林秉勳君（d94222018）在國立臺灣大學物理學系、所完成之碩（博）士學位論文，於民國 99 年 1 月 20 日承下列考試委員審查通過及口試及格，特此證明

口試委員：

汪治平 （簽名）	
（指導教授）	
陳賜原	黃升龍
林俊元	潘犀靈
施宙聰	


國立臺灣大學
敦品勵學・愛國愛人

誌謝

首先感謝我的指導教授汪治平老師，汪老師嚴謹認真的教導，不僅使我學業上有所成長，而且幫助我以更正確的態度來學習科學。我也要特別感謝陳賜原老師，帶領我認清科學研究的本質，並逐步培養建立我的專業能力，讓我得以順利完成各項實驗工作。而陳老師堅定負責的處事態度以及不輕言放棄的精神，更特別值得我去學習效法。另外也謝謝林俊元老師熱心與不厭其煩的教導，彌補我許多專業知識上的不足。同時也感謝朱旭新老師的鼓勵與教導。

六年的實驗室生涯，所有工作都是建築在許多人同心協力的努力下才得以完成。首先感謝小胖周明昌的鼎力相助，多年來 X 光雷射組成員的革命情感以及絕佳的實驗默契，共同克服了種種困難與挑戰。感謝陳彥穆以及白植豪一路來的相互合作打氣，一起體驗從菜鳥到畢業的心路歷程。也謝謝黃善瑜學長、楊蘭昇學長、謝長村學長、何彥政、洪德昇與陳惠群的幫忙。另外，當然也要謝謝陳秉寬、嚴治平、江明哲、曾柏彰、劉奕成、蔡坤達、林祈安、黃章泰、黃茹萍、許娜琦等各位學弟妹的幫忙，也讓我們彼此一同成長。

感謝女友穎亭的相知相伴，總是在昏天暗地的實驗中提供我陽光般的溫暖以及無比的動力，為枯燥的研究生活點綴繽紛的色彩，也讓我擁有最豐富且專屬的幸福資產。另外也謝謝妹妹以及家人的關心和照顧，供給我永不間斷的精神食糧。

最後要將本論文獻給我最敬愛的母親，謝謝她無怨無悔的付出與照顧，永遠在身旁給予我百分之百的支持與鼓勵，讓我得以選擇並堅持自己想要的人生道路，對母親這份感念的心將是驅動我不斷向前邁進的力量。


國立臺灣大學
敦品勵學・愛國愛人

Contents

Abstract

It has been nearly half a century since the invention of lasers, the use of coherent light has become an indispensable part of our world, such as optical communications, precision measurements, optical memories, and medicine. Rapid progress in technology has led to the development of coherent lights that operate in short-wavelength regions, examples of such light sources include soft x-ray lasers. The use of soft x-ray lasers has considerable potential from the viewpoint of pioneering research in various scientific fields like high-resolution microscopy and holography, dense plasma measurement, and nano-lithography; visible lasers are inadequate for these purposes. With the advent of high-power short-pulse lasers, especially the high-repetition-rate terawatt lasers based on the chirped-pulse amplification technique, it is now possible to generate ultrashort coherent soft x-rays with a much lower cost and small size. An ultrashort high-intensity laser pulse combined with the optical-field-ionization (OFI) collisional-excitation mechanism can be used to produce a suitable x-ray gain medium: highly ionized plasma. In addition, the ultrashort feature of the pumping source can overcome the problem of the short duration of the gain in the x-ray region. Considering the size and cost, the use of a table-top, high brightness, soft x-ray laser is advantageous as compared to synchrotron radiations or x-ray free electron lasers.

This thesis first reports the development of an OFI collisional-excitation soft x-ray laser that uses an optically preformed plasma waveguide. Using a 9-mm-long pure krypton plasma waveguide prepared by the axicon ignitor-heater scheme, Ni-like Kr lasing at a wavelength of 32.8 nm can be enhanced by 400 times relative to the case without the plasma waveguide. An output level of 8×10^{10} photons/pulse can be obtained at an energy conversion efficiency of 2×10^{-6}. Then, under the same configuration of the pump and waveguide-forming pulses, strong Pd-like xenon lasing and Ne-like argon lasing were realized at wavelengths of 41.8 nm and 46.9 nm, respectively. In addition to the main lasing lines for Ni-like krypton and Ne-like

argon, other lasing lines are also observed; this is indicative of a strong enhancement effect and a large gas density in the plasma waveguide. With a Kr/Ar mixed gas multi-species parallel x-ray lasing was also demonstrated, showing the capability of generating multi-line soft x-ray lasers by using the optically preformed plasma waveguide. In order to gain a better understanding of waveguide-based soft x-ray lasers and control them suitably, extensive experimental results on the pump-energy dependence, density dependence, and effects of parameters that control the waveguide fabrication were studied in detail. Finally, in order to realize further improvements in the optical qualities of the soft x-ray laser, a strongly saturated waveguide-based OFI soft-x-ray laser seeded by high harmonic generation (HHG) was demonstrated for Ni-like Kr lasing at a wavelength of 32.8 nm. HHG is produced from the nonlinear interaction between intense laser and gas atoms. During this process, electrons that are ionized from the gas atoms oscillate with the laser field; subsequently, they recombine with their parent ions and emit high-energy photons. The emissions from different atoms add constructively and thus retain good spatial and temporal coherence. As compared to laser seeded with only spontaneous emission, the divergence of seeding with HHG is greatly reduced from 4.5 mrad to 1.1 mrad, which is about the same as that of the HHG seed. The amplified HHG seed pulse also shows enhanced spatial coherence and controlled polarization. Moreover, seeded x-ray lasers do not suffer from timing jitter relative to the pump laser; this is important for pump-probe applications. We believe that the integration of high-harmonic seeding, optically preformed plasma waveguide, and OFI pumping forms one of the optimal archetype of a high-repetition-rate, high-intensity, ultrashort-pulse soft x-ray laser.

keywords: EUV laser, Soft x-ray laser; Seeded soft x-ray laser; Optical-field ionization; Plasma waveguide; High-harmonic generation.

摘要

雷射的發明已將近半個世紀，這種高同調性光源對於人類的影響可說是無遠弗屆，從光通訊、精密量測、光學儲存與讀寫裝置乃至於醫療美容，無一不深植於現代人類的生活。然而隨著科技的進步，將雷射光推向更短波長的時代已經來臨，如軟 X 光雷射的發展。軟 X 光雷射可被應用在半導體製程、材料分析、高密度電漿探測以及高解析度顯微術等多方面，其短波長和符合許多元素共振吸收的特性是可見光雷射所無法取代。在 X 光雷射的發展上，高發射頻率、高尖峰功率、短脈衝的桌上型雷射系統的發明無疑帶來一股新動力。以短脈衝高功率桌上型雷射搭配光場游離碰撞激發機制，可以產生軟 X 光波段所需要的雷射增益介質：高游離態電漿，並且可以克服 X 光輻射生命週期短的問題。這種技術所發展的 X 光雷射比起同樣產生高同調性 X 光的同步輻射光和 X 光自由電子雷射，具有體積小、成本低的優點，是比較符合實際應用上所需求。

本論文的工作首先是協助發展出以全光學式電漿波導為基礎的光場游離碰撞激發的軟 X 光雷射。利用電漿波導的技術，可以使產生 X 光雷射增益的紅外光激發雷射克服繞射與游離發散的限制，將操作氣體密度提高一個數量級，並使有效增益長度延伸數倍。因此，我們成功地將 32.8 奈米類鎳氪離子 X 光雷射輸出大幅增加四百倍並達到飽和，轉換效率則達到 2×10^{-6}。接著將這種技術推廣到不同的氣體靶材上，用來分別產生 41.8 奈米類鈀氙離子與 46.9 奈米類氖氬離子等不同波長的 X 光雷射，甚至還利用氪氣與氬氣混合氣體來製造出雙波長同時輸出的 X 光雷射，使得我們的 X 光雷射可以在應用上更加豐富多變。另一方面，我們透過研究 X 光雷射輸出對不同控制參數的變化，藉此深入了解此種 X 光雷射的特性，進而掌握對它的控制調變能力。在成功地提高 X 光雷射輸出後，我們希望進一步提升 X 光雷射的光學品質。所以我們利用一道線偏振短脈衝雷射光游離氬原子外層電子，電子在線性震盪電場作用下回撞原本離子，與之結合並釋放出位於 X 光波段的高階諧波，其為具有良好時空波形的短脈衝，特別適合做為 X 光雷射放大器的種子脈衝。之後經由時間、空間和頻譜上精密的微調，將高階諧波注入到以電漿波導為基礎的 X 光雷射放大器來放大。透過這種注入放大的機制，我們成功地產生高同調性、小發散角以及具有線偏振性質的 X 光雷射。我們相信透過高階諧波、電漿波導與光場游離碰撞激發機制這三種方式的結合，可以提供未來產生短脈衝、高強度、高光學品質 X 光雷射的一個重要參考原型。


國立臺灣大學
敦品勵學・愛國愛人

List of Figures

Chapter 1

Introduction

1.1 Ultrashort Coherent Soft X-Ray Sources

Since Wilhelm Roentgen discovered the x-ray in 1895 [1], this so-called "unknown" radiation has been a powerful tool in many areas, ranging from physics, chemistry, life science, and medicine. Laser, another astonishing invention in the history of science, was demonstrated in 1960 by Ted Maiman [2]. Since then the use of coherent light has become an indispensable part of our world, with applications such as optical communications, precision measurements, optical storages and even entertainment, playing a trillion-dollar role in the global economy [3]. Recently, the rapid progress in technology has opened an opportunity to combine the x-ray and laser technology, taking advantage of the short wavelength and laser-like quality to create ultrashort coherent x-ray sources.

Before proceeding with the introduction of these coherent x-ray sources, it is necessary to define the spectral range of x-rays. Figure 1.1 shows portion of the electromagnetic spectrum extending from the vacuum ultraviolet (VUV) to the x-ray region, with wavelengths across the top [4]. The spectral regions from long to short wavelength are the VUV, the extreme ultraviolet (EUV/XUV), soft x-rays, and finally hard x-rays. Traditionally soft x-ray region is considered to begin at about 300 Å and end at 2 Å. However, soft x-ray is also defined as a broader range which extends to 700 Å [5, 6] and overlaps with the EUV region. The subject of this thesis focuses on this soft x-ray/EUV spectral range. In the regime of short wavelength, it is traditional

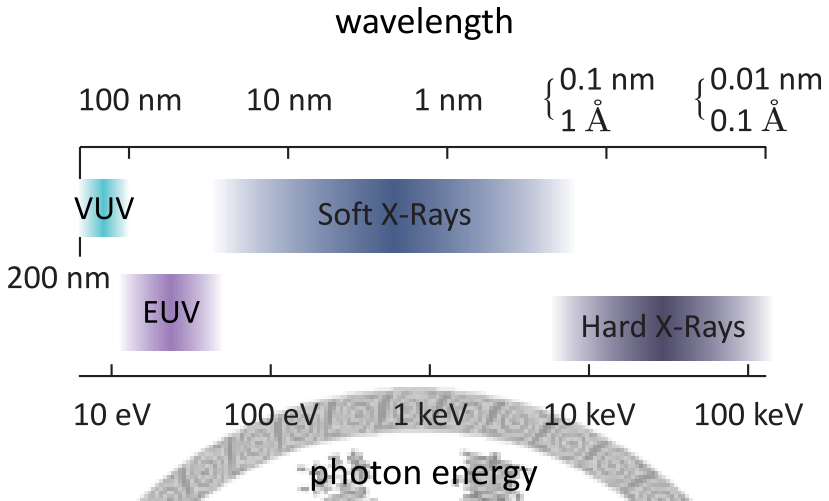

Figure 1.1: Illustration of the electromagnetic spectrum extending from the VUV to the x-ray region.

and practical to use the photon energy $h\nu$ in eV units as a label. Through the relation $\lambda = c/\nu$, the photon energy can be represented as

$$h\nu = \frac{1240}{\lambda[\text{nm}]}\ \text{eV}\,, \tag{1.1}$$

where λ is the wavelength, c is the light speed in vacuum, ν is the frequency, h is the Planck constant. The photon energy is indicated by the lower scale in Fig 1.1.

Ultrashort coherent soft x-ray sources are advantageous in various scientific research. The short wavelength make them practical tools for high-resolution microscopy, holography, nano-lithography and the diagnosis of high-density plasma. With the intense and ultrashort features, they may also open up extreme, unexplored regimes, such as x-ray nonlinear optics, time-resolved x-ray diffractometry of biological and inorganic materials, and medical diagnostics.

In general, ultrashort coherent soft x-ray sources can be divided into three categories: (1) high harmonic generation (HHG), (2) soft x-ray laser (SXRL), and (3) x-ray free electron laser (X-FEL). They are developed based on different experimental approaches, and each source has distinct properties on output energy, pulse duration, spatial and temporal coherence, and spectral range.

High harmonic generation occurs when a femtosecond laser pulse with a

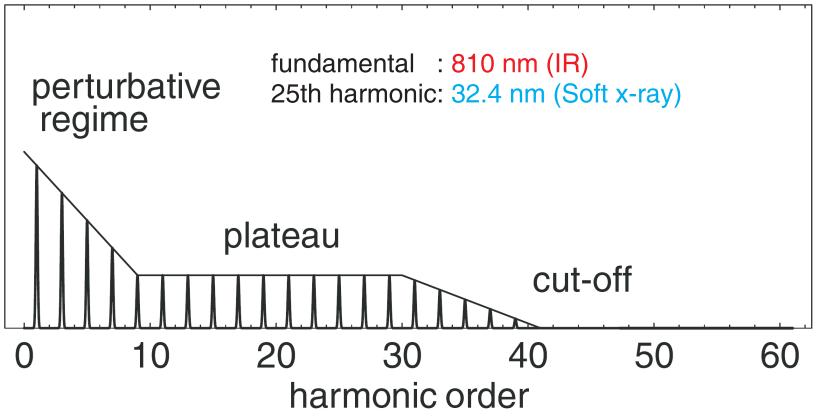

Figure 1.2: Typical high-harmonic spectrum. The spectrum can be divided into three parts: the perturbative regime at low orders, the plateau for intermediate orders, and the cutoff at the highest orders (from Ref[1]).

moderate intensity (typically 10^{14} - 10^{15} W/cm^2) is focused on gas atoms. During the process, the freed electrons, ionized from the atoms, oscillate with the laser field, then recombine with their parent ions and emit high-energy photons. The emissions from different atoms add constructively and retain the good spatial and temporal coherence. The full harmonic spectrum usually consists of the odd harmonics of the fundamental laser frequency and can reaches down to the XUV and soft x-ray range [7], as shown in Figure 1.2 (from [8]). The intensities of high harmonics fall off rapidly at the first several orders, then appear to form a plateau, and drop sharply at the cutoff order. High harmonic generation has an ultrashort pulse duration from sub-10-femtoseconds to attoseconds [9] due to its broad bandwidth ($\Delta\lambda/\lambda \approx 10^{-2}$), but has a limited energy in the nJ range [10]. However, HHG can be produced by using a table-top laser source, and the setup is relatively simple.

The soft x-ray laser, like the visible lasers, is based on the creation of a population inversion between two atomic levels to allow the amplification radiation by stimulated emission. Therefore the soft x-ray laser has a discrete spectrum, and the specific wavelength depends on the energy difference between the lasing levels. In the soft x-ray region, highly ionized plasma is chosen as the lasing medium, which is generated from the solid or gas target irradiated by a high-power laser, or high-voltage discharge in a capillary. Recently, the rapid advances in pump sources including the development of multiterawatt table-top laser systems based on chirped pulse amplification and fast capillary discharges capable of generating highly ionized plasma

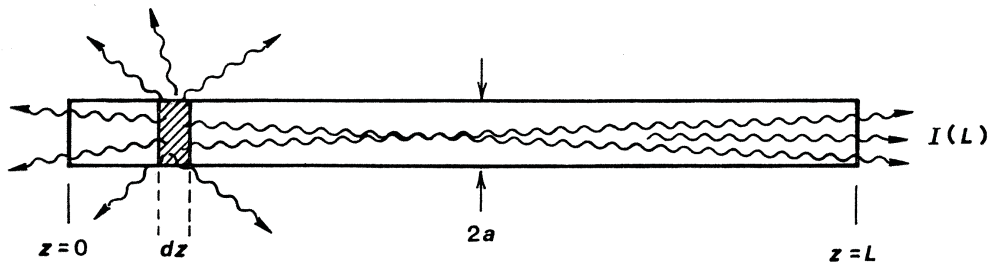

Figure 1.3: Schematic of an amplified spontaneous emission laser (from Ref[11]).

columns with very high uniformity and long length, push the soft x-ray lasers toward higher intensity and compact size. Several novel mechanisms, such as optical-field-ionization collisional excitation and grazing incidence pumping, greatly reduce the pumping energy and raise the operation rate of the soft x-ray lasers to meet the practical requirements. These developments provide a promising future for table-top high-repetition-rate soft x-ray laser sources. However, soft x-ray lasers have relatively high brightness due to the high monochromaticity ($\Delta\lambda/\lambda \approx 10^{-4}$) and short pulse duration (few to tens of picoseconds). The pump energy required for general x-ray lasers is ranging from few hundred millijoules to few hundred joules, depending on pumping mechanisms. Due to the limitation of x-ray optics, the soft x-ray laser is generated from the amplified spontaneous emission (ASE), in which the amplification starts from the randomly distributed spontaneous emission, and thus have partially spatial coherence. Figure 1.3 (from [11]) shows the illustration of an ASE laser.

The x-ray free-electron laser (X-FEL) [12, 13] is often referred to as the fourth-generation synchrotron radiation. They can provide a peak spectral brightness eight orders of magnitude higher than the storge-ring synchrotron sources. Unlike the general x-ray lasing via bound-electron transition, free-electron laser replace the lasing medium by a relativistic electron beam which freely move through a magnetic structure, called undulator, thus in term free electron. Figure 1.4 (from [14]) shows the illustration of an x-ray free-electron laser. Initially all electrons only emit incoherent spontaneous radiation. Through the interaction of this radiation and the electrons, a periodic charge density modulation is induced in the electron bunches, called microbunching. The period in the microbunches is equal to one resonant radiation wavelength, then all electrons begin emitting radiation in phase. This results in an exponential increase of the radiation intensity along the undula-

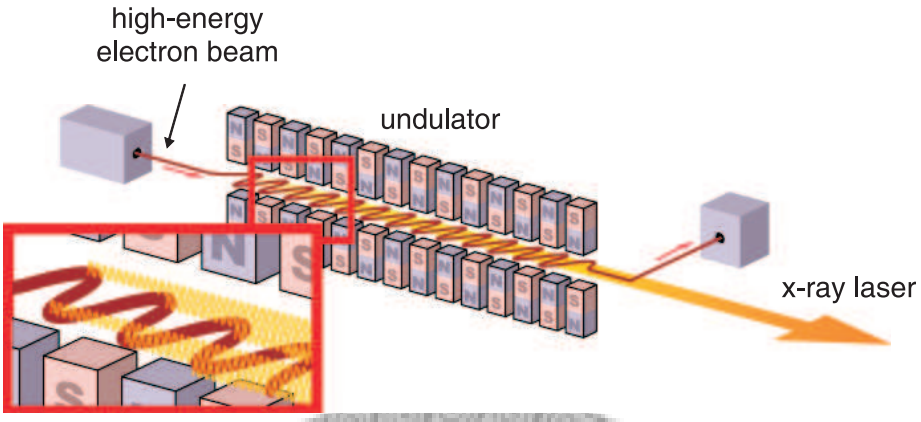

Figure 1.4: Illustration of an x-ray free-electron laser (from Ref[14]).

tor, leading to the laser-like properties. Since the radiation is amplified from incoherent spontaneous emission, such free-electron laser is also called self-amplified spontaneous emission (SASE) X-FEL. The resonant wavelength can be written as

$$\lambda_{ph} = \frac{\lambda_u}{2\gamma^2}(1 + \frac{K^2}{2}) \tag{1.2}$$

with

$$\gamma = \frac{E}{m_e c^2}$$

and

$$K = \frac{eB_u\lambda_u}{2\pi m_e c}$$

, where E is the electron energy, m_e the electron mass, e the electron charge, c the light speed in vacuum, λ_{ph} the undulator period, and B_u is the peak magnetic filed in the undulator. Unlike soft x-ray lasers where the wavelength is determined by the energy levels of lasing species, the wavelength of X-FEL can be varied continuously with the magnetic field or the electron energy, and X-FEL gives the possibility to achieve very short wavelengths at high electron energies. In addition to the short duration (about tens of femtoseconds), X-FEL has excellent optical qualities, such as low divergence, polarization, and high spatial coherence. However, for a SASE X-FEL, the microbunching takes place independently in different parts of the bunch and limits the temporal coherence of the radiation.

In summary, high harmonic generation has a much shorter pulse duration due to its broad bandwidth, making it more suitable for pump-probe experiments that requires much higher time resolution. Nevertheless, this in

turn results in a much lower spectral density. Its output energy is the lowest among the three x-ray sources. Soft x-ray lasers are favored by applications that require narrow bandwidth, such as x-ray diffraction, resonant excitation, and photoelectron spectroscopy. It provides higher energy than HHG, but has a poorer spatial coherence. X-ray free electron laser can provide more intense x-ray pulses with short pulse duration, but it is costly and much less accessible. Each of these coherent x-ray sources has its own advantage, and the best choice depends on the nature of the application. Recently, a straightforward idea is to use HHG to seed into the soft x-ray laser or x-ray free electron laser, thus combining the high beam quality of HHG with the high output energy of soft x-ray lasers or X-FELs to generate a high-intensity highly coherent ultrashort soft x-ray source.

1.2 Soft X-Ray Lasers

1.2.1 Introduction to Soft X-Ray Lasers

The pursuit for x-ray lasers begun immediately after Maiman demonstrated the first laser in 1960. However, two problems hindered the initial development of soft x-ray lasers. The first one is the lack of high reflective mirrors in the x-ray region, making x-ray laser cannot be operated efficiently in a cavity-like oscillator that is commonly used in the visible lasers. Secondly, the upper-level lifetime of soft x-ray lasers is so short that sets a limitation on amplification in a cavity. Therefore, soft x-ray lasers are usually operated at amplified-spontaneous-emission (ASE) regime with a single-pass or double-pass amplification, or so-called mirrorless amplification, and thus need a large gain-length product. Moreover, the power density necessary to obtain a given gain coefficient scales with the pumping wavelength as λ^{-5} or λ^{-4} [15], depending on the broadening mechanism of the lasing medium. Hence, the pump power required for lasing at soft x-ray wavelengths is often dramatically larger than that for a visible laser. A simple estimate shows that a saturated ASE soft x-ray laser at 50 nm requires a pump power density 10^7 times larger than that for a 500 nm green laser [15]. Highly ionized closed-shell ions is chosen as the lasing medium for soft x-ray lasers. The closed shell ensures the ground-state ions to have a high ionization energy, and thus make them stably exist with a large abundance in the plasma. In additions, the inner-shell electron transition from a highly-ionized atom can provide high-energy photons in the x-ray region.

The first x-ray lasers were demonstrated in 1985 [16, 17] by using collisional-excitation and recombination schemes, respectively. At that time, the most powerful laser (energy on the order of kJ), called Nova, was used to meet the high energy density requirement for x-ray lasers. Thereafter, tremendous progress was made in output, beam qualities, compactness, and repetition rate of soft x-ray lasers. The latter two features are particularly important for practical applications. Nevertheless, the invention of high-power laser systems plays an important role in the development of soft x-ray lasers. Because the parameters of the driving laser pulse, in particular the peak intensity and pulse duration, primarily control the space and time evolution of the plasma in the density, temperature, and ionization stage, thus affect the main characteristics of the soft x-ray laser beam. They also determine more practical features such as the cost, scale, and even repetition rate of the soft x-ray laser system. Hence, the progress of x-ray laser research is always closely linked to the development of high-power laser technology.

Other excitation schemes have also been proposed, including photon ionization pumping by thermal x-ray sources [18, 19] or resonant photo-pumping by specific x-ray line emissions [20]. These schemes provide the potential advantage of yielding a lasing wavelength of < 2 nm. However, they have not yet been experimentally demonstrated. The most widely used classification is by the pumping scheme, and Fig. 1.5 shows such a classification of x-ray lasers. Among all, the two major schemes, collisional excitation and recombination, will be addressed in the following sections.

1.2.2 Collisional-Excitation Soft X-Ray Lasers

A obvious feature of currently operational x-ray lasers is that they are all based on the collisional-excitation pumping scheme. The collisional-excitation scheme has already been used in generation of the visible or near-ultraviolet lasers, such as the cw argon ion and krypton ion lasers [21, 22]. Following the success in the development of these lasers at long wavelengths, this pumping scheme is further applied to the soft x-ray region. In general, the pumping process can be illustrated with the energy-level diagram of Figure 1.6. Initially the atoms of element X are ionized to the $i+$ ions at the ground state o, then the ions are collisonally excited to the upper state u by hot electrons (hundreds of eV typically), as shown in the equation [4]

$$X_o^{i+} + e \rightarrow X_u^{i+}. \tag{1.3}$$

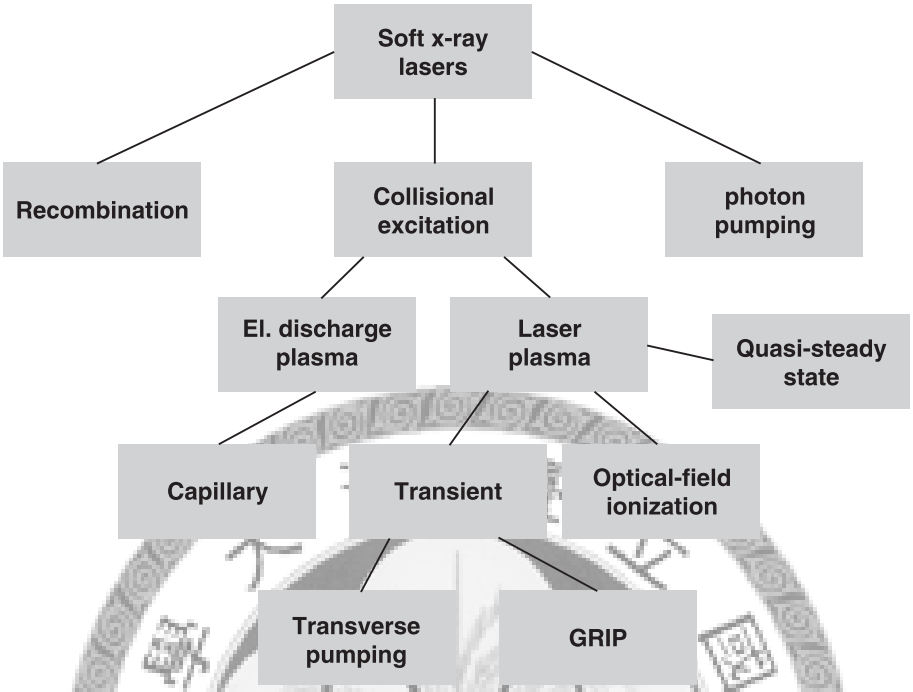

Figure 1.5: Classification of soft x-ray lasers by different pumping schemes.

On the other hand, the lower lasing level is also populated by electron collisions, but radiative decay of this level to ground state can be much faster, whereas that of upper state directly to ground state is optically forbidden. Therefore the population inversion between upper and lower levels is established.

In principle this pumping scheme could be put on any ion with appropriate lasing levels. Experimentally high-gain x-ray lasers based on collisional-excitation scheme were demonstrated only in three isoelectronic sequences: neon-like (10 bound electrons), nickel-like (28 bound electrons), and palladium-like (46 bound electrons) ions. These ion species all have a closed-shell structure and thus a high ionization energy, making them relatively stable lasing ions over a wide range of plasma parameters. Over past two decades, theoretical investigations and experimental demonstrations mostly focused on the $3p - 3s$ transition in Ne-like ions and $4d - 4p$ transition in Ni-like ions over a broad range of atomic numbers. Figure 1.7 (a) and (b) show the energy-level diagrams of the Ne-like and Ni-like ions , respectively. X-ray laser lines were generated between 60 and 10 nm in Ne-like ions and between 25 and 4 nm in Ni-like ions [15, 23], and Figure 1.8 depicts the lasing wavelengths as a function of atomic number for Ne-like and Ni-like ions.

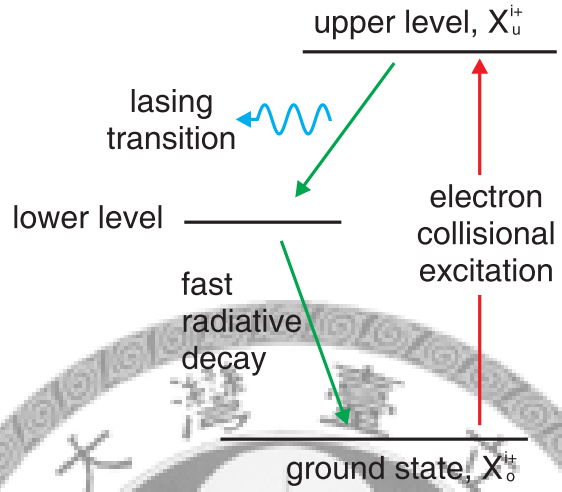

Figure 1.6: Illustration of simplified energy diagram for the collisional-excitation x-ray laser.

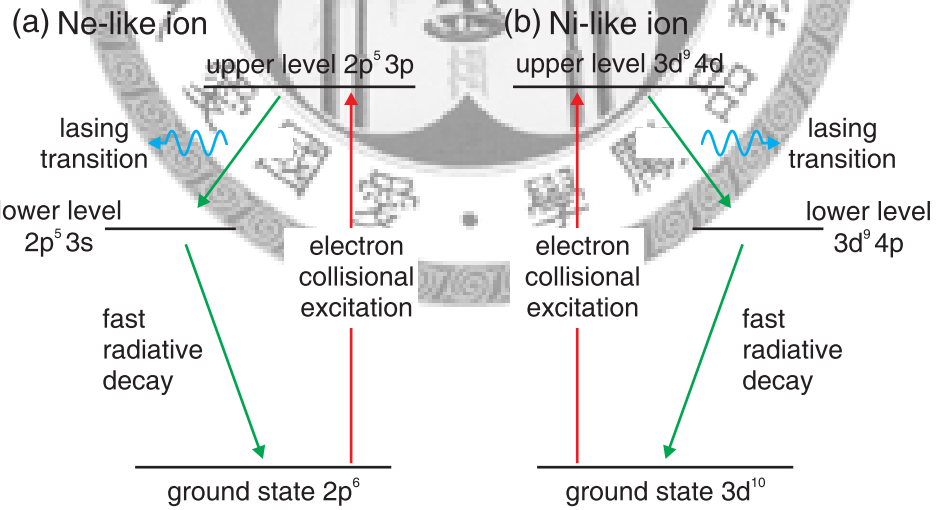

Figure 1.7: Illustrations of (a) the $2p^5\ 3p$ – $2p^5\ 3s$ transition of Ne-like and (b) $3d^9\ 4d$ – $3d^9\ 4p$ transition of Ni-like ions.

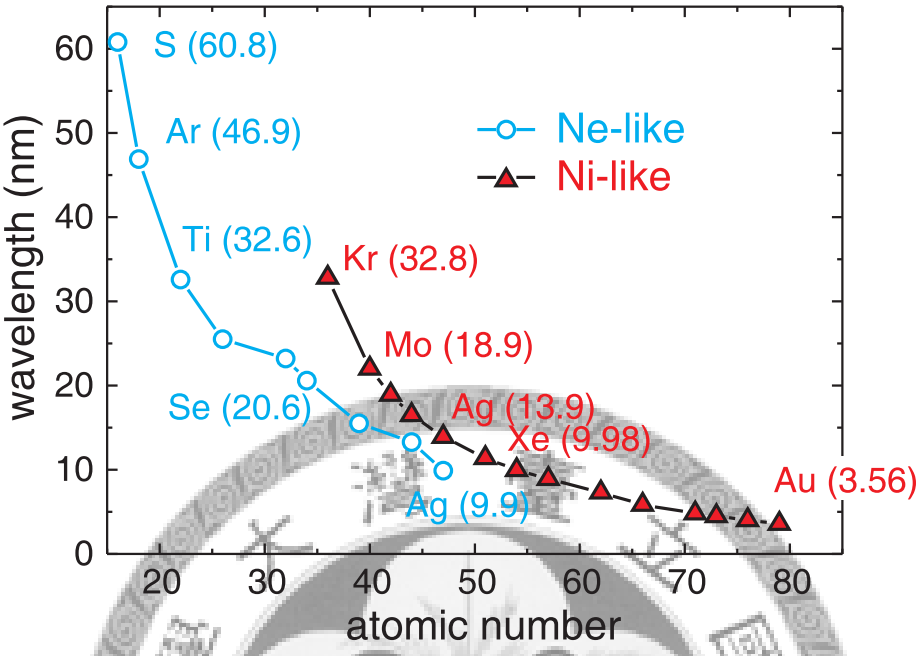

Figure 1.8: Lasing wavelengths as a function of atomic number for Ne-like (circle) and Ni-like (square) transitions.

The early demonstrations of collisional-excitation x-ray lasers relied on a huge laser facility that was only available in two or three laboratories in the world [16]. In this case, x-ray lasers were pumped by one relatively long (on the order of a nanosecond), high-energy (on the order of a kilojoule) laser drivers with a low repetition rate (on the order of one shot/hour). Because the pulse duration of the pump laser is much longer than the population inversion lifetime, the x-ray laser pumped by this type of laser is referred to as quasi-steady-state (QSS) x-ray laser. The high cost, large scale, and low repetition rate severely hindered the developments and applications of soft x-ray lasers. However, with the advent of the chirped pulse amplification (CPA) technique for high-power laser systems, considerable progress was obtained through the use of picosecond to femtosecond laser pulses combining with two new methods: transient collisional excitation and optical-field ionization (OFI).

The transient excitation scheme was proposed in 1989 by Afanasiev and Shlyaptsev to increase the efficiency of lasing [24]. This scheme utilized the difference between the population inversion lifetime (a few tens of picoseconds) and the ionization time (hundreds picoseconds). A prepulse with an intensity of about 10^{12} W/cm^2 and a duration on the order of one nanosec-

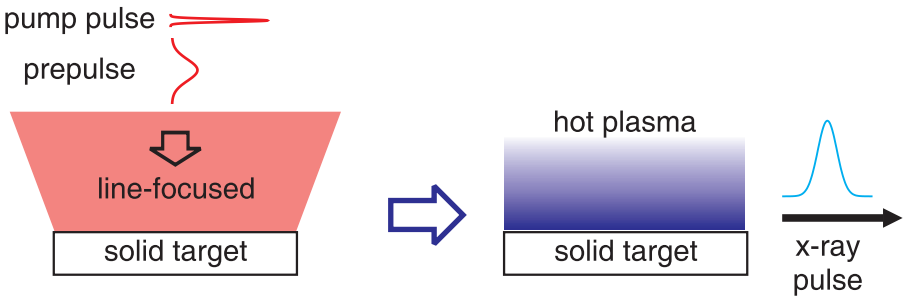

Figure 1.9: Illustration of a transient-collisional-excitation solid-target x-ray laser.

ond creates a plasma with a suitable density and ionization state. Then the plasma is rapidly heated by a pump pulse with an intensity of about 10^{15} W/cm^2 and a duration on the order of one picosecond. Because the time for heat the electron temperature to match or exceed the excitation energy is much shorter than that for further ionization and other plasma evolutions, a large transient population inversion density is established. The first transient collisional excitation x-ray laser was reported in 1997 for Ne-like titanium lasing at 32.6 nm [25]. Soon thereafter, lasing was performed at shorter wavelengthes [26] and saturated outputs were also obtained [27, 28] using various solid targets. In transient-collisional-excitation x-ray lasers, solid slab or foils are the most commonly used targets. For solid-target x-ray lasers, the transverse pumping configuration is usually used, as shown in Figure 1.9. In this configuration, the pumping efficiency is low, so the required pumping energy is still large (a few Joules) and the repetition rate is too low (one shot in a few minutes) to be used in several potential applications, such as x-ray lithography and x-ray radiography.

In 1988, another novel method, optical-field-ionization (OFI) pumping, was proposed by Corkum and Burnett [29]. Instead of the collisional ionization and heating which are dominated in the operation of solid-target x-ray lasers, the atoms are ionized to specific ion species through optical-field ionization and simultaneously obtained a large energy by above-threshold-ionization (ATI) heating in the operation of gas-target x-ray lasers. In gas-target x-ray lasers, longitudinal pumping is the preferred method to make good use of pumping energy, as shown in Fig. 1.10. The required pumping lasers for OFI x-ray lasers are femtosecond terawatt laser systems, with a repetition rate of 10 Hz. Therefore, OFI collisional-excitation x-ray lasers driven by a femtosecond high-repetition-rate laser are dramatically reduced in cost and size, and can be operated at 10 Hz, providing a very promising

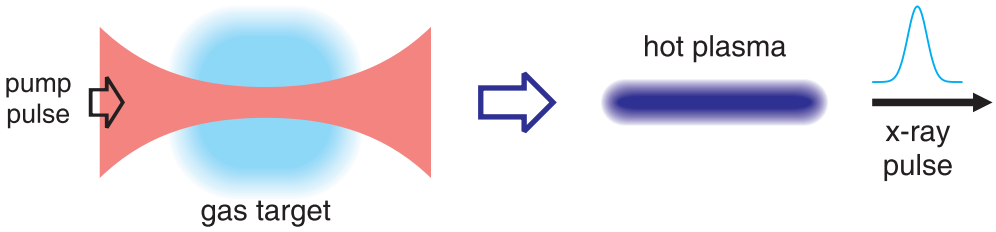

Figure 1.10: Illustration of an optical-field-ionization gas-target x-ray laser.

scheme for practical applications. The details of OFI collisional x-ray laser will be described in Chapter2.

Recently a modification of the transient collisional scheme, grazing incidence pumping (GRIP), was proposed by Shlyaptsev *et al.* [30] and first demonstrated by Keenan *et al.* in 2005 [31]. The main difference in GRIP scheme is that the short pulse, which creates population inversion and gain, is to use refraction in grazing incident geometry to redirect the pump beam along a region of selected electron density near target where the soft x-ray gain is maximum. This leads to an increased absorption of pump energy, thus better pumping efficiency. Further the density at which the short pulse is absorbed can be matched to the optimum density for gain by adjusting the grazing angle. Therefore GRIP scheme reduces the pump energy to sub-joule, which can be operated in a table-top high-repetition-rate laser system. Figure 1.11 illustrates the setup of a GRIP x-ray laser. In addition to the laser-driven x-ray lasers, capillary discharge pumping opened up a new road in the development of soft x-ray lasers. Rocca and his group demonstrated saturated lasing in Ne-like Ar ions at 46.9 nm by fast high-voltage discharge in a capillary [32, 33]. This pumping configuration is shown in Figure 1.12.

1.2.3 Recombination Soft-X-Ray Lasers

Recombination scheme was proposed by Gudzenko and Shelepin in 1965 [34], and was first demonstrated by Suckewer *et al.* in 1985 [17]. In this scheme, the atoms also need to be ionized to a closed shell, such as H-like or Li-like ions. Next, the ions and electrons have to recombine very fast through three-body recombination (2 electrons and one ion), in which an electron loses the energy to another electron and then combine with an ion. Then the recombined electrons are initially trapped in the highly excited states and decay downward via collisional-radiative cascade to the upper state. Usually

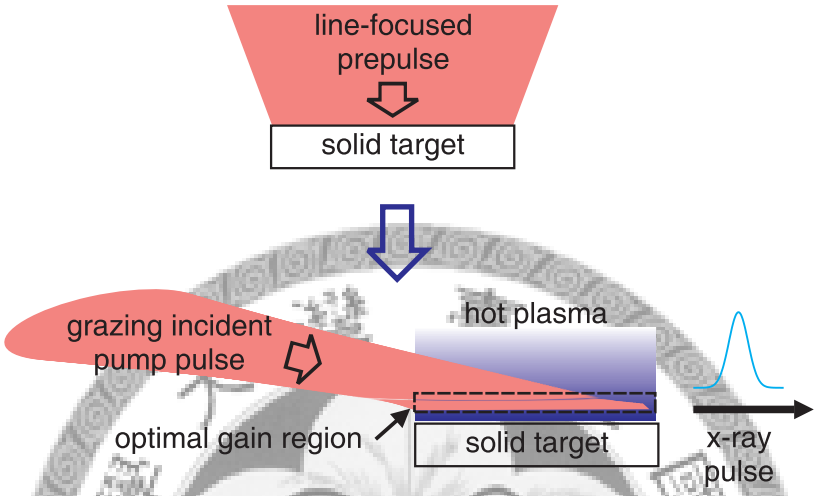

Figure 1.11: Illustration of a grazing-incidence-pumping solid-target x-ray laser.

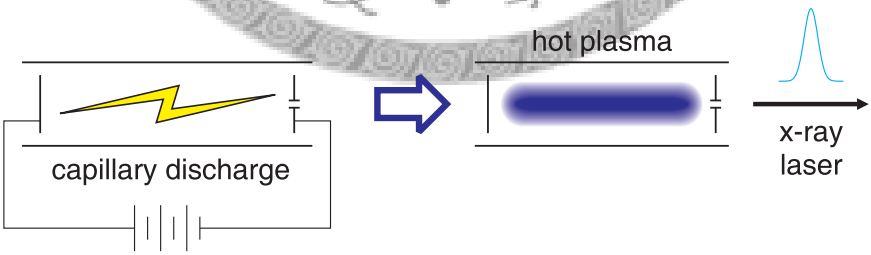

Figure 1.12: Illustration of a capillary discharge x-ray laser.

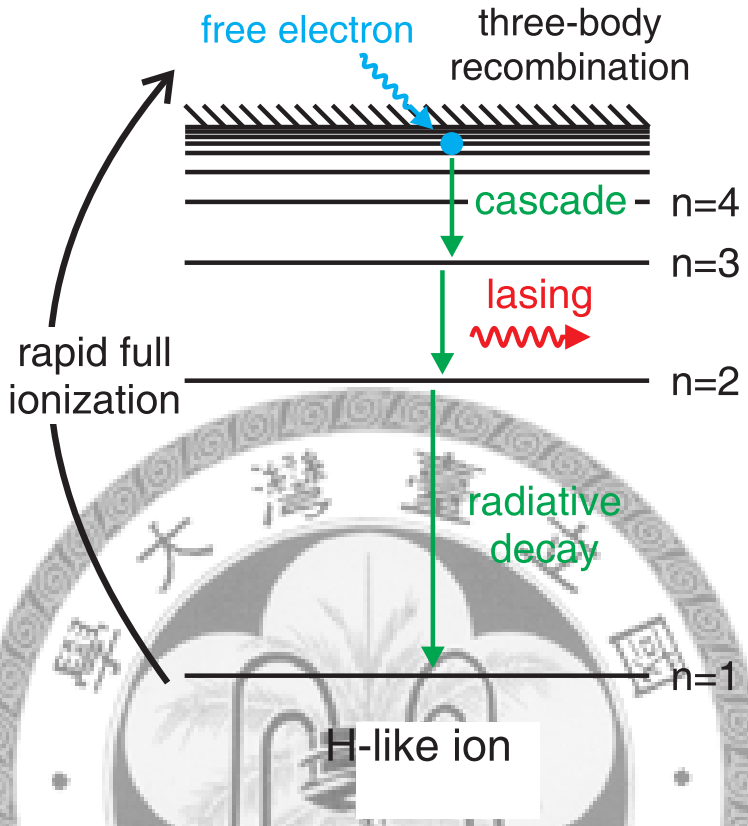

Figure 1.13: Illustration of the 3-2 lasing transition of the H-like ion.

the upper state has a longer lifetime and the lower state is depopulated through fast radiative decay. Hence, a population inversion can be built up between upper and lower levels. Figure 1.13 depicts the energy-level diagram for the 3 - 2 transition in a H-like ion. In this scheme the lasing is dominated by the three body recombination rate R [35], and

$$R \; \alpha \; n_e^2 T_e^{-\frac{9}{2}}, \tag{1.4}$$

where n_e and T_e are the electron density and electron temperature, respectively. Therefore, the generation of large population inversion by recombination requires a dense and relatively cold plasma. As seen from the equation, the collisional recombination rate R is proportional to the square of the electron density. Moreover the recombination rate is also extremely sensitive to the electron temperature. Therefore, the generation of large population inversion by recombination requires a dense and relatively cold plasma.

An important feature of recombination x-ray laser is its lasing wavelength,

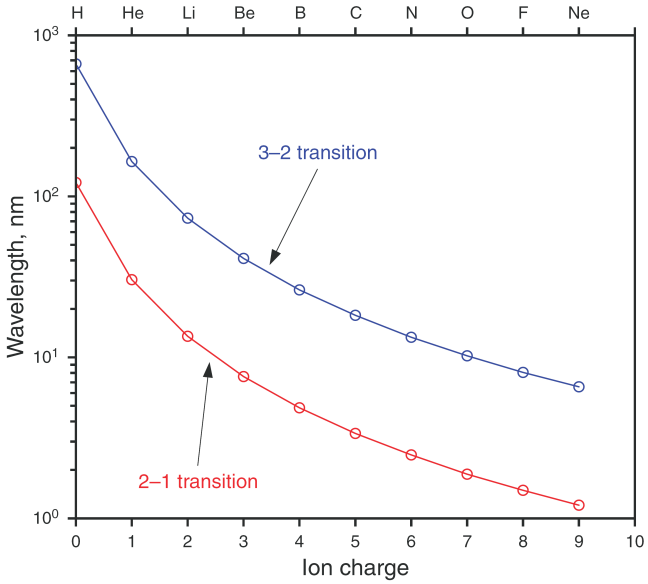

Figure 1.14: Scaling of the wavelengths versus ion charge Z-1; H-like ions for 3-2 and 2-1 lasing transitions.

as shown in Figure 1.14 (from [36]). One can see the wavelength fast decreases with the increasing atomic number Z (scale as Z^{-2}), even can reach the "water window" region (2.3 - 4.4 nm) when $Z > 5$. However, a dense and cold plasma is difficult to be produced by the laser with a high intensity, much less recombination x-ray lasers have been demonstrated in experiments [17, 37, 38] when compared to collisional-excitation x-ray lasers.

1.3 About the Thesis

This thesis records my efforts and accomplishments in the development of soft x-ray lasers. Most of the work presented in this thesis was conducted in close collaboration with my colleague Ming-Chang Chou. The experiments described in this thesis was performed at the 10-TW laser facility in High-Field Physics and Ultrafast Technology Laboratory, part of the Institute of Atomic and Molecular Sciences (IAMS), Academia Sinica, Taiwan (R. O. C.). The organization of this thesis is as follows.

Chapter 1 gives an overview of the ultrashort coherent soft x-ray sources and their advantages and limitations for future applications. Special emphasis is given to the introduction of the soft x-ray lasers which is the subject of this thesis.

Chapter 2 reports the demonstration of an optical-field-ionization collisionally excitated x-ray lasing by using an optically preformed plasma waveguide. With a 9-mm-long pure krypton plasma waveguide, prepared by using the axicon-ignitor-heater scheme, 32.8-nm Ni-like Kr lasing is enhanced by 400 folds relative to the case without the plasma waveguide. An output level of 8×10^{10} photons/pulse is reached at an energy conversion efficiency of 2×10^{-6}, and the divergence angle of which is 5.6 mrad. Under the same configuration of the pump and waveguide-forming pulses, strong lasing at Xe^{8+} 41.8 nm and Ar^{8+} 46.9 nm are also achieved. Finally, spatial coherence measurement of the 32.8-nm Ni-like krypton lasing by using the Young's double-slit interferometry are reported in Section 2.6.

Chapter 3 reports the demonstration of different kinds of multi-line soft x-ray lasers. They include three different lasing lines in the three various pure-gas plasma waveguide, multiple lasing lines in the same pure-gas plasma waveguide, and the simultaneous multispecies x-ray lasing in a Kr-Ar mixed-gas plasma waveguide, showing the versatility of the waveguide-based soft x-ray lasers. To gain a deep insight, extensive experimental results including the pump-energy dependence, the density dependence, and the effects of parameters that control the waveguide fabrication for the multi-line soft x-ray lasers are presented and discussed.

In chapter 4, demonstration of a strongly saturated waveguide-based soft x-ray laser seeded by high harmonic generation (HHG) for Ni-like krypton at 32.8 nm is reported. With seeding the divergence of the soft x-ray laser is greatly reduced from 4.5 mrad to 1.1 mrad, and the spatial coherence is

enhanced by at least a factor of 4. The polarization measurement shows that the seeded soft x-ray laser can have the same polarization state with HHG seed. The optimization and characterization of the seeded soft x-ray laser are also described in details. Comparisons of our seeded waveguide-based soft x-ray laser with synchrotron radiation and other seeded soft x-ray lasers in the world are given in the summary.

Finally, chapter 5 summarizes the results presented in the previous chapters and gives an outlook to the future. Especially the prospect of the generation of a sub-10-nm soft x-ray laser with a plasma waveguide is discussed.

The original works described in Chapter 2 and 3 are published in Phys. Rev. Lett. **99**, 063904 (2007) and Phys. Rev. A **76**, 053817 (2007). The work of the seeded soft x-ray laser in a plasma waveguide in Chapter 5 is published in Opt. Lett. **34**, 3562 (2009).

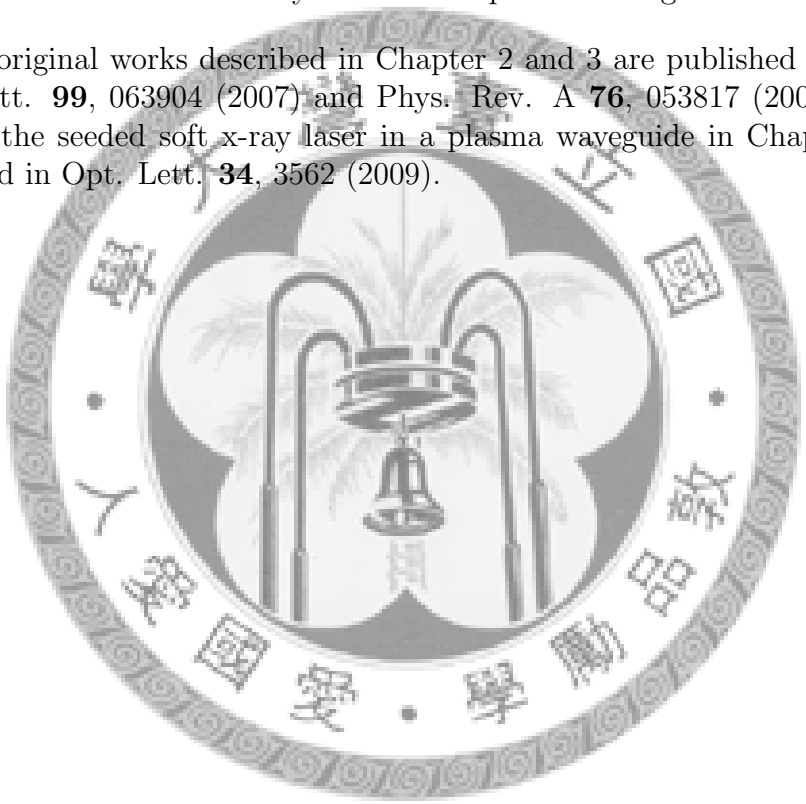

Chapter 2

Optical-Field-Ionization Soft X-Ray Lasers with an Optically Preformed Plasma Waveguide

2.1 Introduction

Since the first soft x-ray laser was demonstrated in 1985 [16, 17], significant progress has been made in pushing x-ray lasers toward higher intensity, shorter pulse duration, higher coherence, and, in particular, compact size with high repetition rate. In the early days, the development of soft x-ray lasers relied on huge laser facilities to deliver a high energy density for excitation. The very high cost, large size, and low-repetition rate limited the development and application of such x-ray lasers. However, with the advent of table-top high-power laser systems and the subsequent optical-field-ionization (OFI) method, this situation has changed. OFI collisional-excitation x-ray lasers driven by a femtosecond high-repetition-rate laser are dramatically reduced in cost and size, and can be operated at 10 Hz, providing a very promising scheme for practical applications. The collisionally excited OFI soft-x-ray laser was first proposed by Corkum and Burnett in 1988 [29] and was demonstrated in a gas cell by Lemoff *et al.* [39, 40]. Later, in view of the versatility of gas jets, our group demonstrated nearly saturated x-ray lasing in xenon and krypton clustered gas jets [41, 42].

In OFI x-ray lasers, longitudinal pumping is the preferred method to meet the requirements of high-intensity pumping and traveling-wave pumping. A

serious problem for longitudinally pumped OFI x-ray lasers is the limited gain length caused by ionization-induced refraction [43, 41]. If a waveguide is used to maintain the high-intensity pump pulse over a long distance, the length of the gain region for x-ray lasing can be increased, and the length of the under-ionized absorptive region can be reduced. Butler *et al.* first reported the enhancement of OFI Pd-like xenon x-ray lasing at 41.8 nm in a preformed plasma waveguide produced by discharge of a capillary tube filled with an Xe/H_2 gas mixture [44, 45]. The lasing intensity with the waveguide was approximately 4 times larger than that from a gas cell. Later, Mocek *et al.* used a 15-mm-long, multi-mode, gas-filled capillary tube [46, 47, 48] to enhance the output of Xe^{8+} lasing at 41.8 nm by an order of magnitude with respect to that from a gas cell of the same length. The waveguide effect of these methods was not large enough to overcome the small gain coefficient, so they cannot be applied to other high-threshold low-gain lasing species, such as Ne-like Ar and Ni-like Kr x-ray lasers. Besides, the capillary tubes have its intrinsic limitations on the long-term high-repetition-rate operation: damage to the pin hole at the entrance and a limited lifetime. Therefore, it is highly desirable to find other guiding methods to support damage-free long-term high-repetition-rate operation.

Of all the guiding methods reported, an optically-preformed plasma waveguide in a gas jet [49, 50, 51] is the most favorable because it allows (1) guiding of the pump pulse and the lasing x-ray pulse simultaneously, (2) characterization of the underlying process through various diagnostics such as interferometry, and (3) damage-free long-term high-repetition-rate operation for practical applications. Finding methods to apply an optically preformed plasma waveguide to x-ray lasers has been an ongoing effort since 1995 [52], but enhancement of x-ray lasing by an optically preformed plasma has not been reported until our group recently demonstrated dramatic enhancement of the OFI x-ray lasers with an optically preformed plasma waveguide [53, 54]. In this chapter, the basic principles of the OFI collisionally excited x-ray laser are described in Sec. 2.2. In Sec. 2.3, the basic concepts of the plasma waveguide are presented. The axicon ignitor-heater scheme for producing plasma waveguide is described. The experimental setup for producing OFI soft x-ray lasers in an optically preformed plasma waveguide and the primary diagnostics are presented in Sec. 2.4. Measurements of waveguide formation, x-ray lasing divergence, and x-ray lasing spectra are described in Sec. 2.5. In Sec. 2.6, measurements of spatial coherence on Ni-like 32.8-nm Kr lasing with a plasma waveguide are reported.

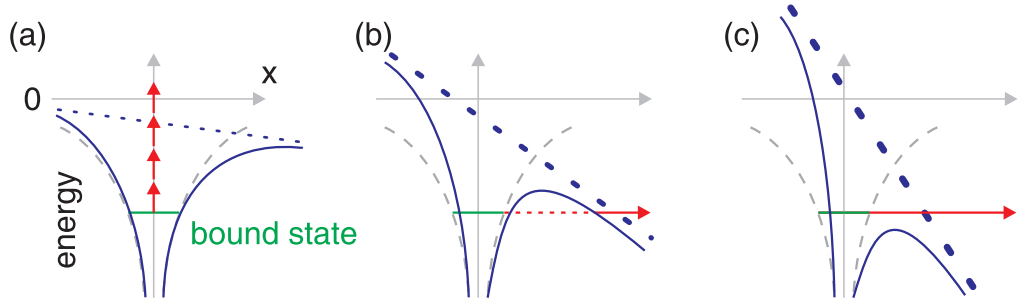

Figure 2.1: Optical-field ionization: (a) multiphoton ionization, (b) tunnelling ionization, and (c) over-barrier ionization.

2.2 Principle of an Optical-Field-Ionization Collisional-Excitation Soft X-Ray Laser

2.2.1 Optical-Field Ionization

An intense laser pulse can directly ionize atoms, even if the individual photon energy is much smaller than the ionization potential. Such ionization is generally known as "optical-field ionization" (OFI), a basic process of the interaction between laser and matter. OFI can be divided into three regimes according to the strength of the laser field. Figure 2.1 depicts the concepts associated with each regime. First, when the laser intensity is increased, a bound electron has a certain probability of absorbing several photons simultaneously and overcoming the ionization potential to become a free electron. This process is called "multi-photon ionization". If the laser intensity is further increased, the ionization process can be treated semiclassically, such that the potential well of the atom is tilted or surpressed by the laser field. Therefore, a bound electron has a chance to tunnel through the reduced energy barrier and become released. This is called "tunnelling ionization". When the laser intensity is increased so high that the energy barrier is tilted and becomes lower than the bound state, the electron leaves the atom directly. This final process is known as "over-barrier ionization".

Keldysh defined a parameter to determine where each type would dominate, known as the Keldysh parameter [55],

$$\gamma = \sqrt{\frac{U_i}{2U_p}}, \tag{2.1}$$

where U_p is the ponderomotive potential of the laser, and U_i is the ionization

potential of the atom or ion. The ponderomotive potential is the average kinetic energy of an electron in the laser field, given by

$$U_p = \frac{e^2}{4\, m_e\, \omega^2} |\mathbf{E}_0|^2 \ , \tag{2.2}$$

where e is the charge of the electron, m_e is the mass of the electron, ω is the laser frequency, and $\mathbf{E}_0$ is the electric field of the laser. In the regime of $\gamma > 1$, the ionization can be described as a multiphoton process. For $\gamma < 1$, it is in the tunnelling/over-barrier regime, and the ionization process can be described by using a semiclassical method [56, 57].

When $\gamma < 1$, the ionization rate can be calculated from DC tunnelling theory [58]. The ionization rate of a hydrogen-like ion in a static electric field E_s is well known:

$$W_{st}(E_s) = 4\,\omega_a \left(\frac{U_i}{U_H}\right)^{5/2} \frac{E_a}{E_s} \exp\left[\frac{-2}{3}\left(\frac{U_i}{U_H}\right)^{3/2} \frac{E_a}{E_s}\right] , \tag{2.3}$$

where U_H and U_i are the ionization potentials of hydrogen and the atom or ion in question, ω_a is the unit of atomic frequency, and E_a is the atomic field strength at the first Bohr radius of hydrogen.

$$\omega_a = \frac{m_e}{\hbar^3} \frac{e^4}{(4\,\pi\,\epsilon_0)^2} \simeq 4.1 \times 10^{16} \text{ Hz}$$

$$E_a = \frac{m_e^2}{\hbar^4} \frac{e^5}{(4\,\pi\,\epsilon_0)^3} \simeq 5.1 \times 10^9 \text{ V/cm}$$

For non-hydrogen-like atoms, the static-field ionization rate is modified to [59, 60]

$$\begin{aligned} W_{st} \;=\; & \frac{{\omega_a}^2}{2}\, C_{n,l}\, \frac{U_i}{U_H}\, \frac{(2l+1)(l+|m|)!}{2^{|m|}\,(|m|)!\,(1-|m|)!} \left[2\left(\frac{U_i}{U_H}\right)^{3/2} \frac{E_a}{E_s}\right]^{2n^*-|m|-1} \\ & \times \exp\left[\frac{-2}{3}\left(\frac{U_i}{U_H}\right)^{3/2} \frac{E_a}{E_s}\right] , \end{aligned} \tag{2.4}$$

where $C_{n,l}$ is a constant that is approximately 2; n^* is the effective principal quantum number ($n^* = Z/(U_i/U_H)^{1/2}$); l is the angular momentum quantum number; m is the magnetic quantum number, and Z is the charge state of the resulting ion. The response time of a bound electron is much shorter than the

period for which the electromagnetic field is applied, so the ionization rate in such an AC field is obtained by replacing the static field E_s in Eq. (2.4) with a time-dependent field $\mathbf{E}(t)$,

$$W_{ac}(t) = W_{st}(|\mathbf{E}(t)|)\,. \tag{2.5}$$

The density of ions in ionization stage i is determined by the rate equations

$$\frac{\partial N_i}{\partial t} = -N_i W_{i\to i+1} + N_{i-1} W_{i-1\to i}\,. \tag{2.6}$$

The electron density variation is given by

$$\frac{\partial N_e}{\partial t} = \sum_{i=0}^{i} N_i W_{i\to i+1}\,. \tag{2.7}$$

Given the laser parameters, the initial atom density, and the ionization potential in each ionization stage, the evolution of the ion populations and the electron density can be calculated by using Eq.(2.5)-(2.7). Figures 2.2(a) and (b) plot the evolution of the relative population of argon ion species in response to linear-polarized and circular-polarized laser pulses, respectively. The laser pulses have a laser wavelength of 810 nm, pulse duration of 60 fs (FWHM), and peak intensity of 3×10^{16} W/cm^2. The gray areas in the figures show the respective pulse wave forms. In the case of linear polarization, the laser pulse can ionize the Ar ions to a higher ionization stage (Ar^{6+}); this is due to the larger peak electric strength for the linear-polarized laser. Furthermore, the evolution curves are not smooth and have step-like shapes. This is because the electric field oscillates sinusoidally and the ionization only occurs near the peak values. Consequently the period between the two successive steps is roughly equal to the half cycle of the laser field. In contrast, with circular polarization, the evolution curves are continuous and much smoother because the electric field strength increases continuously with time.

2.2.2 Above-threshold-ionization heating

In the tunnelling limit ($\gamma < 1$), the ionization process can be described semiclassically by a two-step process [56, 57]. First, the electron is removed from the atom, absorbs an amount of energy equal to the ionization potential, and becomes a free electron at rest. Next, the electron is accelerated by the laser field and obtains some residual energy after the laser pulse has passed by. This heating mechanism is known as the "above-threshold-ionization"(ATI) heating.

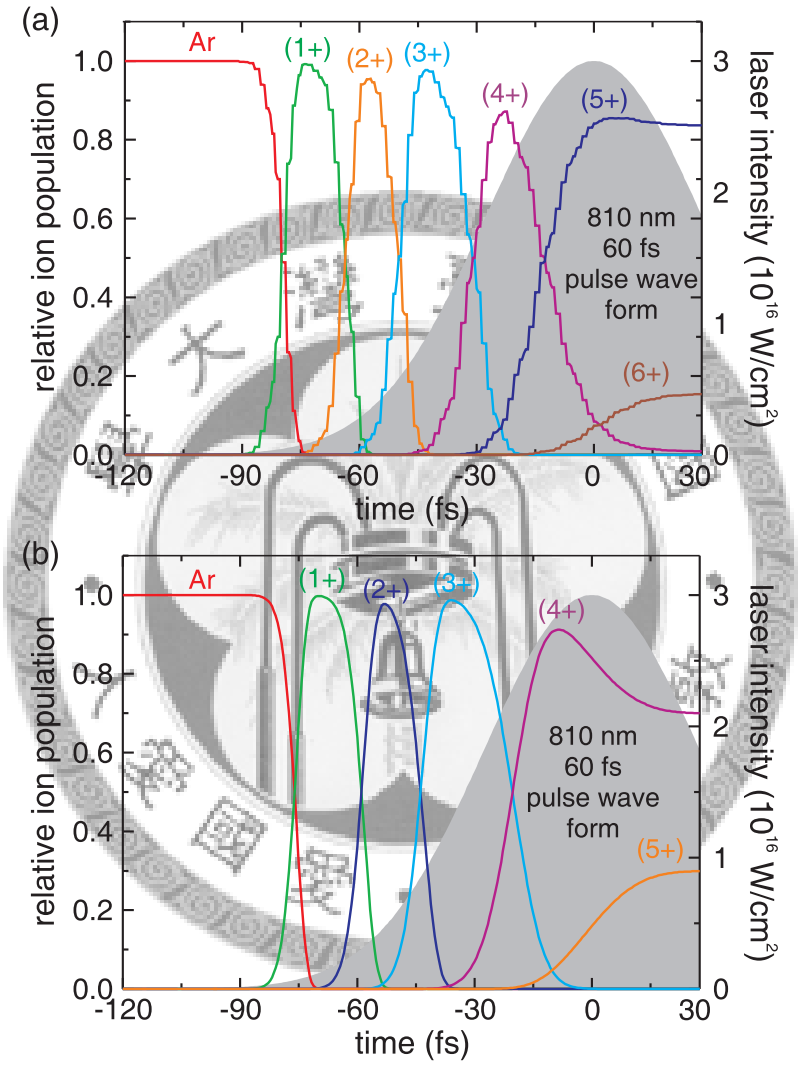

Figure 2.2: Calculated evolution of the relative population of argon ion species ionized by a linear-polarized pulse (a) and a circular-polarized pulse (b). The laser pulses have a wavelength of 810 nm , duration of 60 fs (FWHM), and peak intensity of 3×10^{16} W/cm^2.

The residual kinetic energy of the released electron in an applied electromagnetic field can be calculated in a classical way. Consider an electron released at time t_0 from rest into an intense laser field $\mathbf{E}(t) = E_0 \sin(\omega t)\hat{e}_x + \alpha E_0 \cos(\omega t)\hat{e}_y$, where $\alpha \leq 1$ allows for any polarization. The velocity of the electron in the laser field is given by

$$\begin{aligned} v_x(t) &= \frac{eE_0}{m_e\omega}\left[\cos(\omega t) - \cos(\omega t_0)\right] \\ v_y(t) &= \alpha\frac{-eE_0}{m_e\omega}\left[\sin(\omega t) - \sin(\omega t_0)\right] . \end{aligned}$$

Therefore, the cycle-averaged kinetic energy equals

$$K = \frac{1}{2}m_e\langle v_x(t)^2\rangle + \frac{1}{2}m_e\langle v_y(t)^2\rangle. \tag{2.8}$$

In the case of linear polarization ($\alpha = 0$), the laser field $\mathbf{E}(t) = E_0 \sin(\omega t)\,\mathbf{e}_x$. The cycle-averaged kinetic energy becomes

$$\begin{aligned} K &= \frac{1}{2}m_e\langle v^2\rangle \\ &= \frac{e^2E_0^2}{4\,m_e\,\omega^2}\left[1 + 2\,\cos^2(\omega t_0)\right] . \end{aligned} \tag{2.9}$$

The first term on the right-hand side is the coherent quiver energy $\epsilon_q = e^2E_0^2/4\,m_e\,\omega^2$, which will return to the laser pulse as the pulse passes by. The second term is known as the ATI energy, which is the residual energy of the electron after the optical pulse has passed. Note that the ATI energy depends on the relative phase between the ionization and the laser field. For example, ionization occurs mostly when $E_0 \sin(\omega t_0)$ is maximum, which is when $\omega t_0 = \pi/2$, thus the electron has no residual energy. In contrast, hot electrons are created only at the minimum field $\omega t_0 = 0$, in which the ionization rate is low. As a result of this feature, the energy spectrum of electrons produced from optical-field ionization in a linear-polarized field is concentrated at low energy. In general, an electron ionized at some arbitrary phase mismatch $\Delta\phi$ carries a residual kinetic energy,

$$K_{ATI} = 2\,\epsilon_q \cos^2(\Delta\phi). \tag{2.10}$$

Figure 2.3(a) plots the evolution of the relative population of xenon atoms

$$n_{atom}(t) = \exp\left[-\int_{-\infty}^{t} W_{ac}(t')\,dt'\right]$$

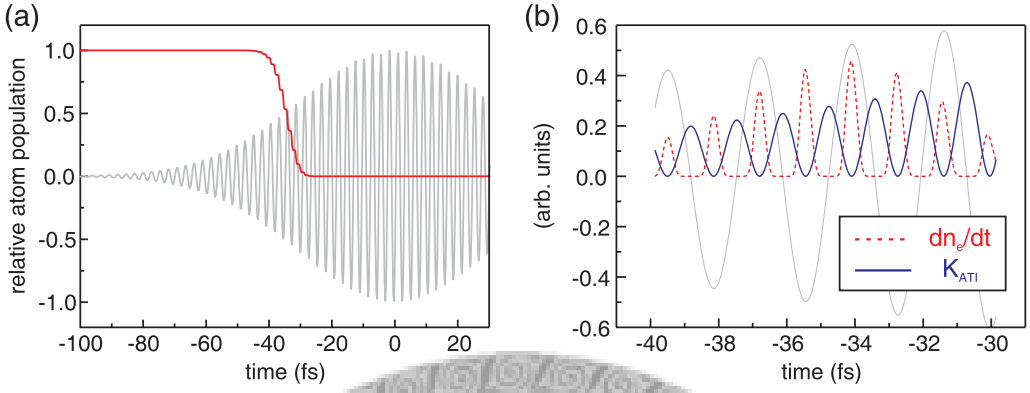

Figure 2.3: (a) Calculated evolution of the relative population of helium atoms ionized by a linear-polarized laser pulse with a wavelength of 810 nm, duration of 50 fs (FWHM), and peak intensity of 5×10^{15} W/cm^2. (b) Calculated variation in electron density as a function of time (dne/dt, solid line) and ATI energy obtained by electrons ionized at that time (K_{ATI} , dashed line). The electric field of the laser pulse is represented by gray lines in both figures.

in response to a linearly polarized laser pulse with a wavelength of 810 nm, duration of 50 fs (FWHM) and peak intensity of 5×10^{15} W/cm^2. The ionization potential U_i of neutral helium is 24.59 eV. Figure 2.3(b) shows the corresponding variation in electron density and ATI energy as functions of time.

On the other hand, a circularly polarized laser field ($\alpha = 1$) can be represented as $\mathbf{E}(t) = E_0 \sin(\omega t)\,\mathbf{e}_x + E_0 \cos(\omega t)\,\mathbf{e}_y$, in which the quiver energy $\epsilon_q = e^2 E_0^2 / 2\, m_e\, \omega^2$. The velocity of the electron created at t_0 is obtained as

$$\begin{aligned} v_x &= \frac{eE_0}{m_e\,\omega}\,[\cos(\omega t) - \cos(\omega t_0)\,] \\ v_y &= \frac{eE_0}{m_e\,\omega}\,[\sin(\omega t_0) - \sin(\omega t)\,]\,, \end{aligned}$$

so the residual ATI energy is

$$K_{ATI} = \epsilon_q = \frac{e^2 E_0^2}{2\, m_e\, \omega^2}\,. \tag{2.11}$$

This is because the field strength of a circular-polarized laser pulse never becomes zero, and only the orientation changes. Hence, at a given intensity, a circularly polarized field can produce more hot electrons than a linearly

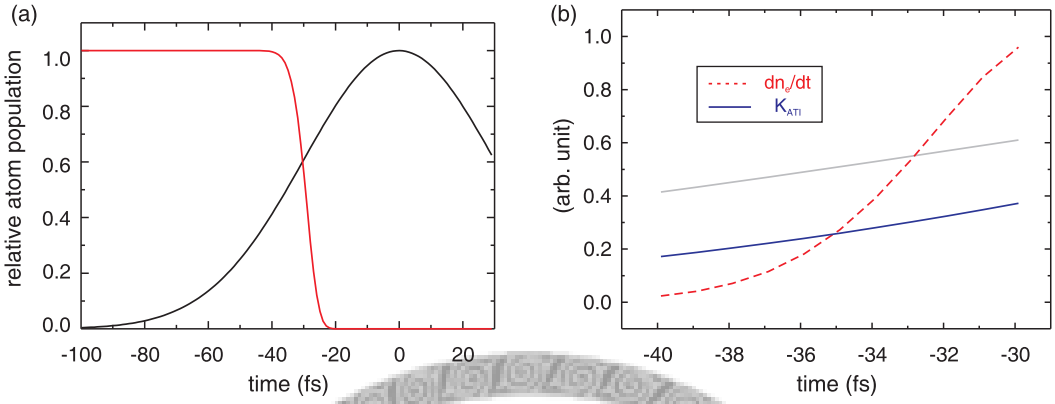

Figure 2.4: (a) Calculated evolution of the relative population of helium atoms ionized by a circularly polarized laser pulse with a wavelength of 810 nm , duration of 50 fs (FWHM), and peak intensity of 5×10^{15} W/cm^2. (b) Calculated variation in electron density as a function of time (dne/dt, solid line) and ATI energy obtained by electrons ionized at that time (K_{ATI} , dashed line). The electric field of the laser pulse is represented by gray lines in both figures.

polarized field. Figure 2.4(a) shows the evolution of the relative population of helium atoms under the influence of a circularly polarized laser pulse with the same wavelength, duration, and peak intensity as that in Fig. 2.3. Figure 2.4(b) shows the corresponding variation in electron density and ATI energy as functions of time. The obtained electron energy spectra for a linearly polarized laser pulse (dashed line) and a circularly polarized laser pulse (solid line) are shown in Fig. 2.5. Electrons ionized from linearly and circularly polarized laser pulse have very different energy distributions: very cold electrons for linear-polarized light and very hot electrons for circular-polarized light.

2.2.3 Optical-Field-Ionization Collisional-Excitation Soft X-Ray Laser

Electron collisional excitation is a common mechanism for pumping a wide variety of x-ray lasers. In this scheme, sufficient energetic electrons are required to excite highly ionized ions from the ground state to the upper state. As stated in the last section, OFI and ATI heating can provide control of plasma ionization and plasma heating with an appropriate choice of laser intensity and polarization. Using an intense circularly polarized laser pulse

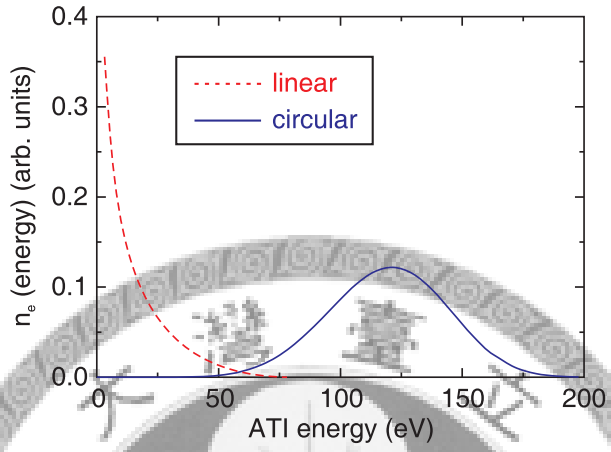

Figure 2.5: Calculated electron energy distribution under linear-polarized pulse (solid line) and circular-polarized pulse (dashed line).

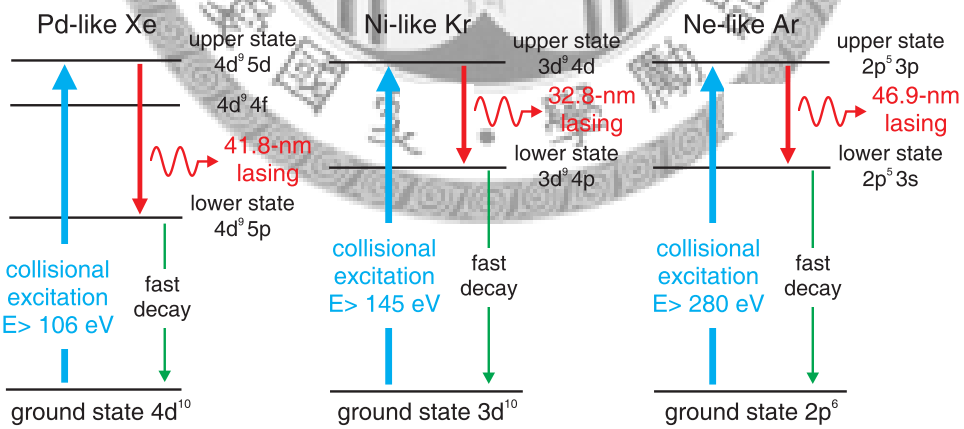

Figure 2.6: Energy-level diagrams of (a) Pd-like Xe ion, (b) Ni-like Kr ion, and (c) Ne-like Ar ion.

to pump the electron-excited x-ray lasers has been suggested by Burnett and Corkum in 1988 [29]. In this method, the intense circularly polarized laser pulse is used to create the highly ionized species via optical-field ionization. Then the released electrons will retain a kinetic energy equal to the quiver energy of the laser at the time of ionization after the pulse has passed. The resulting hot electrons are suitable for pumping the upper level of laser transition by collisional excitation. Based on this concept, Lemoff further proposed three specific systems of OFI collisionally excited soft-x-ray lasers in 1994 [39]: 41.8-nm Pd-like Xe lasing, 32.8-nm Ni-like Kr lasing, and 46.9-nm Ne-like Ar lasing.

Figure 2.6 shows energy-level diagrams for Pd-like xenon (Xe^{8+}), Ni-like Kr (Kr^{8+}), and Ne-like Ar (Ar^{8+}) x-ray lasers. The required ionization stage, the excitation energy, three major energy levels, and the main lasing line are all included in the figures. To achieve the efficient x-ray lasing, an appropriate laser intensity and plasma temperature that fulfill the lasing requirements should be chosen for the three systems. These parameters can be calculated according to the theories described in Secs. 2.2.1 and 2.2.2. Figure 2.7 (a) shows the evolution of the ion species created by a 60-fs laser pulse of 3.3×10^{17} W/cm^2 intensity. It can be seen that the Kr^{9+} ions are produced when the intensity is above 2×10^{17} W/cm^2. Thus the laser intensity should be controlled below this value to prevent from the overionization. Moreover, a threshold-like behavior appears in the laser intensity; the threshold intensity for ionization of the ninth electron is higher by a factor of nine than that for the eighth. Accordingly, with a proper choice of the laser intensity, the ion stages will not be below or above the specific stage (Kr^{8+}) due to the spatial distribution of the laser intensity over a sizable beam size, and an almost uniform plasma volume of Ni-like krypton is anticipated. Figure 2.7(b) shows the corresponding electron energy spectrum under the same laser conditions as in Fig. 2.7(a). The electrons, ranging from the third to the eighth, all have sufficient kinetic energy ($> 145eV$) to collisionally excite the ions from the ground state to the upper level. The same calculations are further applied for xenon and argon atoms. Here the intensities are precisely controlled so the pump pulse does not ionize the Xe^{8+} and Ar^{8+} ions to the next stage. The calculated results are shown in Figure 2.8 and Figure 2.9, respectively. The parameters are described in the figure captions.

In brief, the threshold nature of OFI makes it an attractive mechanism for creating plasmas suitable for gain media in soft-x-ray lasers, since the ion stage generated may be controlled by adjusting the laser intensity. The energy of the electrons after the passage of the laser pulse can be controlled

through the laser polarization: circular polarization produces hot electrons which can produce population inversions by electron collisions. Further, the gas-type gain media can allow for longitudinal pumping, which is a very efficient pumping configuration and can satisfy the requirements of high-intensity pumping and traveling-wave pumping. Hence, the development of soft-x-ray lasers in this work are all based on this lasing mechanism.

2.3 Optically Preformed Plasma Waveguide

2.3.1 Introduction

The interaction of ultrashort high-intensity laser pulses with gases and plasmas has a wide range of applications, such as the laser-driven electron acceleration [61], soft x-ray lasers [52], and high harmonic generation [62]. Such intensity can be achieved in a tightly focused beam with current high-power lasers, but the interaction length at high intensity is limited by the beam diffraction. For example, the interaction length represents the gain length in the soft x-ray laser. Hence, high x-ray output requires propagation over a long gain region. When a focused Gaussian pulse propagates along the z axis, the intensity distribution can be written as

$$I(r,z) = \frac{2P}{\pi w(z)^2}\exp\left[\frac{-2r^2}{w(z)^2}\right] = \frac{2E}{\tau\pi w(z)^2}\exp\left[\frac{-2r^2}{w(z)^2}\right] \tag{2.12}$$

$$w(z) = w_0\left[1+\left(\frac{z}{Z_R}\right)^2\right]^{1/2} \tag{2.13}$$

$$Z_R = \pi w_0^2/\lambda\ , \tag{2.14}$$

where λ, P, E, τ, w are the laser wavelength, power, energy, duration, and beam radius, respectively. w_0 is the beam waist, defined as the laser spot size at the focus(here, at $z=0$). Z_R is called the Rayleigh range, and $2Z_R$ is the confocal parameter, which is often referred to as the interaction length. A schematic illustration is shown in Figure 2.10. The peak intensity reaches the maximum at the focus and can be written as

$$I_0 = \frac{2E}{\tau\pi w_0^2}. \tag{2.15}$$

From Eq.2.14 and 2.15, we can see that a more intense laser beam requires a tighter focus and thus has a shorter interaction length. For example, when

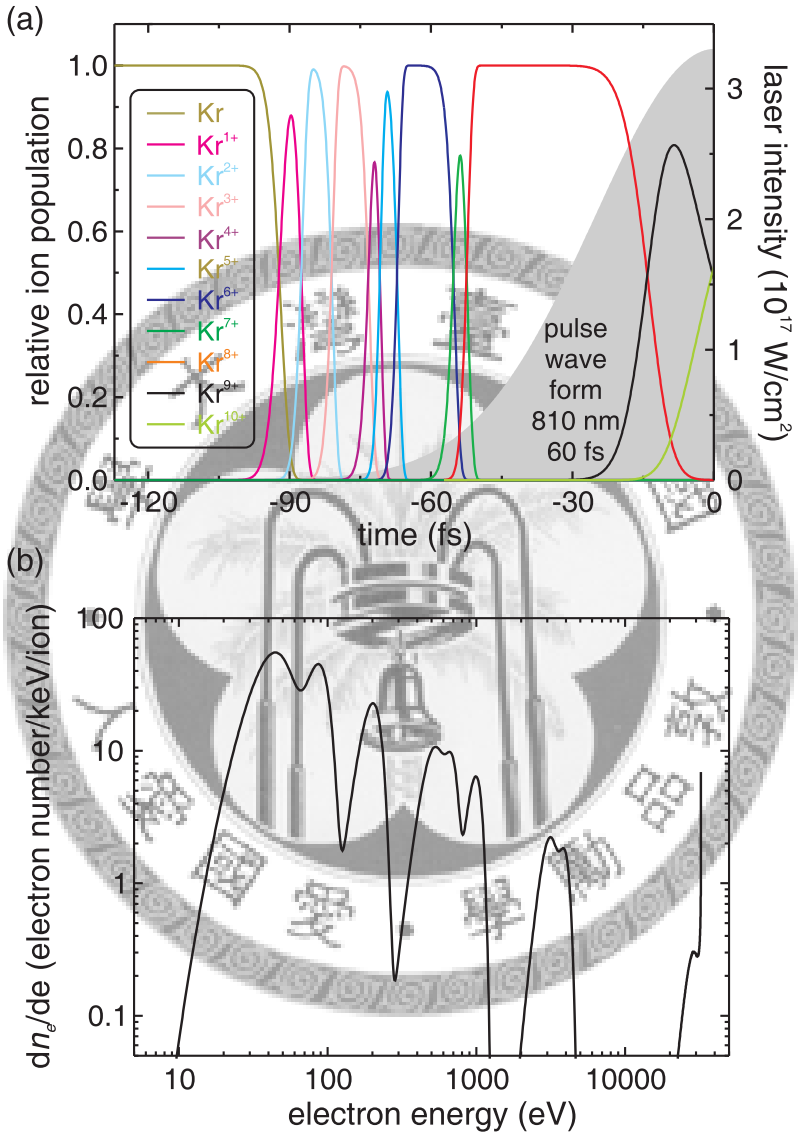

Figure 2.7: (a) Calculated evolution of the relative population of krypton ions by a circular-polarized laser pulse with a duration of 60 fs (FWHM), wavelength of 810 nm, and peak intensity of 3.3×10^{17} W/cm^2. (b) Energy spectrum of the ionized electrons.

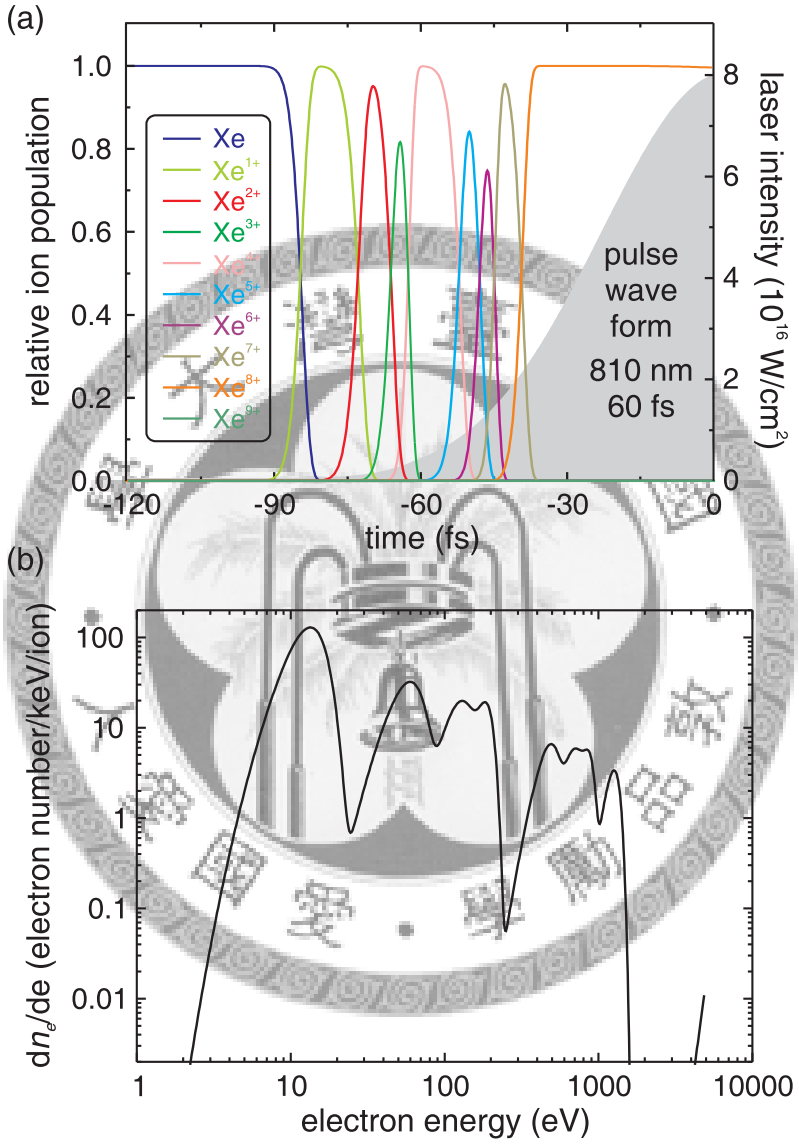

Figure 2.8: (a) Calculated evolution of the relative population of xenon ions by a circular-polarized laser pulse with a duration of 60 fs (FWHM), wavelength of 810 nm, and peak intensity of 8×10^{16} W/cm^2. (b) Energy spectrum of the ionized electrons.

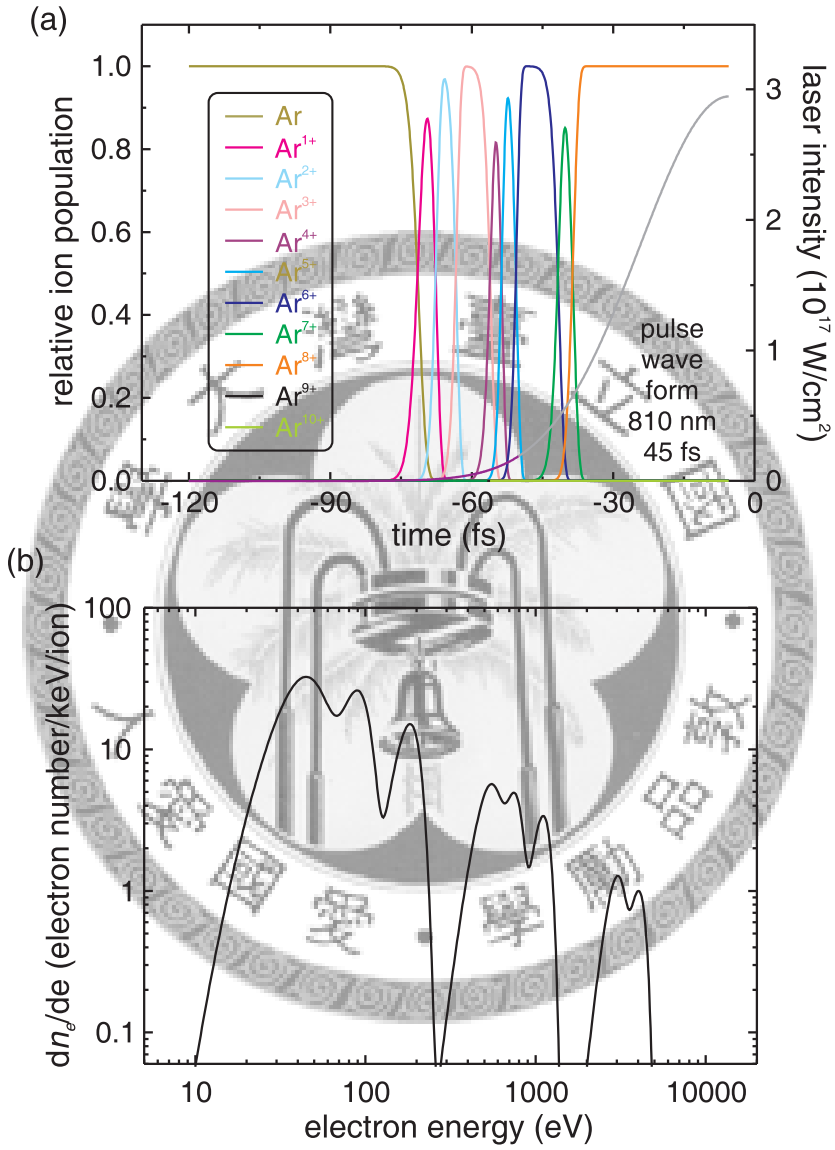

Figure 2.9: (a) Calculated evolution of the relative population of argon ions by a circular-polarized laser pulse with a duration of 45-fs (FWHM), wavelength of 810 nm, and a peak intensity of 3×10^{17} W/cm^2. (b) Energy spectrum of the ionized electrons.

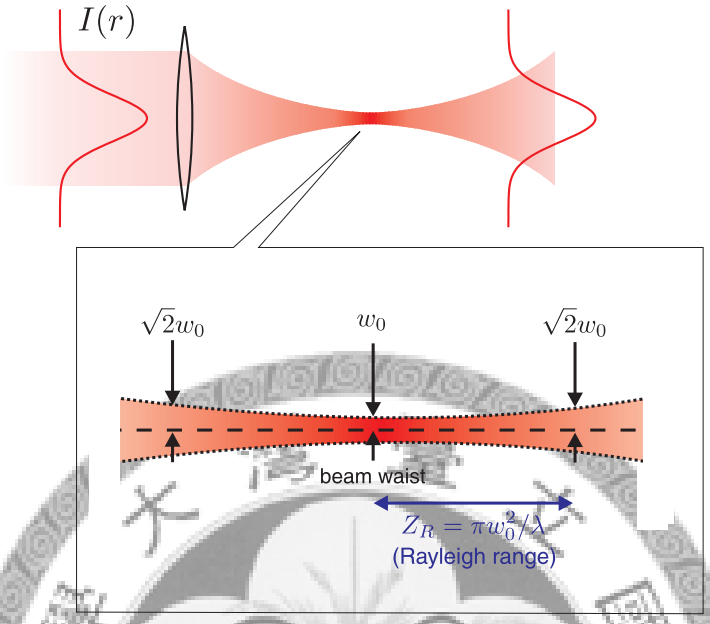

Figure 2.10: Diffraction of a focused Gaussian beam.

a 250-mJ, 38-fs, 810-nm Gaussian beam is focused to a spot of w_0=10 μm, the peak intensity can reach 4×10^{18} W/cm^2, but the Rayleigh range is only 0.4 mm. There is always a tradeoff between the interaction length and the maximum peak intensity. Moreover, these laser pulses propagate with an intensity which is far above the ionization threshold of atoms. This will make the laser beam break up due to filamentation [63, 64] or suffer from severe ionization-induced refraction which is shown in Figure 2.11. Both effects will drastically reduce the interaction length. Therefore, it is highly desirable to find a way to guide a high-intensity laser for a relatively long distance, as shown in Figure 2.12.

2.3.2 Guiding Condition of a Plasma Waveguide

For a focused laser beam to be guided at constant size in a waveguide, the diffractive effect of the laser beam should be compensated for the focusing effect of the waveguide. The diffractive defocusing contribution is $R_D = \delta z(1 + Z_R^2/\delta z^2) \approx Z_R^2/\delta z$, where Z_R is the Rayleigh range. On the other hand, the focusing contribution can be written as $R_F \approx w_0^2/(2\Delta n \delta z)$. When $R_F = R_D$, a focused Gaussian beam will maintain a flat phase front. The

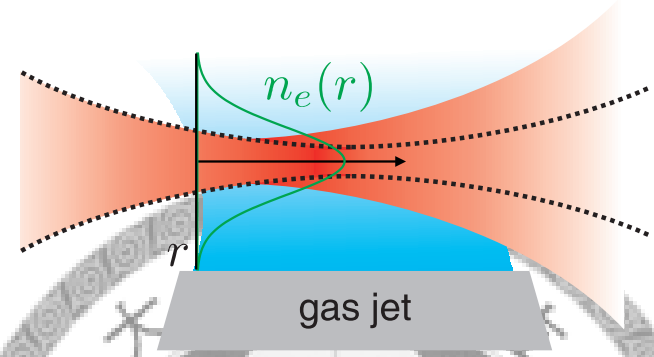

Figure 2.11: The effect of ionization-induced refraction. Dotted line represents the diffraction of a focused Gaussian pulse without ionization-induced refraction.

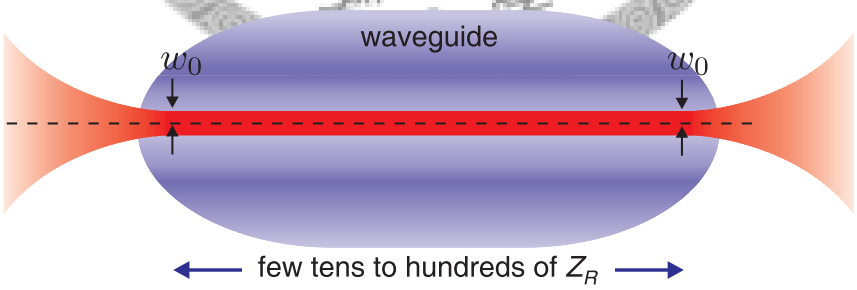

Figure 2.12: A Gaussian beam is guided in a plasma waveguide.

guiding condition can be written as

$$\Delta n^{min} = \frac{\lambda^2}{2\pi^2 w_0^2}\,. \tag{2.16}$$

In an underdense plasma, the refractive index is

$$\begin{aligned} n &= \sqrt{1-\frac{N_e}{N_{cr}}} \\ &= \sqrt{1-\frac{4\pi e^2 N_e}{m_e\omega^2}} \\ &\approx 1-\frac{2\pi e^2 N_e}{m_e\omega^2}\,, \end{aligned} \tag{2.17}$$

where $N_{cr} = m_e\omega^2/4\pi e^2$ is the critical electron density ($N_{cr} \approx 1.74\times10^{21}$ cm^{-3} for $\lambda = 810$ nm). ω, N_e, and m_e are the laser frequency, electron density, and electron mass, respectively. From Eq. 2.16 and Eq. 2.17, the minimum electron density difference necessary to guide a beam of spot size w_0 is determined by

$$\Delta N_e^{min} = \frac{1}{r_0\pi w_0^2}\,, \tag{2.18}$$

where $r_0 = e^2/m_e c^2 \approx 2.82\times10^{-13}$ cm is the classical electron radius. For $w_0 = 10$ μm, $\Delta N_e^{min} \approx 10^{18}$ cm^{-3}.

Note that the required density difference is independent of the guided laser wavelength. This is due to the decreasing plasma contribution to the refractive index with laser frequency, which is balanced by reduced diffraction at higher frequency for a given spot size. Since the guiding criterion does not depend on wavelength from infrared to soft x-ray, a plasma waveguide produced for guiding the pump laser pulse can also guide x-ray lasing.

2.3.3 Formation of a Plasma Waveguide

The plasma waveguide is formed through the hydrodynamic evolution of a laser-produced plasma in a gas. Initially the focused laser pulse (line focus) ionizes the neutral gas by optical-field ionization to provide seed electrons. The intensities used here are sufficient for multiphoton ionization of all or a substantial fraction of the atoms in the gases. If the pulse duration is longer

than the average electron-ion collision time, the seed electrons can be efficiently heated by laser pulse via inverse bremsstrahlung (IB) heating [65]. In addition, the long heating pulse should have a relatively low intensity, since the collisional frequency is reduced for large quiver velocities [66]. Then the heated energetic electrons collisionally ionize the ions or atoms and thus increase the electron density. After that there are more electrons to be involved in the electron-ion collisions, which enhances the IB heating. Such a positive feedback process is called a seeded avalanche breakdown [49]. The resultant dense hot line-shaped plasma begins to expand outwards. At that moment, the heated electrons pull the cooler ions radially outward, and the plasma expands at the local ion speed $c_s = \sqrt{< Z > k_B T_e / m_i}$. The plasmas in the expanding front collide with surrounding ions and atoms in the relative cold weakly ionized gas. These collisions lead to a density buildup at the boundary between the two regions, forming a shock front. After a period(a few nanoseconds), the on-axis plasma electron density is greatly reduced, while the plasma electron density at the encircling outer region builds up as a result of collisional ionization by the outgoing electrons and ions. Therefore, a cylindrically symmetric plasma with an on-axis electron density lower than that at the radially outer region is produced. If the difference in electron density between the on-axis and the beam radius positions is larger than that stated in Eq. 2.18, a plasma waveguide capable of guiding a laser pulse is produced.

2.3.4 The Axicon Ignitor-Heater Scheme

For a plasma waveguide, the plasma forming pulse must satisfy two conditions: (1) be sufficiently intense to create free electrons through multiphoton ionization and (2) be long and energetic but relatively low intensity to efficiently heat the plasma through IB heating. It is difficult to meet these two conditions by using a single laser pulse for ionization and heating. Therefore, a more efficient method, the axicon ignitor-heater scheme, is implemented in producing a plasma waveguide [51]. In this scheme, a short, low-energy, high-intensity ignitor pulse preionizes the gas through multiphoton ionization to produce a small concentration of seed electrons. A long, high-energy, low-intensity heater pulse arrives later to heat the preformed plasma efficiently by IB absorption and thereby drives the formation of the plasma waveguide. For comparison, here the total energy of the ignitor and heater is set to be constant. When only a short laser pulse is used, even though it has sufficient energy to ionize the gas, the pulse duration is too short to heat the plasma

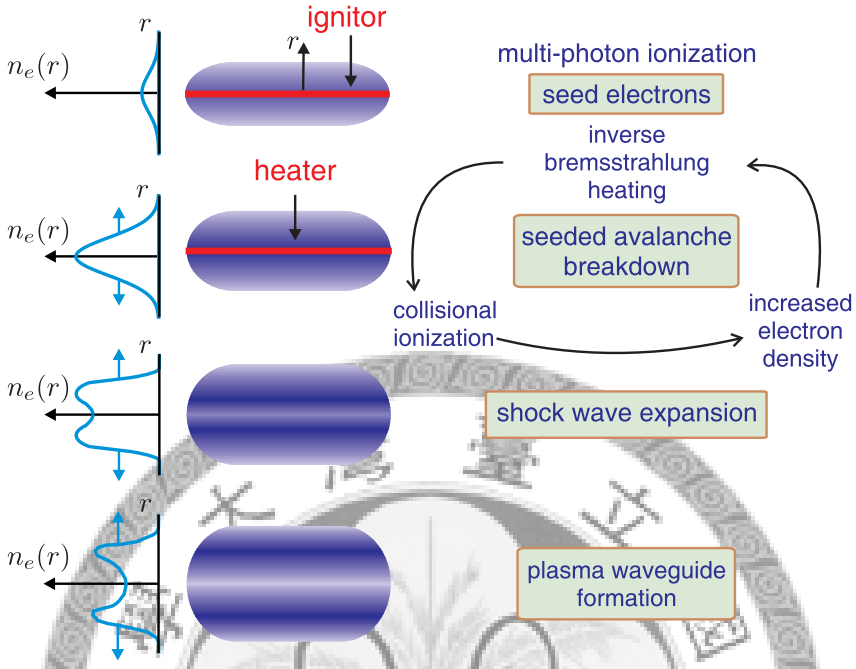

Figure 2.13: Fabrication of a plasma waveguide using the axicon ignitor-heater scheme.

efficiently via IB absorption. When only a long pulse is used, the laser intensity is too low to produce seed electrons so there is no IB absorption to drive the formation of the plasma waveguide. This shows the great efficiency of such a method. Figure 2.13 illustrates the fabrication of a plasma waveguide using the axicon ignitor-heater scheme.

In this scheme, the ignitor and heater are focused by an axicon to a line focus on the gases. An axicon is a conical polished glass that axially symmetrically converts light rays to a continuous range of points extended along the axis [67]. Figure 2.14 illustrates a laser beam focused by an axicon. For an input ray normal to the plane side of the axicon with a base angle α, the ray is focused on the optical axis(here, the z axis) with an angle γ. γ can be calculated from Snell's law $n \sin\alpha = \sin(\alpha + \gamma)$. The rays at the input position ρ are related to a distance z along the axis by the relation

$$z(\rho) = \rho \left[\frac{1}{\tan\gamma} - \tan\alpha \right] , \tag{2.19}$$

where $z = 0$ is at the axicon tip. In Fig. 2.14, a hole 5 mm in diameter at the center of the axicon allows the passage of the pump pulse of the soft x-ray laser. Figures 2.16 (b) and (c) show the transverse beam profiles of the

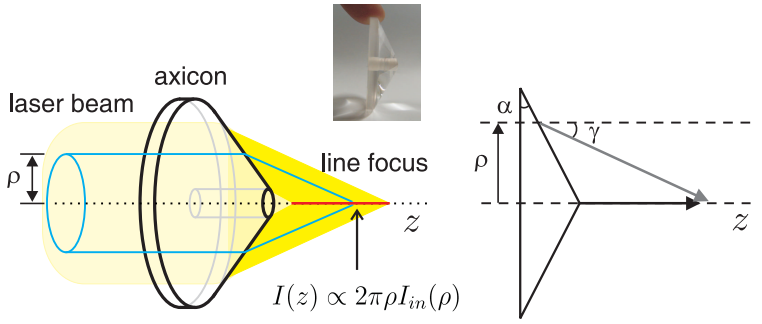

Figure 2.14: Line focusing by an axicon.

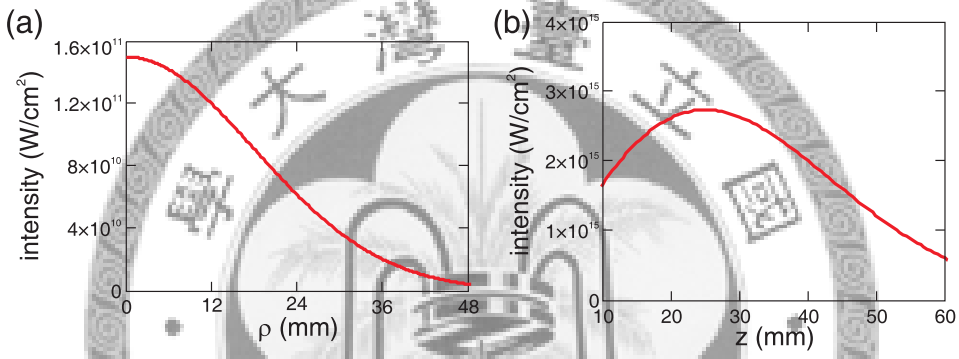

Figure 2.15: Axial intensity distribution of a Gaussian beam focused by an axicon. (a) shows the transverse intensity distribution of a 55-mJ, 60-fs input Gaussian beam with a 40-mm clear aperture in FWHM. (b) shows the axial intensity distribution of a Gaussian beam focused by an axicon.

ignitor and heater, respectively. The intensity distribution of the laser pulse along the optical axis is [68, 69]

$$I(z) = \frac{\pi k \sin\gamma}{2} \frac{z}{\frac{1}{\tan\gamma} - \tan\alpha} I_{\text{in}}\left[\rho(z)\right] \frac{(1+\cos\gamma)^2}{4}. \tag{2.20}$$

For example, by using an axicon with 30° base angle and a refractive index of 1.45, a 55-mJ, 60-fs Gaussian beam with a 40-mm clear aperture can be focused to a line focus of >2 cm in length with an intensity above 2×10^{15} W/cm^2, which is shown in Fig. 2.15.

However, in our experiment, the slit nozzle used to produce the gas jet is only 1-cm long. This means the half the length of the 2-cm-long line focus is useless. To overcome this problem, a convex lens with a 40-cm focal length and a hole 2 cm in diameter at the center is used in the experiment. This

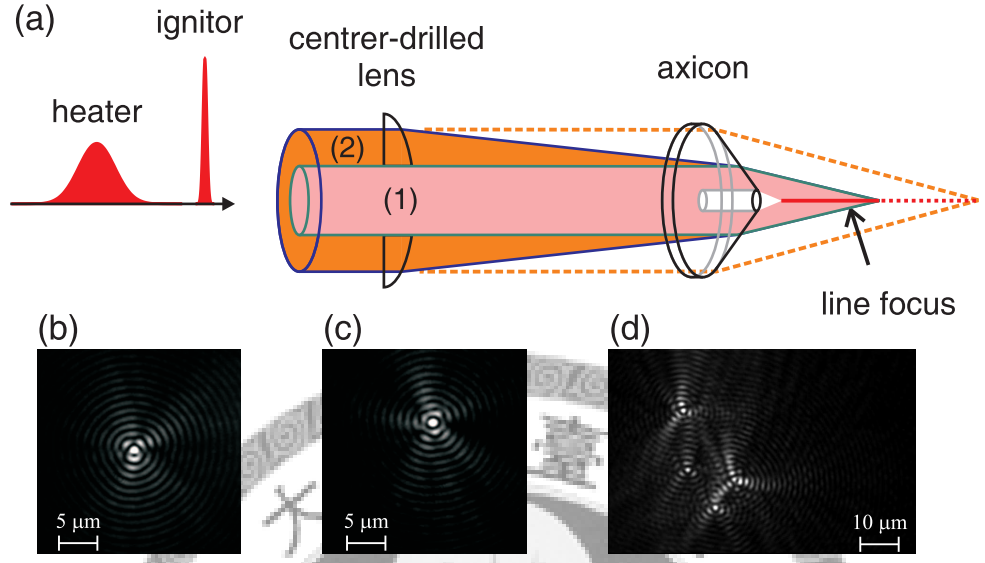

Figure 2.16: (a) Modified axicon-ignitor-heater scheme, where a convex lens of 40-cm focal length with a hole at the center 2 cm in diameter is put in front of the axicon at a distance of 20 cm. (b) and (c) are images of the beam profile of component (1) for the ignitor and heater, respectively. (d) shows the image of two components for the ignitor and heater pulses in the modified axicon ignitor-heater scheme.

convex lens is located in front of the axicon, as shown in Fig. 2.16(a). The input laser beam can be divided into two parts, component (1) and component (2), by this convex lens. Component (1), with a 2-cm clear aperture, passes through the center hole of the lens and is focused to a 1-cm-long line focus by the axicon. Figure 2.16(b) and (c) show the transverse beam profiles of component (1) for the ignitor and heater, respectively. Component (2) is a donut-shaped circle with a 2-cm inner diameter and 4-cm outer diameter and is focused by the convex lens before the axicon. Next, it is further focused by the axicon to another 1-cm-long line focus. At this time, the line focus moves closer to the axicon because of the prior focusing by the convex lens. By adjusting the position of the convex lens, we can concentrate the laser energy in a length (∼1-cm) matching that of the gas jet to increase the uniformity of the longitudinal intensity distribution. Figure 2.16(d) shows the transverse beam profiles of the focused ignitor and heater when a convex lens is put in front of the axicon, and Figure 2.17 show the modified longitudinal intensity distribution of the line foci for the ignitor and heater.

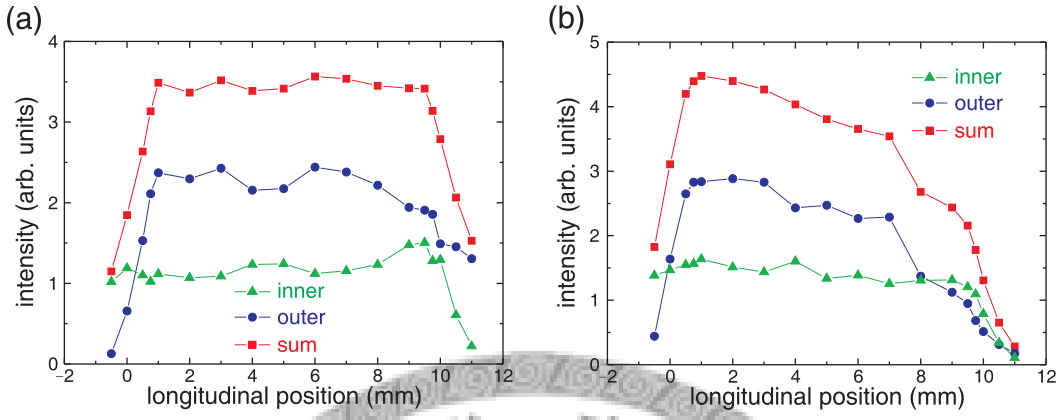

Figure 2.17: Longitudinal intensity distribution of the line foci of the ignitor (a) and the heater (b) in the modified axicon ignitor-heater scheme.

2.4 System Design and Configuration

The experimental layout is shown in Fig. 2.18. A 45-fs circularly polarized pump pulse is used to prepare the lasing ionization stage through optical-field ionization and heating of the ionized electrons. It is focused with an off-axis parabolic mirror of 30-cm focal length onto a clustered gas jet. The focal spot size of the pump pulse is 10-μm diameter in full width at half maximum (FWHM) with 85% energy enclosed in a Gaussian-fit profile. A motorized quarter-wave plate is used to vary the pump polarization. Two laser pulses, referred to as the ignitor and the heater, are used to produce a plasma waveguide. The ignitor is 45 mJ in energy, 45 fs in duration, and p-polarized (horizontally polarized), and the heater is 300 mJ in energy, 160 ps in duration, and s-polarized (vertically polarized). The ignitor-heater separation is fixed at 200 ps. After being combined by a thin-film polarizer, these two pulses, with 4-cm diameter in clear aperture propagate collinearly and are then focused by an axicon of 30° base angle to a line focus of >2-cm length in FWHM. The transverse profiles of the ignitor and the heater are both a Bessel distribution with an intensity FWHM of 1.1 μm. A hole of 5-mm diameter at the center of the axicon allows passage of the pump pulse. To increase the efficiency of waveguide fabrication a convex lens of 40-cm focal length with a hole of 2-cm diameter at the center is put in front of the axicon to concentrate the laser energy in a length (∼1-cm) matching with that of the gas jet and to increase the uniformity of the longitudinal intensity distribution. The line focus overlaps with the propagation path of the pump pulse in the gas jet. A photo of the experimental setup is shown in Fig. 2.22.

The clustered gas jet used for this experiment is produced from a pulsed valve with a 1-cm-long slit nozzle. In early experiments, it was difficult to find a good guiding condition for the pump pulse and the guiding efficiency was relatively low and unstable [70, 71]. This can be ascribed to the slowly varing density distribution at the edges of the gas-jet profile. The dashed line in Figure 2.19(c) shows the density distribution of the 2.5-mm region at one side of the original 5-mm slit nozzle. The atom density is retrieved from the interferogram in Fig. 2.19(a). A 750 μm-long slowly rising region appears at the boundary. Because the low-density region provides much fewer seed electrons to drive the formation of the plasma waveguide, it cannot make a suitable density barrier for supporting the guiding of the pump pulse. To overcome this problem, a 50 μm-thick metal sheet is attached to the nozzle edge to block the low-density area. The modified gas profile is shown in Fig. 2.19(c) (solid line). Here the atom density is retrieved from the interferogram in Fig. 2.19(b). The ascending region is greatly reduced to 250 μm after the modification. By applying this modification to the 1-cm slit nozzle used in this experiment, we can get a gas-jet profile with a flat-top region of 8-mm length and a sharp boundary of 500-μm length at both edges along the long axis. The gas-jet profile is measured by transverse Mach-Zehnder interferometry, and the result is shown in Fig. 2.20. With this treatment, the density barrier of the plasma waveguide at the boundary is enhanced, providing a more stable guiding condition for the pump pulse.

Four main optical diagnostic tools are used in this experiment. The first, Mach-Zehnder interferometry, with a probe pulse that passes transversely through the cluster jet, is used to measure the density distribution of electrons. The probe pulse of 15-mm diameter is split from the second stage amplifier of the 10-TW laser system and then compressed to a 45-fs duration by an independent compressor. It is imaged onto a 14-bit charge-coupled device (CCD) camera by a lens with a focal length of 500 mm. With an objective length of 740 mm and an image length of 3170 mm, the magnification of the interferogram imaging system was 4.3×. The second tool is a relayed imaging system for measuring the beam profile of pump pulses at the exit of the gas jet. It consists of a movable wedge, a pair of lens, an objective lens, and a 14-bit CCD camera. The third is an online imaging system for doing spatial overlap between the pump beam and waveguide-forming pulses in air and vacuum. It consists of an objective lens, a movable aluminum mirror, and a 14-bit CCD camera. The last is a home-made flat-field grazing-incidence x-ray spectrometer for measuring the spectrum and angular distribution of x-ray lasing in the direction of pump-laser propagation. In contrast to traditional x-ray spectrometers, which have only a concave grating and lead to

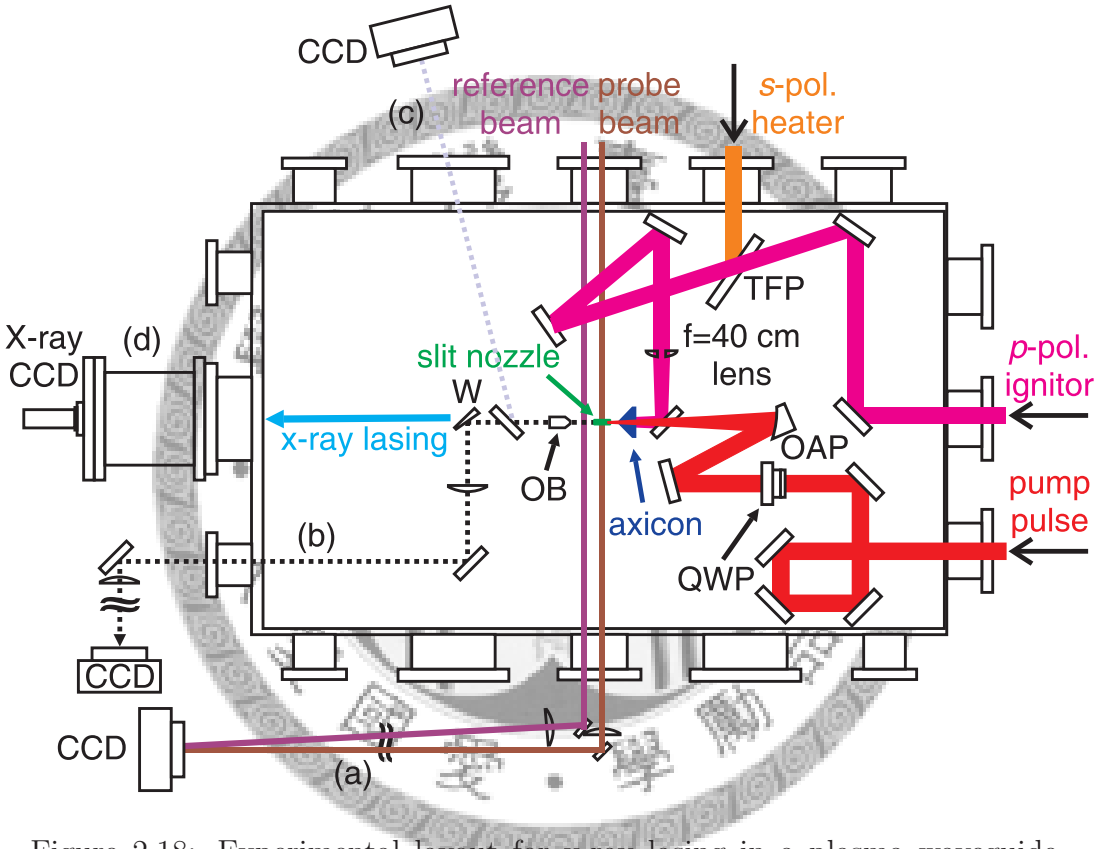

Figure 2.18: Experimental layout for x-ray lasing in a plasma waveguide. OAP: off-axis parabolic mirror, QWP: quarter-wave plate, TFP: thin-film polarizer, W: wedge, OB: objective, CCD: charge-coupled device. Four diagnostic tools were used: (a) interferogram, (b) relayed imaging system, (c) on-line imaging system, and (d) flat-field spectrometer.

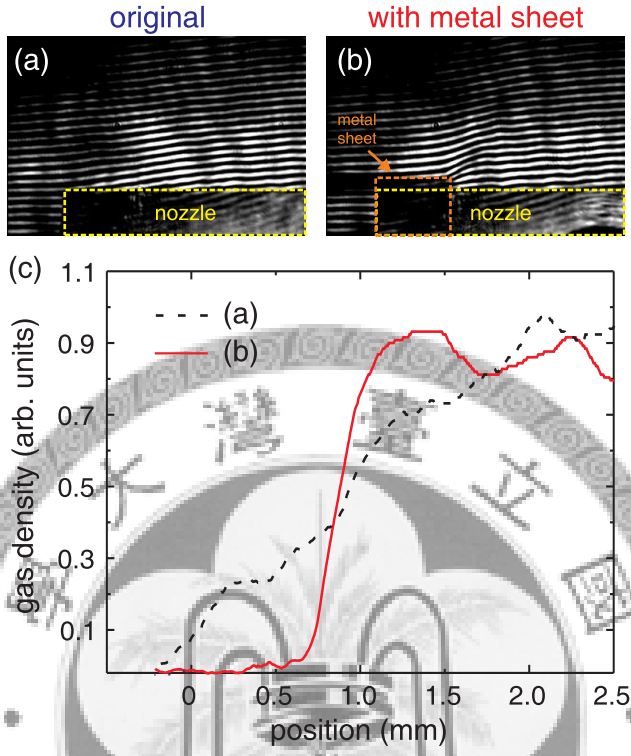

Figure 2.19: (a) Interferogram of the gas jet from the original 5-mm slit nozzle. (b) Interferogram of the gas jet from a 5-mm slit nozzle with the edge blocked by a 50-μm-thick metal sheet. (c)Gas profiles retrieved from (a) (dashed line) and (b) (solid line).

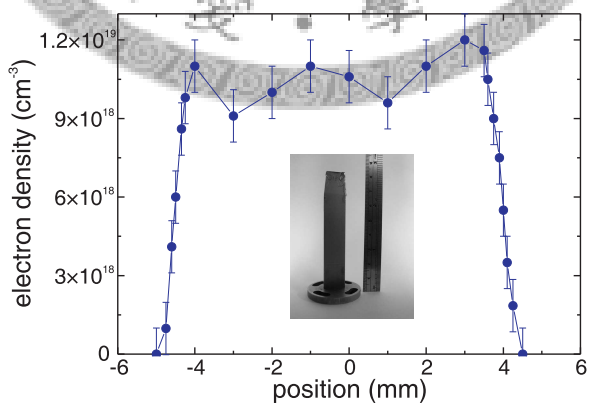

Figure 2.20: Gas profile of the hydrogen jet from the modified 1-cm slit nozzle. A photo of the 1-cm-long slit nozzle is shown in the inset.

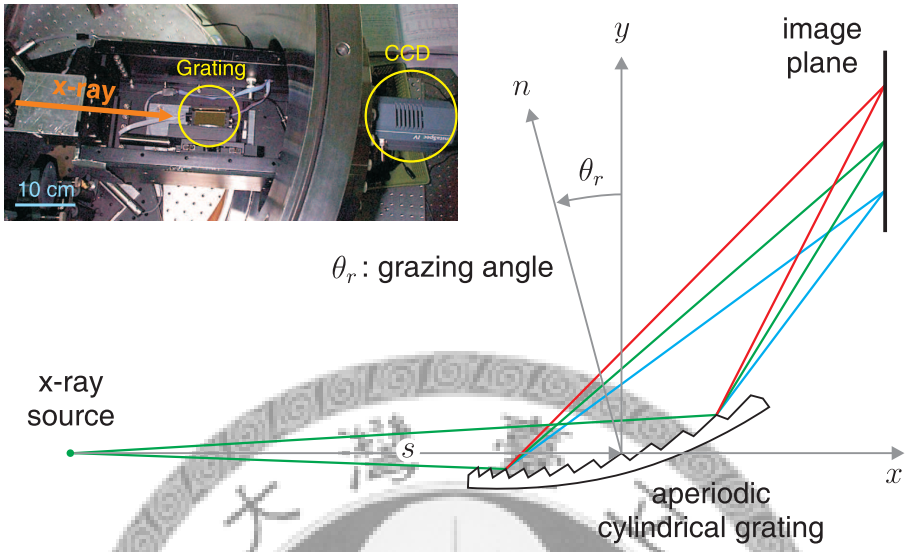

Figure 2.21: Illustration of the flat-field spectrometer. Inset shows a photo of the home-made flat-field spectrometer. Grating: 1200-line/mm aperiodically ruled cylindrical grating, CCD: 16-bit back-illuminated soft x-ray CCD camera.

a curved image plane, a flat-field spectrometer (FFS) uses a concave grating with varied groove spacing to produce a flat image plane [72, 73]. A flat image plane is desirable for the use of an x-ray CCD camera, microchannel plate, or streak camera to achieve online, real-time, and fully computerized data acquisition. The FFS used here consists of a 1200-line/mm aperiodically ruled cylindrical grating (001-0437, Hitachi) and a back-illuminated 16-bit x-ray CCD camera (DX420-BN, Andor Technology), as shown in Fig. 2.21. The spectral range of this FFS is 5 - 60 nm and the resolution is 0.05 nm. Two 0.25-μm-thick aluminum filters are used to block the transmitted pump laser pulse and attenuate x-ray emission. A dipole magnet with a magnetic field of 1.8 kG, is employed to deflect the electrons emitted from the interaction region to prevent false signals in the soft x-ray CCD camera. From the known grating reflectivity, filter transmittance, and CCD response, the approximate absolute number of x-ray photons is determined.

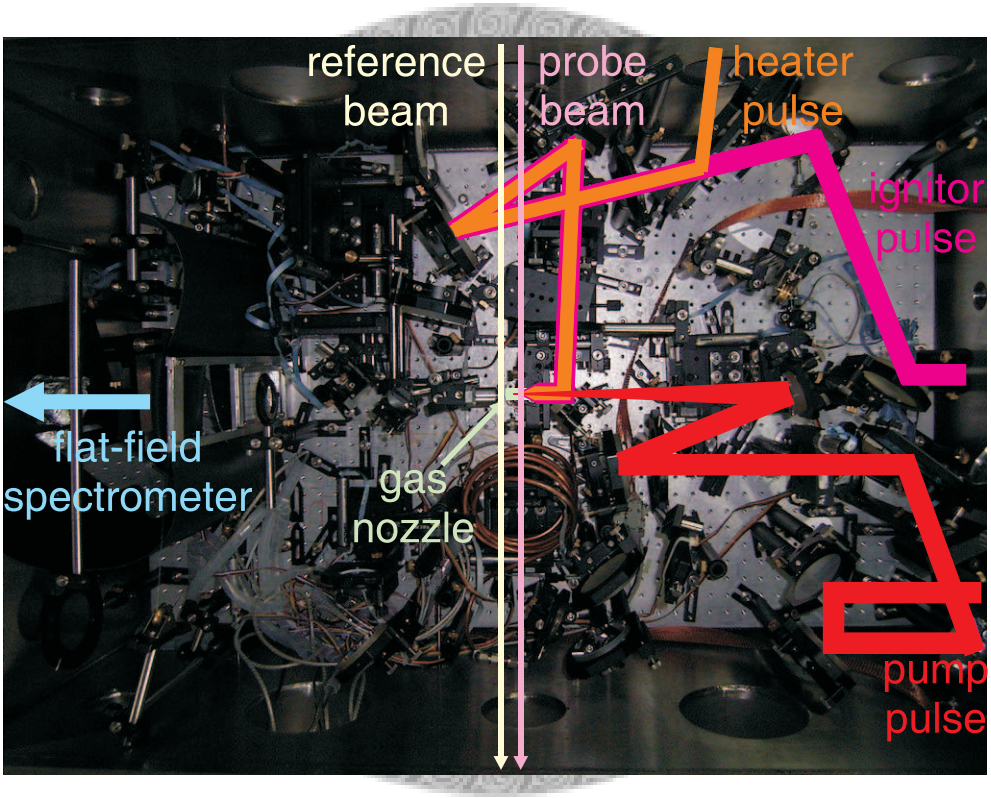

Figure 2.22: Photo of the experimental setup.

2.5 Enhancement of Optical-Field-Ionization Soft X-Ray Lasers By an Optically Preformed Plasma Waveguide

Without a plasma waveguide, the maximum x-ray lasing of Ni-like krypton at 32.8 nm is observed at an atom density of 8.0×10^{17} cm^{-3} and a pump focal position of 2.75 mm behind the entrance of the gas jet. The pump pulse has an energy of 235 mJ, a duration of 45 fs, and is circularly polarized. The condition for maximum output is known to be determined by the optimal balance between pump beam convergence and ionization-induced refraction that produces the longest gain region and the shortest x-ray reabsorption region [42, 74]. Figure 2.23(a) shows an interferogram taken at 10 ps after the pump pulse has passed through the gas jet. The amount of fringe shift decreases along with the laser propagation and almost vanishes in the final 2-mm region, indicating that the pump intensity at the end of the gas jet is too low to ionize the gas. This means that the effective gain region is limited by beam diffraction and ionization-induced refraction, even though the laser parameters have been optimized. The number of photons at the 32.8-nm lasing line is 2×10^8, and the x-ray beam divergence is 15 mrad in FWHM. The x-ray spectrum and the angular distribution are shown in Fig. 2.24(a) and (b), respectively. Figure 2.23(b) shows an interferogram of the plasma taken at the same condition as in Fig. 2.23(a) except that the krypton atom density is raised to 1.6×10^{19} cm^{-3} and the pump focal position is moved to 500 μm behind the entrance of the gas jet, corresponding to the beginning of the flat-top region of the gas profile. Although the increase in ion density should lead to a larger lasing gain, severe ionization-induced refraction drastically reduces the length of the gain region, as indicated by the much shorter length of the fringe-shifted region compared to (a), and thus no x-ray lasing is observed at this condition. The images in Fig. 2.23(c) and (d) show the beam profiles of the pump pulse at the entrance and exit of the gas jet, respectively. The divergent profile in Fig. 2.23(d) reveals the much lower intensity of the pump pulse at the exit, which is consistent with the results in the interferogram.

To overcome the adverse effect of ionization-induced refraction on a longitudinally pumped x-ray laser, a plasma waveguide based on the axicon ignitor-heater scheme (described in Sec. 2.3.4) is implemented in the experiment. The interferograms in Fig. 2.25(a) and (b) show the plasma channels at a krypton atom density of 1.6×10^{19} cm^{-3} for only a 45-mJ ignitor and only a 225-mJ heater. They are taken after 2.71 ns and after 2.51 ns, respectively.

Figure 2.25(c) shows the plasma waveguide at 2.5 ns after the heater with a 45-mJ ignitor, 225-mJ heater, 200-ps pulse separation, and 1.6×10^{19}-cm^{-3} krypton atom density. A uniform pure krypton plasma waveguide of 9-mm long is produced. The interferogram in Figure 2.25(d) shows the plasma waveguide taken at 10 ps after the pump pulse has passed through the gas jet under the same conditions in Fig. 2.25(c). The 235-mJ pump pulse is circularly polarized with a focal position of 500 μm behind the entrance of the gas jet and a delay of 2.5 ns after the heater. The images in Fig. 2.25(e) and (f) show the beam profiles of the pump pulse at the entrance and exit of the plasma waveguide, respectively, indicating that the pump pulse is well guided over the entire length of the plasma waveguide with a guided beam size of $<$15 μm in FWHM.

In the past, it was believed that it is difficult to guide an intense pump pulse for producing an OFI x-ray laser in a plasma waveguide of pure high-atomic-number gas. This is because the ionization of the on-axis ions is stronger than that of those in the outer region due to the transverse intensity distribution of the guided laser pulse, which tends to lower the density barrier and thus destroys the guiding condition [44, 45]. However, our experiment shows that under suitable conditions an intense pump pulse can even raise the density barrier(the difference between the peak electron density and the on-axis density) to improve guiding instead of degrading it. Figure 2.26 shows the radial electron density profiles retrieved from Fig. 2.25(c) and (d). At 2.5 ns after the heater pulse, the plasma waveguide evolves into one with an on-axis electron density of 4.1×10^{18} cm^{-3} and an electron density barrier of 1.3×10^{19} cm^{-3}. Right after the pump pulse has passed through the waveguide, both the on-axis electron density and the density in the barrier region increase, resulting in an on-axis electron density of 1.3×10^{19} cm^{-3} and an increased electron density barrier of 2.0×10^{19} cm^{-3}. The action of the pump pulse actually increases the density barrier of the plasma waveguide. The increase results from the transverse intensity distribution of the guided pump pulse. Although the average on-axis ionization stage is raised from 2.5 to 8 by the pump pulse, as inferred from Fig. 2.25(b), the average ionization stage at the barrier position is also increased, for instance, from 1 to 1.9, leading to a larger electron density barrier.

Figure 2.27(a) and (b) show the x-ray spectrum and the angular distribution, respectively, for a 32.8-nm Ni-like Kr laser by using a pure Kr plasma waveguide. The pump energy is 235 mJ, the heater energy is 225 mJ, the heater-pump delay is 2.5 ns, and the atom density is 1.6×10^{19} cm^{-3}. With the plasma waveguide, the x-ray lasing photon number is dramatically en-

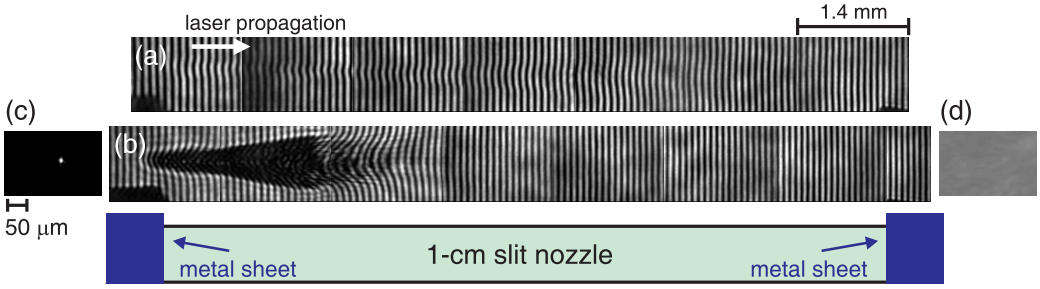

Figure 2.23: Interferograms of the plasma taken at 10 ps after the 235-mJ circular-polarized pump pulse has passed through the gas jet. (a) Using only the pump pulse with a focal position at 2.75 mm behind the entrance of the gas jet. Krypton atom density = 8.0×10^{17} cm^{-3}. (b) Using only the pump pulse with a focal position at 500 μm behind the entrance of the gas jet. Krypton atom density = 1.6×10^{19} cm^{-3}. Beam profiles of the pump pulse at the entrance and exit of the gas jet for the condition of (b) are shown in (c) and (d), respectively.

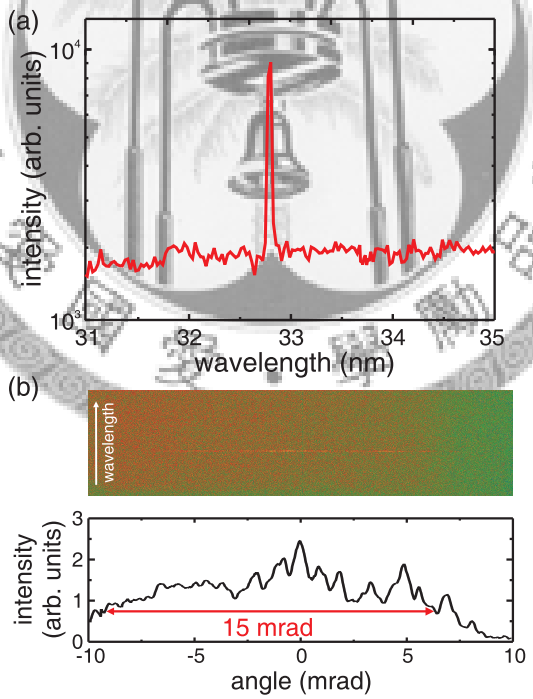

Figure 2.24: (a) X-ray emission spectrum and (b) angular distribution in the propagation direction of the pump pulse for only a 235-mJ circularly-polarized pump pulse with a focal position at 2.75 mm behind the entrance of the gas jet and a krypton atom density of 8.0×10^{17} cm^{-3}.

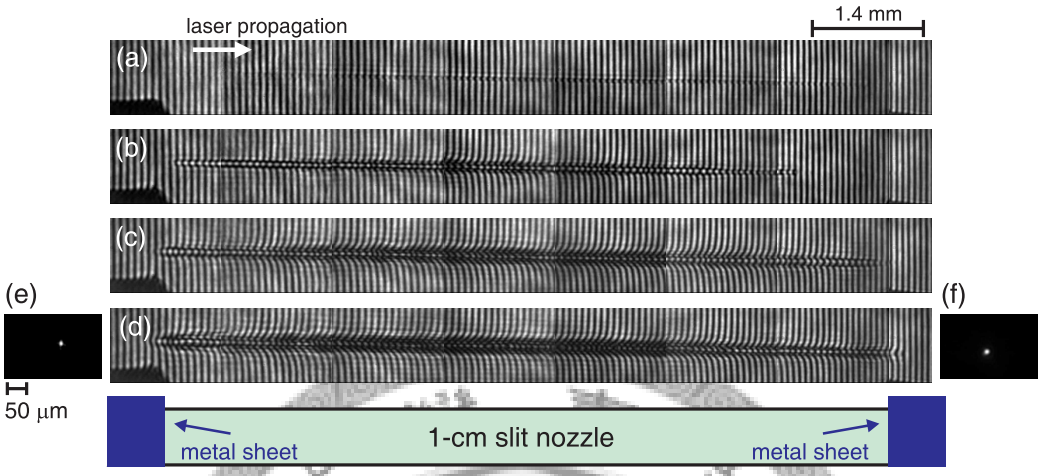

Figure 2.25: Krypton atom density = 1.6×10^{19} cm^{-3}. (a) Using only a 45-mJ ignitor. (b) Using only a 225-mJ heater. There is no pump pulse and the interferograms in (a) and (b) are taken after 2.71 ns and after 2.51 ns, respectively. (c) Using a 45-mJ ignitor pulse followed after 200 ps by a 225-mJ heater pulse. There is no pump pulse and the interferogram is taken at 2.51 ns after the heater pulse. (d) Interferograms of the plasma taken at 10 ps after the 235-mJ circularly-polarized pump pulse is guided by the plasma waveguide shown in (c). The beam profiles of the pump pulse at the entrance and exit of the gas jet for the condition of (d) are shown in (e) and (f), respectively.

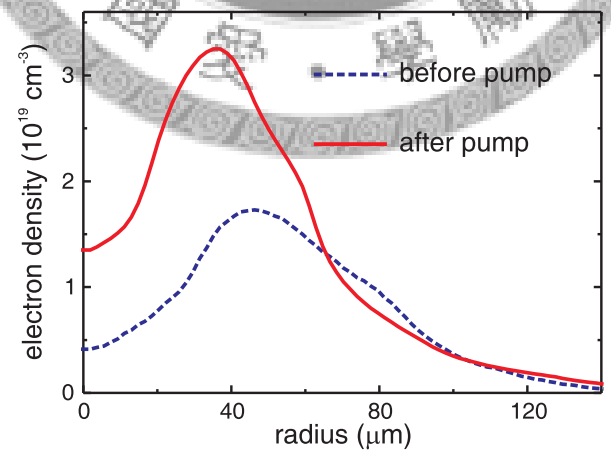

Figure 2.26: Radial electron density profiles of the plasma waveguide retrieved from Fig. 2.25(c) and (d).

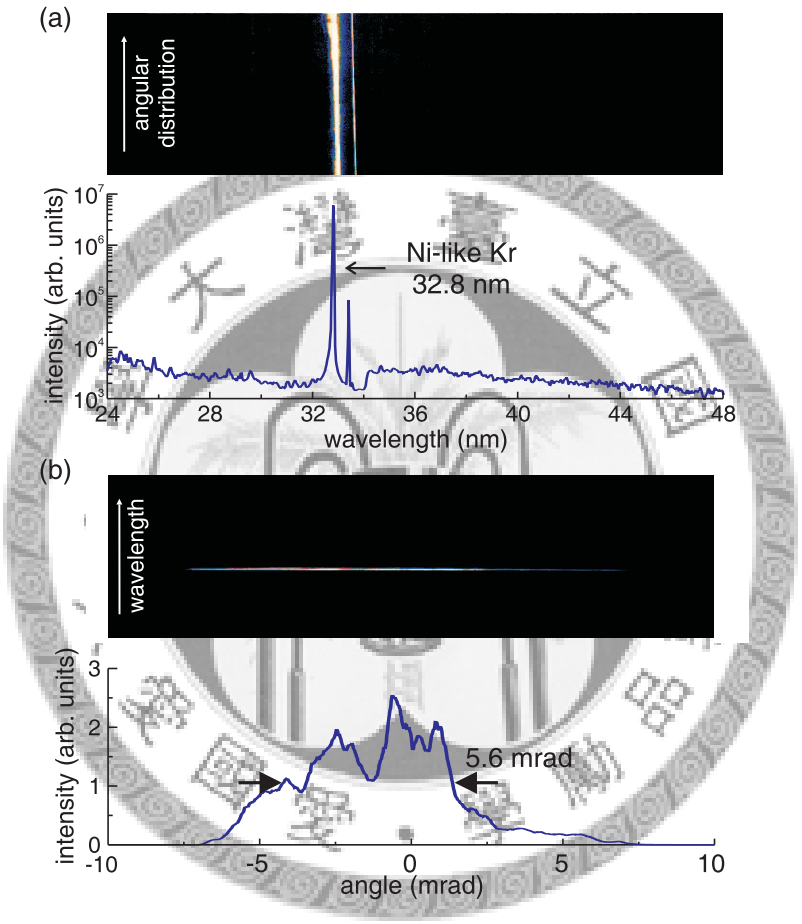

Figure 2.27: (a) X-ray emission spectrum and (b) angular distribution in the propagation direction of the pump pulse for a 235-mJ circularly-polarized pump pulse guided in a pure krypton waveguide with an atom density of 1.6×10^{19} cm^{-3}. The ignitor energy is 45 mJ, the heater energy is 225 mJ, the ignitor-heater separation is 200 ps, and the heater-pump delay is 2.5 ns.

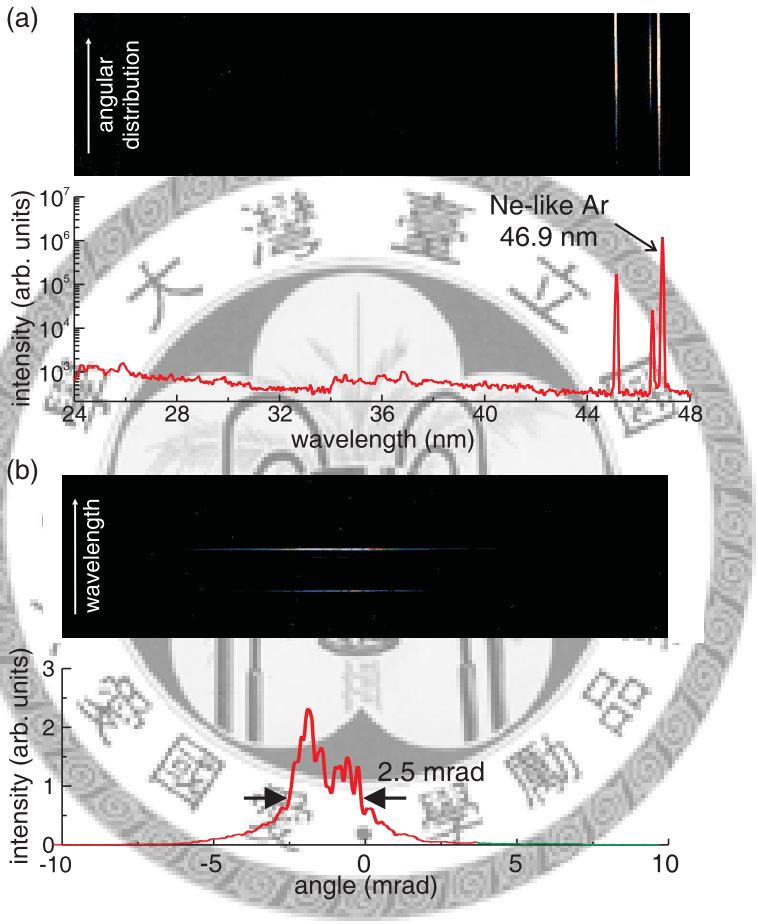

Figure 2.28: (a) X-ray emission spectrum and (b) angular distribution in the propagation direction of the pump puls for a 235-mJ circularly-polarized pump pulse guided in a pure argon waveguide with an atom density of 2.7×10^{19} cm^{-3}. The ignitor energy is 45 mJ, the heater energy is 325 mJ, the ignitor-heater separation is 200 ps, and the heater-pump delay is 1.5 ns.

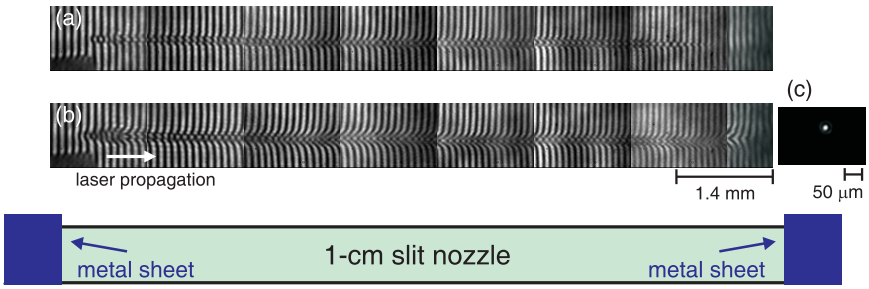

Figure 2.29: Interferograms of the plasma taken at 10 ps after the 235-mJ circularly-polarized pump pulse has passed through the gas jet for a 45-mJ ignitor, 325-mJ heater, 200-ps ignitor-heater separation, 1.5-ns heater-pump delay, and 2.7×10^{19}-cm^{-3} Ar atom density (a) without and (b) with the pump pulse. The beam profiles of the pump pulse at the exit of the plasma waveguide are shown in (c).

hanced by a factor of 400 compared to that with only the pump pulse at the optimal condition. The output reaches 8×10^{10} photon/pulse with 10% fluctuation and the x-ray beam divergence is decreased to 5.6 mrad in FWHM with 20% fluctuation. The divergence is close to the ratio of the waveguide diameter to the waveguide length. There is no lasing signal with only the waveguide-forming pulses. The increase in on-axis plasma electron density and the strong x-ray lasing observed when the pump pulse is turned on reveal that the x-ray lasing results from optical-field ionization of the gas driven by the pump laser pulse. In addition, clustering of the atoms occurs in the gas jet but does not effect the results because the clusters are easily disintegrated in advance by the ignitor and heater pulses before encountering the pump pulse [41]

Taking advantage of the high atom density and large gain length provided by such a plasma waveguide, OFI collisional-excitation x-ray lasing for the high-threshold low-gain transition at 46.9 nm in Ne-like argon was also achieved. In this case, the pump energy is 235 mJ, the heater energy is 325 mJ, the heater-pump delay is 1.5 ns, and the atom density is 2.7×10^{19} cm^{-3}. The output photon of the Ar laser was 3.4×10^9, and the beam divergence is 2.5 mrad at an atom density of 2.7×10^{19} cm^{-3}. The x-ray spectrum and angular profile for the 46.9-nm Ar^{8+} lasing are shown in Fig. 2.28(a) and (b), respectively. In contrast, no x-ray lasing occurs without the Ar plasma waveguide. Figure 2.29(a) shows an interferogram of the plasma waveguide taken at 1.5 ns after the heater, without the pump pulse. A uniform pure argon plasma waveguide of 9-mm length is produced. Figure 2.29(b) shows

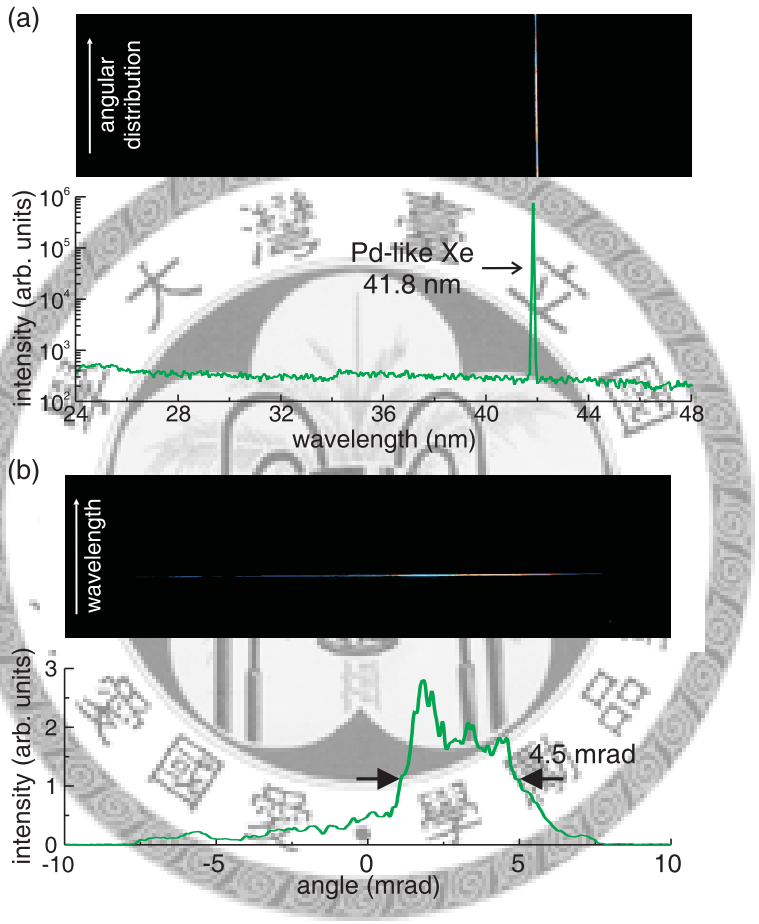

Figure 2.30: (a) X-ray emission spectrum and (b) angular distribution in the propagation direction of the pump pulse for a 225-mJ circularly-polarized pump pulse guided in a pure argon waveguide with an atom density of 1.4×10^{19} cm^{-3}. The ignitor energy is 45 mJ, the heater energy is 180 mJ, the ignitor-heater separation is 200 ps, and the heater-pump delays is 5.5 ns.

the interferogram of this plasma waveguide taken at 10 ps after the pump pulse has passed through the waveguide. The beam profile of the pump pulse at the exit of the plasma waveguide is shown in Fig. 2.29(c), indicating that the pump pulse is well guided over the entire length of the plasma waveguide with a guided beam size of <15 μm in FWHM. For the Ar plasma waveguide the transverse plasma electron density profile cannot be correctly retrieved and thus is not shown because of the large error caused by the small channel size. Similarly, a 41.8-nm Pd-like Xe x-ray laser was also demonstrated with a pure Xe plasma waveguide. The x-ray spectrum and angular distribution are shown in Fig. 2.30(a) and (b), respectively. The pump energy is 225 mJ, the heater energy is 180 mJ, the heater-pump delay is 5.5 ns, and the atom density is 1.4×10^{19} cm^{-3}. Under these conditions, the number of photons for the 41.8-nm x-ray lasing is 2.5×10^9 and the x-ray beam divergence is 4.5 mrad.

For the three lasing species, the small divergence angles of the main lasing lines can be ascribed to the high gain-length product and the guiding effect on the x-ray beam provided by the plasma waveguide. The strengths of both effects differ for the three cases due to the different operating conditions, resulting in different divergence angles. Without the preformed plasma waveguide (turning off the ignitor and the heater), the photon number of 32.8-nm Kr^{8+} lasing is reduced by 400 folds and the 46.9-nm Ar^{8+} lasing is not observed. In contrast, the photon number of 41.8-nm Xe^{8+} lasing with the plasma waveguide is lower than that obtained using a bare gas jet with optimal pump focal position and gas-jet length [41, 42]. This is because an optically preformed plasma waveguide of good guiding efficiency is generally limited to a small channel diameter (smaller guided spot size). Since 41.8-nm Xe^{8+} lasing requires only relatively low pump intensity, the small channel diameter has no advantage in raising the gain while limiting the transverse cross section of the gain region. Furthermore, the extension of the gain length by the plasma waveguide cannot lead to a dramatic increase in photon number since 41.8-nm Xe^{8+} lasing has a relatively high gain coefficient and thus can reach saturation in a short distance. Therefore, with optimal pump f-number and focal position, 41.8-nm Xe^{8+} lasing can yield more energy than that with an optically preformed plasma waveguide, because the optimal balance between pump beam convergence and ionization-induced refraction can produce a gain region with the largest transverse cross section and the largest gain length. The enhancement effect of an optically preformed plasma waveguide is more dramatic for x-ray lasing that requires higher pump intensity and has a smaller gain coefficient.

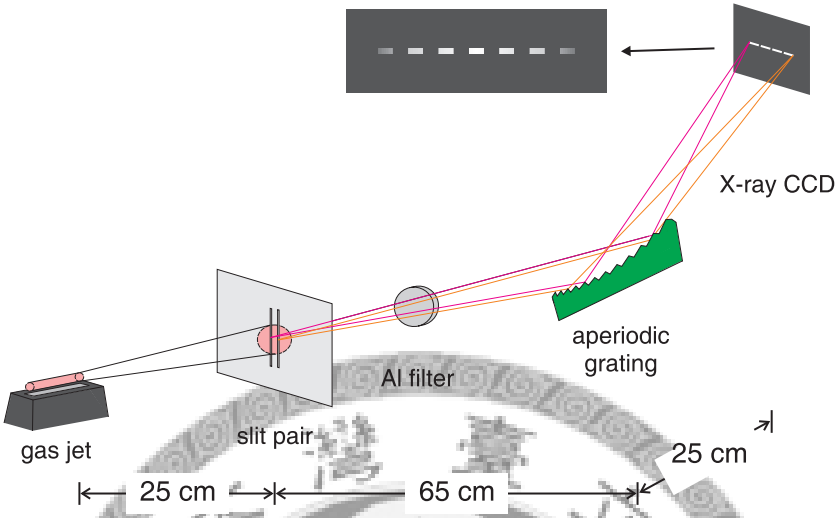

Figure 2.31: Experimental setup of the spatial coherence measurement for a 32.8-nm Kr^{8+} x-ray laser.

2.6 Spatial Coherence Measurement for the Ni-Like Kr Lasing in a Plasma Waveguide

As mentioned in Sec. 1.1, the soft-x-ray lasers have potential in many exciting applications, such as at-wavelength wavefront interferometry [75] and high-spatial-resolution microscopy [76, 77]. Since the spatial coherence of the laser plays a critical role in these applications, it is highly desirable to characterize the degree of spatial coherence for these sources. Measurements of the spatial coherence of different soft x-ray sources have been reported in the literatures [78, 79, 80, 81, 82]. Since waveguide-based soft-x-ray laser has significant ability to guide the intense pump pulses and the soft-x-rays, as shown by the small divergence and high output, it is of interest to measure the spatial coherence of an OFI soft-x-ray laser with a plasma waveguide. In this section, the measurement of the spatial coherence of a 32.8-nm soft x-ray laser with a pure Kr plasma waveguide is reported.

The spatial coherence is measured by using Young's double-slit interferometry. The setup is shown in Figure 2.31. For this measurement a 25-μm-thick Al foil with slit pairs of various slit separations is inserted in the x-ray beam path at 25 cm from the exit of the gas jet and before the entrance of the flat-field x-ray spectrometer. The slits are all 15-μm wide and are machined by our ultrashort high-intensity laser. For a typical double-slit coherence measurement, the relationship between fringe visibility V and the

spatial coherence factor μ_{12} is

$$\begin{aligned} V &= \frac{2\sqrt{I_1 I_2}}{I_1 + I_2}|\mu_{12}| \\ &= \frac{(I_{max} - I_{min})}{(I_{max} + I_{min})}, \end{aligned} \tag{2.21}$$

where I_1 and I_2 are the intensities at the two individual slits, and I_{max} and I_{min} are the maximum intensity and the minimum intensity, respectively, in the interferogram [83]. If the transverse beam profile is axially symmetrical and the silt pair is perfectly aligned, then $I_1 = I_2$, which leads to $V = |\mu_{12}|$. The spatial coherence can be acquired from the fringe visibility. However, I_1 may not equal to I_2 in a real case, implying that $V < |\mu_{12}|$. Thus, the measured fringe visibility would always underestimate the real degree of spatial coherence. Figure 2.32 shows the results for a 32.8-nm Kr^{8+} x-ray laser under the same condition as for Fig. 2.27(b). The images of double-slit interference fringes for slit separations of 65, 80, 100, and 143 μm are shown in Figs. 2.32(a)–(d), respectively. The results for larger slit separations are not used because the fringe visibility is then dominated by the finite pixel size of the x-ray CCD camera. Figure 2.32 shows the measured fringe visibility as a function of slit separation and the Gaussian-fit curve. By the definition that the coherent length is the slit separation at which the visibility falls to 0.61, the coherent length for this x-ray laser is measured to be 95 μm.

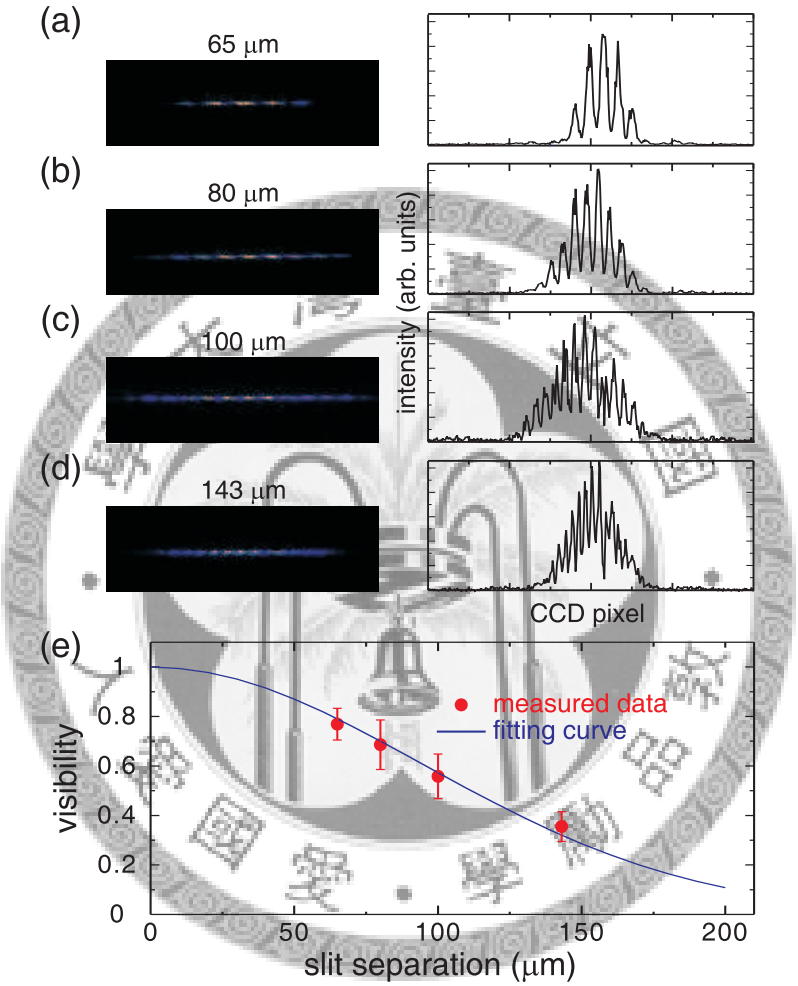

Figure 2.32: Transverse spatial coherence of a 32.8-nm Kr^{8+} x-ray laser under the same conditions as for Fig. 2.32(b) measured by Young's double-slit interferometry. Images (a) – (d) show the double-slit interference fringes for slit separations of (a) 65, (b) 80, (c) 100, and (d) 143 μm. The distance from the gas jet to the slit pairs is 25 cm. (e) shows the fringe visibility as a function of slit separation and its Gaussian-fit curve.

Chapter 3

Multi-line Waveguide-Based Optical-Field-Ionization Soft X-Ray Lasers

As stated in chapter 1, soft x-ray lasers have extensive applications in many areas. Soft x-ray lasers have a specific lasing wavelength depending on the energy difference between the atomic levels. If they can also be operated at different wavelengths, or even at several lasing lines simultaneously, they would be a more practical tool for scientific research. The waveguide-based optical-field-ionization (OFI) soft x-ray laser is one of the working mechanisms showing this multi-line feature. Under the same configuration of pump and waveguide-forming pulses, three strong lasing lines with different wavelengths can be achieved in pure xenon, krypton, and argon plasma waveguides. Because of the strong enhancement effect of the waveguide, one additional lasing line at 33.5 nm for a Ni-like krypton laser and two additional lasing lines at 45.1 nm and 46.5 nm for a Ne-like argon laser are observed. Moreover, simultaneous multi-species x-ray lasing at two different wavelengths is also demonstrated with a Kr/Ar mixed-gas plasma waveguide, and the ratio of the intensities of the two lasing lines can be easily tuned by varying heater energy.

In Sec. 3.1, the dependencies of x-ray lasing photon number on heater-pump delay, heater energy, pump energy, atom density, and pump polarization for 41.8-nm Xe^{8+} lasing, 32.8-nm Kr^{8+} lasing, and 46.9-nm Ar^{8+} lasing are presented and discussed. In Sec. 3.2, the cause of multiple lasing lines from the same ion species is described, and the correlation between the multiple lines is addressed. In Sec. 3.3, measurements of multi-species parallel

x-ray lasing in a Kr/Ar mixed-gas plasma waveguide are reported.

3.1 Parameter Space of X-Ray Lasing in a Pure-Gas Plasma Waveguide

Although the plasma waveguide has shown its power in the reduction of divergence and increase in the gain length of x-ray lasers, the degree of its influence on the three lasing species is very different. This can be ascribed to the different operating conditions for these soft x-ray lasers. In this experiment, to maximize the output photons of the x-ray laser, several parameters are optimized for a Pd-like Xe laser, Ni-like Kr laser, and Ne-like Ar laser. Due to the various characteristics of the three species, the optimal conditions are different.

For high-output x-ray laser, abundant ion species with the proper stage (8+ in this case) are necessary. This can be done by the OFI mechanism via appropriate control of the laser intensity. Although the intensities required for Xe^{8+}, Kr^{8+}, and Ar^{8+} ions can be calculated by the ADK theory, as stated in Sec. 2.2.1, another simple theoretical model is used here to estimate the ionization threshold intensity without running complicated simulations. This model supposes a combined potential formed by a superposition of the Coulomb potential with a static electric field [84]. As the external field strength is increased, the height of the Coulomb barrier is suppressed. If the field depression of the potential barrier exceeds the binding energy of an electron, ionization will occur rapidly. The superimposed potential is written as

$$V(x) = -\frac{Ze^2}{x} - eE_0x, \tag{3.1}$$

where Z refers to the residual charge seen by that electron, e is the electron charge, and E_0 is the strength of the electric field. The position of the barrier maximum, x_{max}, is found by setting $\partial V(x)/\partial x = 0$. Equating $V(x_{max})$ to the ionization potential (the binding energy of the electron), U_i, yields an expression for the critical electric field strength

$$E_{crital} = -\frac{U_i^4}{16e^6Z^2}. \tag{3.2}$$

Setting this static electric field equal to the peak electric field of the laser, we obtain the corresponding intensity which can be defined as the ionization

Element	I	II	III	IV	V	VI
Xe	12.13	21.21	32.10	46.70	59.70	71.80
Kr	14.00	24.36	36.95	52.50	64.70	78.50
Ar	15.76	27.63	40.47	59.81	75.02	91.01

Element	VII	VIII	IX	X	XI	XII
Xe	92.10	105.90	171.00	202.00	232.60	263.50
Kr	111.00	125.80	230.85	268.20	308.00	350.00
Ar	124.32	143.46	422.45	478.69	538.96	618.26

Table 3.1: The ionization potentials (eV) of Ar, Kr, and Xe atoms [6, 88].

threshold intensity [85, 86],

$$I_{threshold} = \frac{cU_i^4}{128\pi^6 Z^2}, \tag{3.3}$$

where U_i is the ionization potential of an ionized electron. Experiments by Augst *et al.* have shown that for a laser wavelength of 1 μm and pulse duration of 1 ps, the ionization of several noble gases can be accurately estimated by this Coulomb-barrier model [85]. Equation 3.3 shows that $I_{threshold}$ is proportional to U_i^4, and the ionization potential increases from Xe to Kr to Ar under the same charge state, as shown in Tab. 3.1. This means it is increasingly difficult to ionize atoms to the specific ion stages from Xe to Kr to Ar gases. Figure 3.1 depicts the threshold intensities of Xe, Kr, and Ar ions for the first ten charge states. For Xe^{8+} ion, Kr^{8+} ion, and Ar^{8+} ions, the ionization intensity thresholds are about 7.9×10^{15} W/cm^2, 1.6×10^{16} W/cm^2, and 2.7×10^{16} W/cm^2, respectively. On the other hand, the oscillator strengths for the Xe^{8+} $5d$ – $5p$ transition, Kr^{8+} $4d$ – $4p$ transition, and Ar^{8+} $3p$ – $3s$ transition are 0.7461, 0.6273, and 0.2053, respectively [87]. The higher ionization intensity threshold requires a higher pump laser intensity and the lower oscillator strength results in a smaller gain coefficient. Therefore, from 41.8-nm Xe^{8+} to 32.8-nm Kr^{8+} to 46.9-nm Ar^{8+}, OFI x-ray lasing is increasingly difficult to achieve because of the increasing ionization intensity threshold and decreasing oscillator strength of the lasing transition. For convenience, the lasing and optimal experimental parameters are summarized in the Tabs. 3.2 and 3.3, respectively.

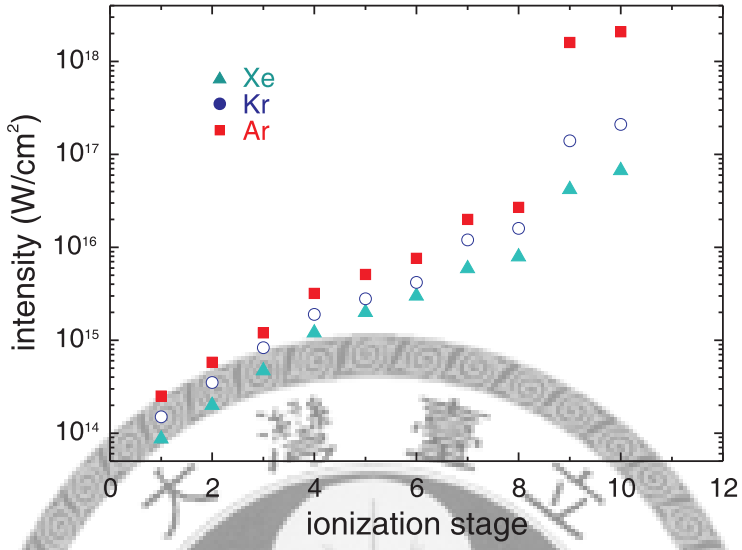

Figure 3.1: Threshold intensities of Xe, Kr, and Ar ions for the first 10 charge states.

Element *	Lasing wavelength	Photons/pulse	Divergent angle
Xe	41.8 nm	2.5×10^9	4.5 mrad
Kr	32.8 nm	8×10^{10}	5.6 mrad
Ar	46.9 nm	3.4×10^9	2.5 mrad

Table 3.2: The lasing parameters for Pd-like Xe, Ni-like Kr, and Ne-like Ar x-ray lasers.

Element	Pump energy	Heater energy	Pump delay	Atom density
Xe	225 mJ	180 mJ	5.5 ns	1.6×10^{19} cm^{-3}
Kr	235 mJ	225 mJ	2.5 ns	2.7×10^{19} cm^{-3}
Ar	235 mJ	325 mJ	1.5 ns	1.4×10^{19} cm^{-3}

* The ignitor energy is 45 mJ and the ignitor-heater separation is 200 ps for the three lasing lines.

Table 3.3: The optimal experimental parameters for Pd-like Xe, Ni-like Kr, and Ne-like Ar x-ray lasers.

Figure 3.2 shows the number of photons of 41.8-nm Xe^{8+}, 32.8-nm Kr^{8+}, and 46.9-nm Ar^{8+} lasing lines with a pure-gas plasma waveguide as a function of heater-pump separation. The other parameters are the same as that in Tab. 3.3. Optimal delays for maximum x-ray lasing for the three lasing lines are found to be 5.5 ns, 2.5 ns, and 1.5 ns, respectively. All the data points in this and the following figures represent the average of five laser shots, and the error bars represent the standard deviation. With increasing of heater-pump separation via hydrodynamic expansion, the plasma waveguide evolves into one with a larger channel diameter and a lower on-axis ion density. The increase in channel diameter leads to a larger transverse cross section of the gain region, resulting in an increased photon number. However, the correspondingly reduced pump intensity lowers the fraction of the lasing ion species when the pump intensity falls to the level of the ionization intensity threshold of the lasing ionization stage or lower, decreasing the gain coefficient. At the same time, the decreased on-axis ion density also lowers the gain coefficient. The trade-off between these three effects should result in an optimal heater-pump delay for maximum lasing photon number. Figure 3.3 shows the number of photons of 41.8-nm Xe^{8+}, 32.8-nm Kr^{8+}, and 46.9-nm Ar^{8+} lasing lines with a pure-gas plasma waveguide as a function of heater energy. The other parameters are the same as that in Tab. 3.3. Since a plasma waveguide evolves faster with increasing heater energy as a result of increased plasma temperature, an optimal heater energy is present for a fixed heater-pump delay due to the same trade-off mechanism.

A comparison between the optimal conditions for maximum lasing output for these three lasing lines shows that a higher heater energy and a shorter heater-pump delay should be used when changing the target from Xe to Kr to Ar. This can be ascribed to the difference in the ionization intensity threshold between the three cases. For Xe^{8+}, Kr^{8+}, and Ar^{8+} ions, the ionization intensity thresholds are about 7.9×10^{15} W/cm^2, 1.6×10^{16} W/cm^2, and 2.7×10^{16} W/cm^2, respectively. That is, the required pump intensity in the plasma waveguide increases when changing from Xe to Kr to Ar. Therefore, a higher heater energy and a shorter heater-pump delay should be used to produce a plasma waveguide of a smaller channel diameter, which leads to a smaller guided pump beam size and thus higher pump intensity, while maintaining a sufficient plasma density barrier for good guiding efficiency.

Figure 3.4 shows the number of photons for 41.8-nm Xe^{8+}, 32.8-nm Kr^{8+}, and 46.9-nm Ar^{8+} lasing lines with a pure-gas plasma waveguide as a function of pump energy. The other parameters are the same as in Tab. 3.3. An exponential dependence on pump energy at low pump energies is expected

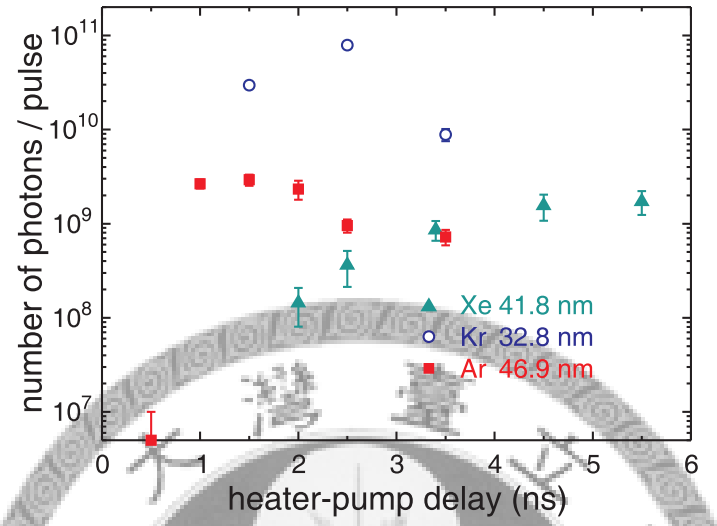

Figure 3.2: Number of photons of 41.8-nm Xe^{8+}, 32.8-nm Kr^{8+}, and 46.9-nm Ar^{8+} lasing lines with a pure-gas plasma waveguide as a function of heater-pump delay. The other parameters are the same as in Tab. 3.3.

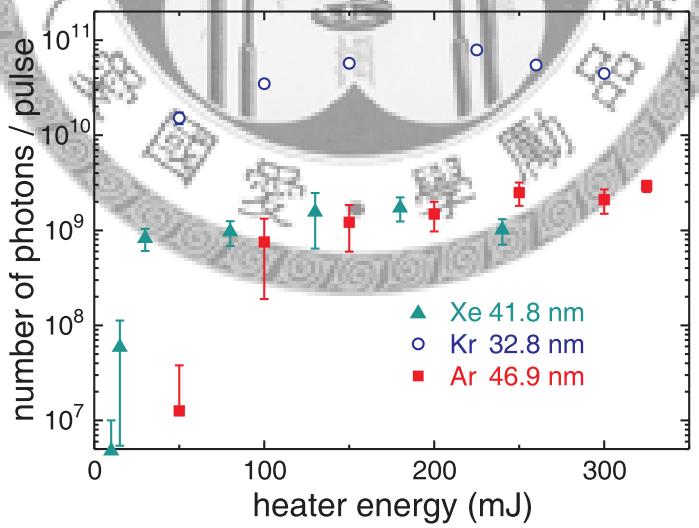

Figure 3.3: Number of photons of 41.8-nm Xe^{8+}, 32.8-nm Kr^{8+}, and 46.9-nm Ar^{8+} lasing lines with a pure-gas plasma waveguide as a function of heater energy. The other parameters are the same as in Tab. 3.3.

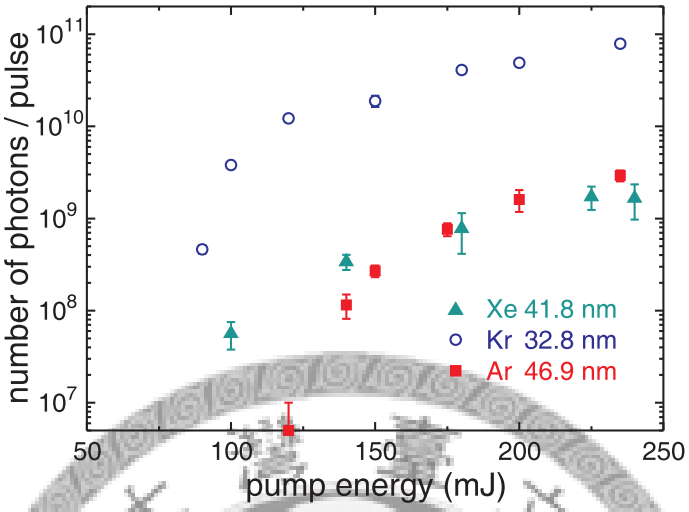

Figure 3.4: Number of photons of 41.8-nm Xe^{8+}, 32.8-nm Kr^{8+}, and 46.9-nm Ar^{8+} lasing lines with a pure-gas plasma waveguide as a function of pump energy. The other parameters are the same as in Tab. 3.3.

from the higher ion fraction and longer gain length with increasing pump energy. The reduced rate of increase in lasing output at high pump energies may be attributed to saturated lasing ion fraction (to unity) and saturated gain length (to the length of the plasma waveguide).

Figure 3.5 shows the number of photons for 41.8-nm Xe^{8+}, 32.8-nm Kr^{8+}, and 46.9-nm Ar^{8+} lasing lines with a pure-gas plasma waveguide as a function of atom density in the gas jet. The other parameters are the same as in Tab. 3.3. Interferometry measurements reveal that the on-axis ion density increases with increasing gas-jet atom density when the other parameters are fixed. The x-ray lasing intensity increases exponentially with increasing atom density at low density, which can be ascribed to the increase in gain coefficient with increasing on-axis lasing ion density and also with increasing on-axis lasing ion fraction due to better guiding. At higher atom densities, the increase in lasing photon number with increasing atom density becomes gradually saturated. This may indicate that the amplification reaches the saturation regime, in which the photon number becomes roughly linearly proportional to the lasing ion density instead of exponentially proportional. As observed from the Ar data, at even higher atom densities the lasing photon number decreases with increasing atom density, which may be explained by the increased collisional-deexcitation and collisional-mixing rate of the upper level with increasing on-axis plasma density and/or the lowered lasing

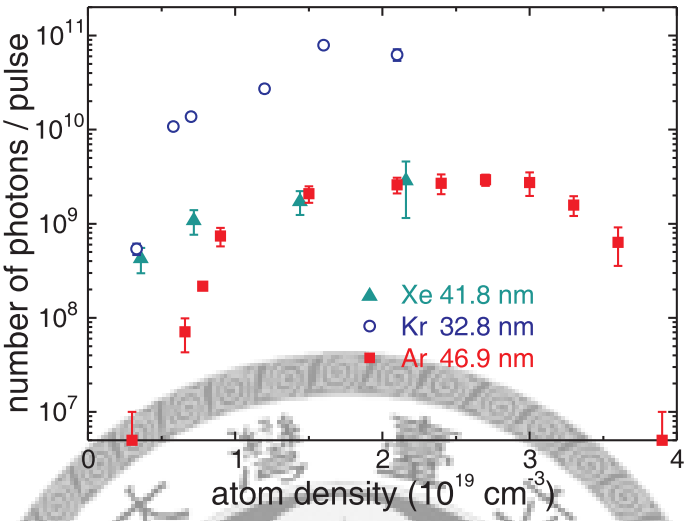

Figure 3.5: Number of photons of 41.8-nm Xe^{8+}, 32.8-nm Kr^{8+}, and 46.9-nm Ar^{8+} lasing lines with a pure-gas plasma waveguide as a function of atom density. The other parameters are the same as in Tab. 3.3.

ion fraction with the increase in channel diameter and thus the decrease in pump intensity. In contrast to an OFI x-ray laser without guiding, with a plasma waveguide the operating atom density can be raised to a level greatly exceeding the restriction set by ionization-induced refraction, making the lasing much stronger.

Figure 3.6 shows the number of photons for 41.8-nm Xe^{8+}, 32.8-nm Kr^{8+}, and 46.9-nm Ar^{8+} lasing lines with a pure-gas plasma waveguide as a function of pump polarization. The other parameters are the same as in Tab. 3.3. For 41.8-nm Xe^{8+} lasing, the highest photon number is achieved at circular polarization while no x-ray lasing occurs at linear polarization. The strong dependence on pump polarization ellipticity reveals that above-threshold ionization heating is the dominant heating mechanism. For 32.8-nm Kr^{8+} lasing, the x-ray lasing photon number is also higher for a circularly polarized pump than for a linearly polarized pump but the difference is much smaller. Strong lasing can also be obtained with a linearly polarized pump pulse. For 46.9-nm Ar^{8+} lasing, the lasing photon number shows roughly no dependence on pump polarization ellipticity. The results for Kr and Ar support the strong enhancement effect by the plasma waveguide, which enables lasing even for the much less effective linearly polarized pump pulse. A plasma waveguide can provide a long gain length which can lead to saturation even with the low gain coefficient from a linearly polarized pump pulse, thus reducing the

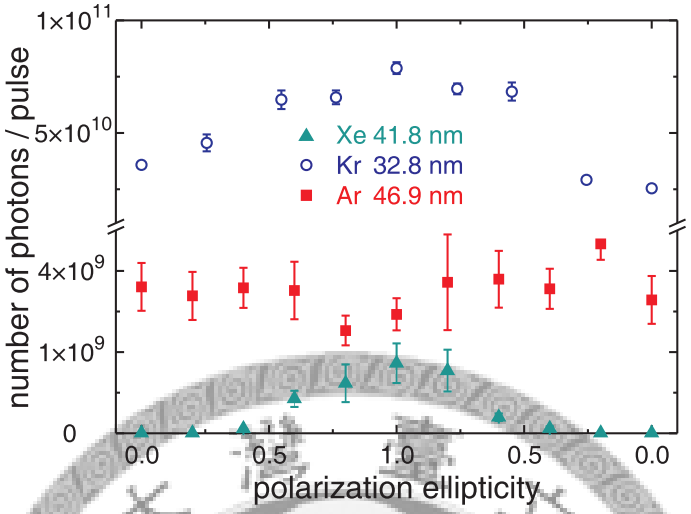

Figure 3.6: Number of photons of 41.8-nm Xe^{8+}, 32.8-nm Kr^{8+}, and 46.9-nm Ar^{8+} lasing lines with a pure-gas plasma waveguide as a function of pump polarization. The other parameters are the same as that in Tab. 3.3.

dependence on polarization ellipticity. Furthermore, a plasma waveguide can also reduce the difference in the gain coefficient via two effects. First, due to the high electron density, the collisional excitation to the upper level of x-ray lasing can be quite effective even though the fraction of electrons exceeding the collisional excitation threshold is lower for a linearly polarized pump pulse. This is consistent with the fact that in these three cases the atom density used for Ar is the highest. Second, with increasing pump laser intensity, other heating mechanisms such as stimulated Raman scattering may come into play so that the difference in electron temperature when using pump pulses of different polarization ellipticities is reduced. This is consistent with the fact that in these three cases higher pump intensity inside the plasma waveguide is used when changing from Xe to Kr to Ar.

X-ray laser using an optically preformed plasma waveguide of Kr/H_2 mixture is also investigated. Figure 3.7(a) and (b) show the x-ray spectrum and angular distribution, respectively, for a 32.8-nm Ni-like Kr laser by using a Kr/H_2 mixed-gas plasma waveguide. The total backing pressure of the gas jet is 630 psi, and the $Kr:H_2$ partial-pressure ratio is 1 : 4. Assuming that the relation between backing pressure and atom density measured for pure krypton can be applied to the mixed gas, the Kr atom density is estimated to be 5.8×10^{18} cm^{-3}. The ignitor energy is 45 mJ, the heater energy is 50 mJ, the ignitor-heater separation is 200 ps, and the heater-pump delays

is 2.5 ns. The output is only 2×10^9 photon/pulse, and the x-ray beam divergence is decreased to 2.7 mrad in FWHM. Although a better guiding efficiency is achieved, the lasing photon number is not as large as that with a pure gas plasma waveguide, which may be ascribed to the lower krypton density imposed by the maximum applicable gas-jet backing pressure and also the cooling of plasma electron temperature by the low-temperature electrons released from hydrogen [89].

Figure 3.8 shows the number of photons of a 32.8-nm Kr^{8+} lasing line with a Kr/H_2 mixed-gas plasma waveguide (triangle) and with a pure Kr plasma waveguide (square) as a function of pump polarization ellipticity. Due to the lower krypton density and the cooling effect of cold electrons, the output of Ni-like Kr lasing exhibits much stronger dependence on pump polarization ellipticity. Figure 3.9 shows the number of photons of a 32.8-nm Kr^{8+} lasing line with a Kr/H_2 mixed-gas plasma waveguide (triangle) and with a pure Kr plasma waveguide (square) as a function of heater energy. The optimal heater energy can also be ascribed to the same trade-off mechanism described above. Note that the optimal heater energy is much lower in the case of a Kr/H_2 mixed-gas waveguide. This discrepancy may result from the lighter hydrogen ions, leading to faster plasma expansion and thus a lower on-axis ion density.

3.2 Multiple Lasing Lines for the Same Ion Species

3.2.1 Ni-like Kr lasing

Using an optically preformed plasma waveguide yields not only dramatic enhancement of a soft x-ray laser but also subsidiary lasing lines. In the case of a Kr^{8+} plasma waveguide, besides the primary lasing line at 32.8 nm, another lasing line at 33.5 nm is also observed, as shown in Fig. 3.10(b). The output of the 33.5-nm lasing line roughly maintained at about two orders of magnitude smaller than that of the 32.8 nm lasing line with varying atom density, pump polarization, pump energy, and heater energy, as shown in Figure 3.11. This seems to indicate that the 33.5-nm lasing line comes from a transition from the same upper level to another satellite lower level close to that of the primary lower level. It may be attributed to the $3d^9\ 4d\ ^1S_0$ – $3d^9\ 4p\ ^3D_1$ transition, as illustrated in Fig. 3.12.

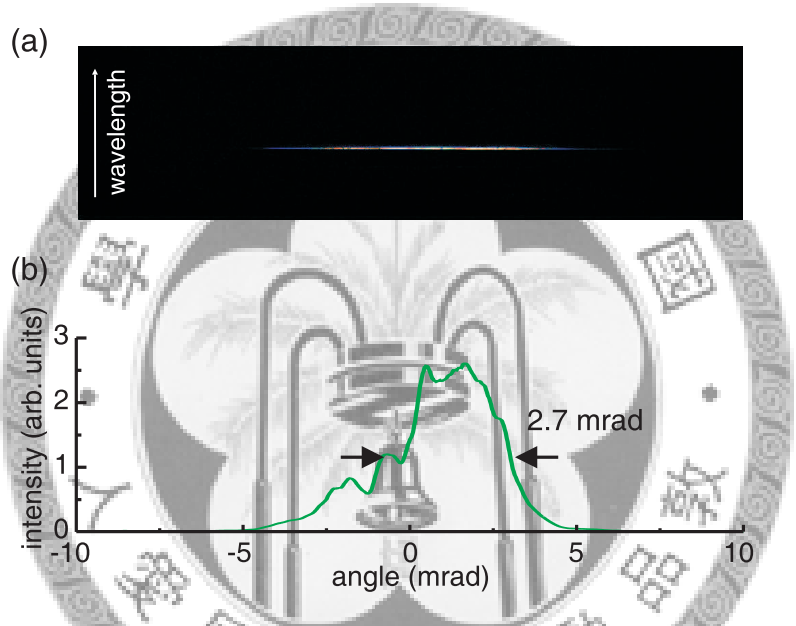

Figure 3.7: (a) X-ray emission spectrum and (b) angular distribution in the propagation direction of the pump pulse for a 235-mJ circularly-polarized pump pulse guided in a Kr/H_2 mixed-gas waveguide. The total backing pressure of the gas jet is 630 psi and the $Kr{:}H_2$ partial-pressure ratio is 1 : 4. The ignitor energy is 45 mJ, the heater energy is 50 mJ, the ignitor-heater separation is 200 ps, and the heater-pump delays is 2.5 ns.

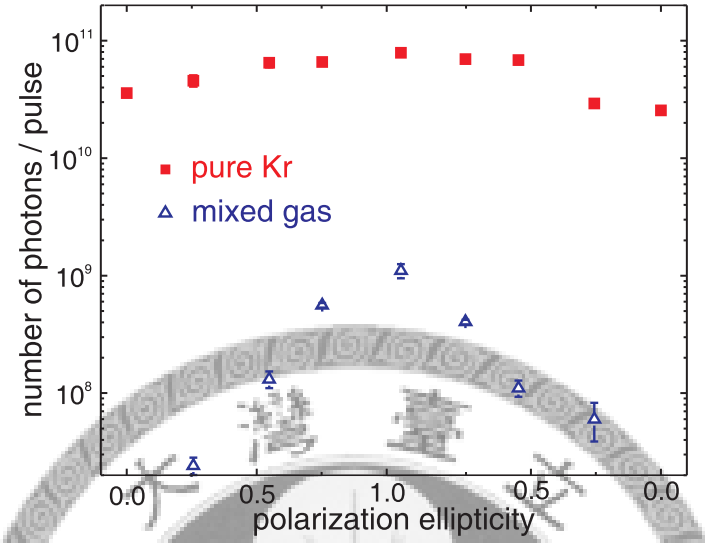

Figure 3.8: Number of photons of a 32.8-nm Kr^{8+} lasing line with a pure Kr plasma waveguide (square) and a Kr/H_2 mixed-gas plasma waveguide (triangle) as a function of pump polarization ellipticity. The other parameters are the same as that for Fig. 3.7.

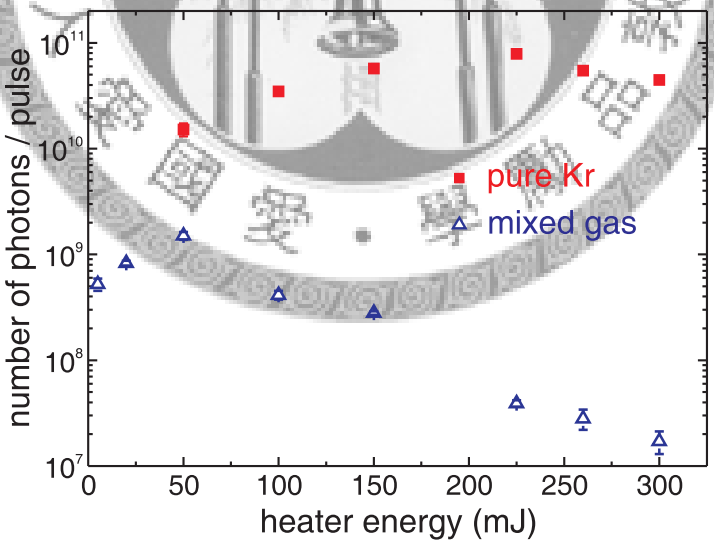

Figure 3.9: Number of photons of a 32.8-nm Kr^{8+} lasing line with a pure Kr plasma waveguide (square) and with a Kr/H_2 mixed-gas plasma waveguide (triangle) as a function of heater energy. The other parameters are the same as in Fig. 3.7.

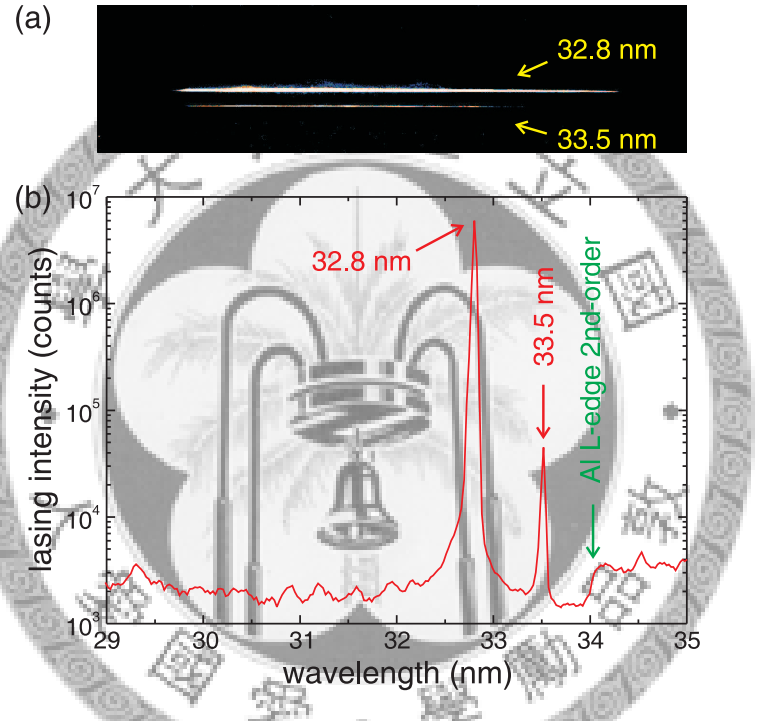

Figure 3.10: (a) CCD raw image and (b) x-ray emission spectrum in the propagation direction of the pump pulse for a 235-mJ circularly polarized pump pulse guided in a pure krypton waveguide with an atom density of 1.6×10^{19} cm^{-3}. The ignitor energy is 45 mJ, the heater energy is 225 mJ, the ignitor-heater separation is 200 ps, and the heater-pump delay is 2.5 ns.

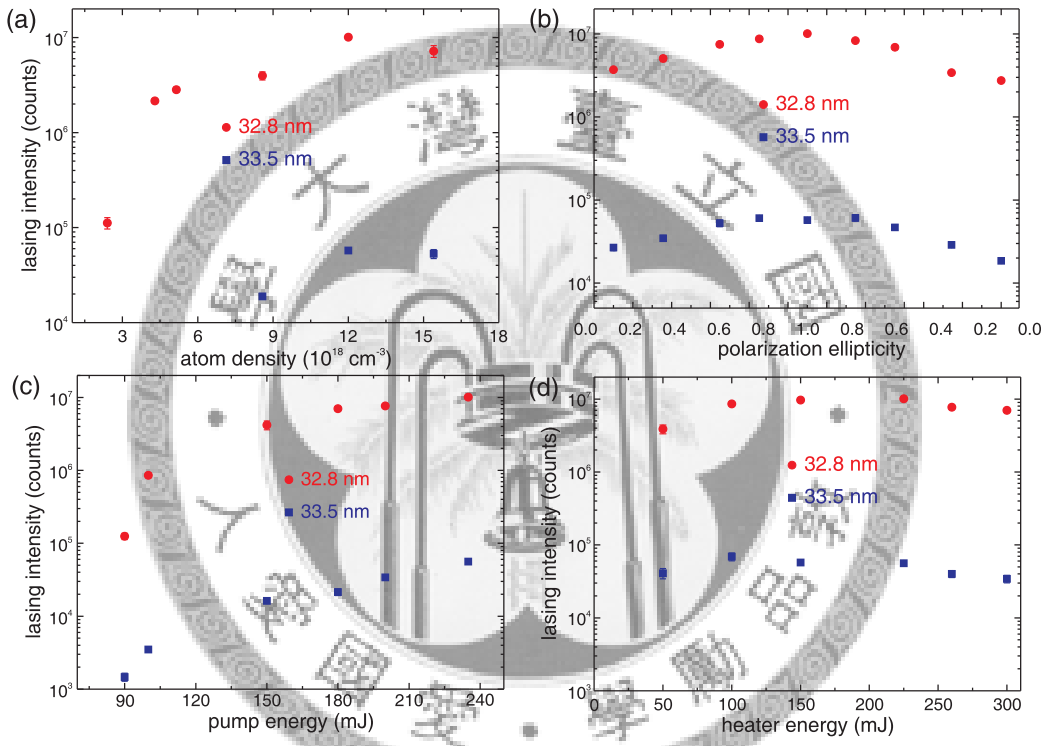

Figure 3.11: Number of photons of 32.8-nm and 33.5-nm Kr^{8+} lasing lines with a pure-gas plasma waveguide as a function of (a) atom density, (b) pump polarization, (c) pump energy, and (d) heater energy. The other parameters are the same as in Tab. 3.3.

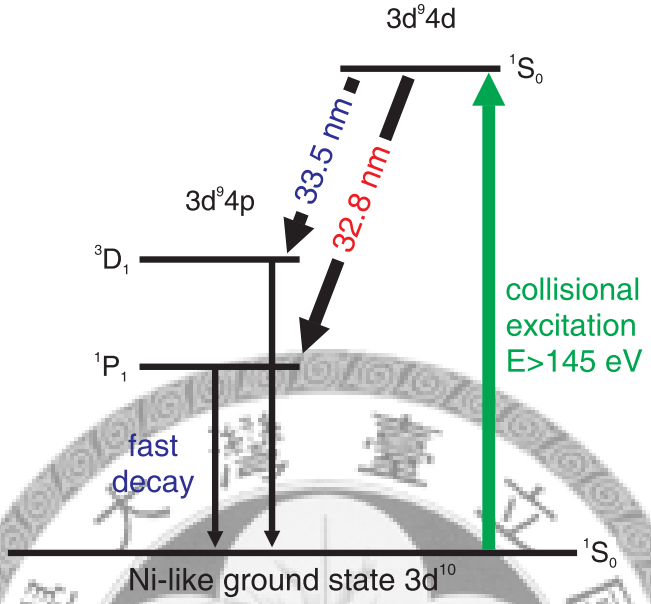

Figure 3.12: Simplified energy-level diagrams of the Ni-like Kr ion.

3.2.2 Ne-like Ar lasing

In the case of an Ar^{8+} plasma waveguide, besides the strong lasing line at 46.9 nm, two additional lasing lines at 45.1 nm and 46.5 nm are observed, as shown in Fig. 3.14(b). Observation of the 45.1-nm lasing line from a Ne-like argon plasma has been reported in the experiments with an Ar gas puff target irradiated by a high-energy laser beam focused to a line [90, 91, 92, 93]. The 45.1-nm line was recognized as the $2p^5\ 3d\ ^1P_1 - 2p^5\ 3p\ ^1P_1$ transition in Ne-like Ar driven by the self-photopumping mechanism [90, 91, 92, 93]. Photopumping is one of the original mechanisms for demonstrating x-ray lasing, which uses thigh-energy photons to pump the laser upper level. Of several photopumping methods, resonant photopumping is more efficient because it uses a strong pump line that is resonant with a line in the lasing material that can be photopumped and thereby create a population inversion [94, 20]. Nilsen *et al.* showed that the amplification observed in the $2p^5\ 3d\ ^1P_1 - 2p^5\ 3p\ ^1P_1$ line of Ne-like Ar at 45.1 nm in a laser-created plasma was assisted by photopumping due to reabsorption of the $2p^5\ 3d\ ^1P_1 - 2p^6\ ^1S_0$ resonance line [90, 91, 92, 93]. Unlike other proposed resonantly photopumped x-ray laser schemes that require a strong pump line from a separate plasma that is resonant with a line in the laser medium, this scheme is self-pumped and therefore has a perfect resonance.

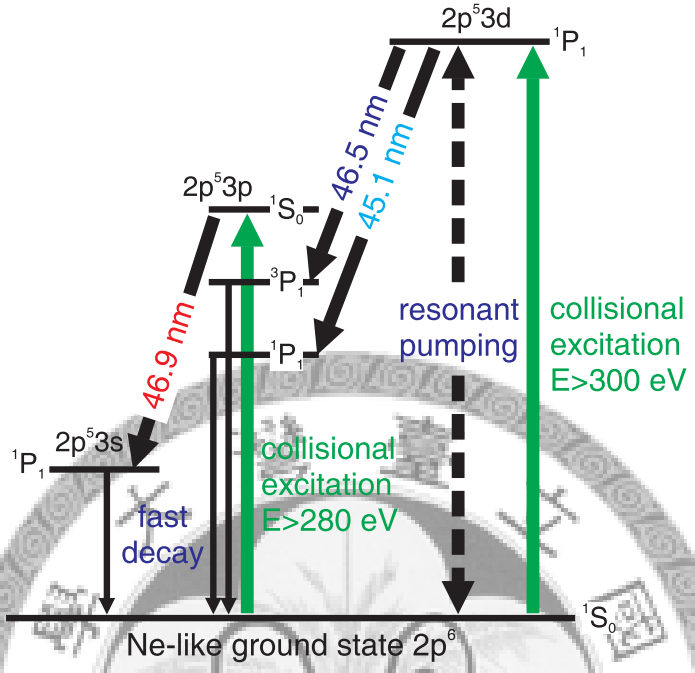

Figure 3.13: Simplified energy-level diagrams of the Ne-like Ar ion.

Figure 3.13 illustrates the energy-level diagrams for Ne-like argon. Lasing at 45.1 nm and 46.5 nm can be produced by collisional excitation from the ground level to the $2p^5\ 3d\ ^1P_1$ upper level. Radiative decay of the upper level to the $2p^6\ ^1S_0$ ground state is not forbidden, however it is counteracted by radiation trapping as a result of high ion density (optically thick), which is referred to as self-photopumping. The $2p^5\ 3p\ ^1P_1$ and $2p^5\ 3p\ ^3P_1$ lower levels are quickly depopulated through collisional mixing with the other nearby $3s$ and $3d$ states and also by radiative decay. The $2p^5\ 3d\ ^1P_1$ state also decays strongly to the $2p^5\ 3p\ ^1S_0$ state and enhances the gain of the collisionally excited $2p^5\ 3p\ ^1S_0$ – $2p^5\ 3s\ ^1P_1$ transition at 46.9 nm. For convenience, the $1s^2\ 2s^2$ electrons, which are common to all the levels, are omitted, and LS coupling notation is used. The strong lasing at 45.1 nm with an intensity comparable to that of the 46.9 nm lasing and the first observation of 46.5-nm lasing, which has even less gain than the 45.1-nm line, verify the strong enhancement capability of the optically preformed plasma waveguide.

Figure 3.15 shows the number of photons for the three Ar^{8+} lasing lines with a pure-gas plasma waveguide as a function of pump energy. The other parameters are the same as in Tab. 3.3. The dependencies on pump energy for the three lasing lines are similar because they are from the same lasing

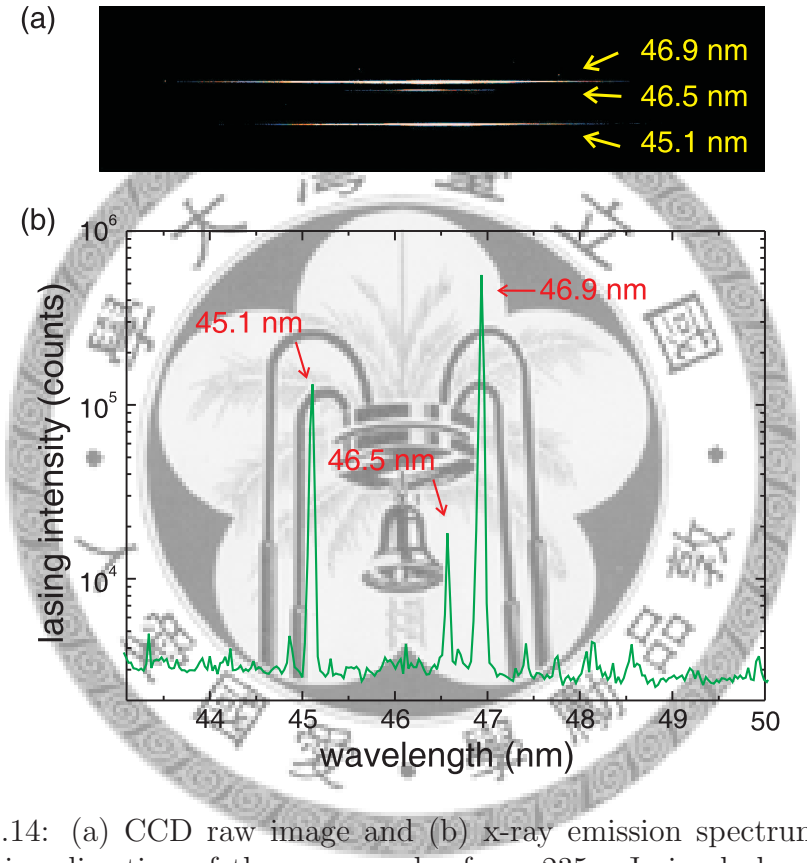

Figure 3.14: (a) CCD raw image and (b) x-ray emission spectrum in the propagation direction of the pump pulse for a 235-mJ circularly polarized pump pulse guided in a pure argon waveguide with an atom density of 2.7×10^{19} cm^{-3}. The ignitor energy is 45 mJ, the heater energy is 325 mJ, the ignitor-heater separation is 200 ps, and the heater-pump delay is 1.5 ns.

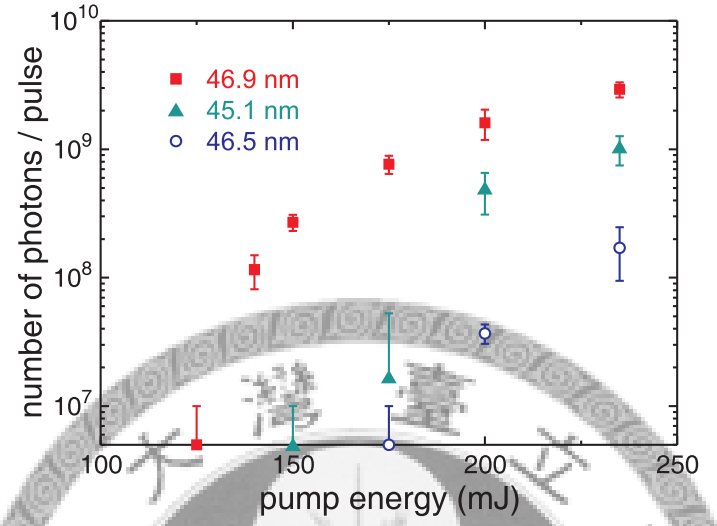

Figure 3.15: Number of photons for the three Ar^{8+} lasing lines with a pure-gas plasma waveguide as a function of pump energy. The other parameters are the same as in Tab. 3.3.

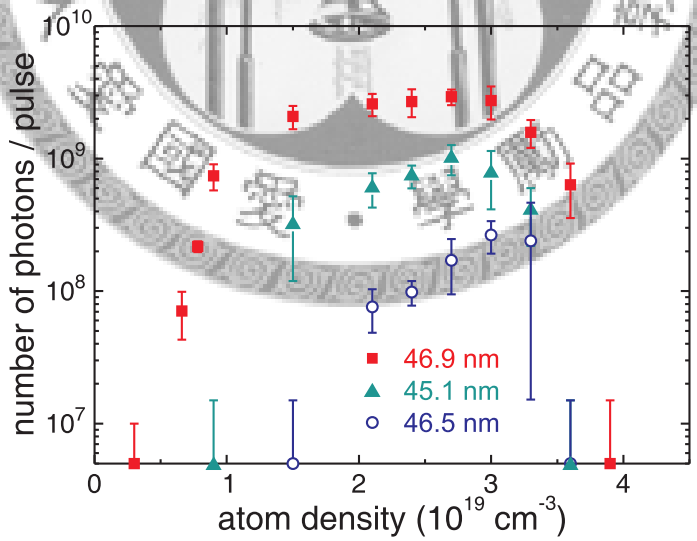

Figure 3.16: Number of photons for the three Ar^{8+} lasing lines with a pure-gas plasma waveguide as a function of atom density in the gas jet. The other parameters are the same as in Tab. 3.3.

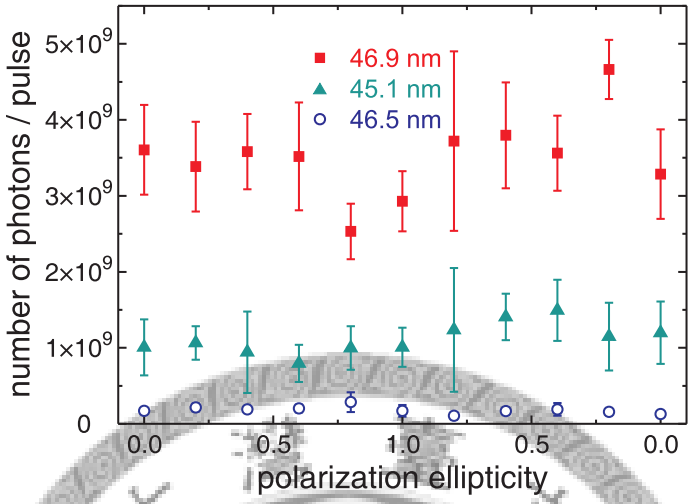

Figure 3.17: Number of photons for the three Ar^{8+} lasing lines with a pure-gas plasma waveguide as a function of pump polarization ellipticity. The other parameters are the same as in Tab. 3.3.

ions, while the thresholds for lasing and the magnitudes of their output at the same pump energy differ because of their different gain coefficients.

Figure 3.16 shows the number of photons for the three Ar^{8+} lasing lines with a pure-gas plasma waveguide as a function of atom density. The other parameters are the same as in Tab. 3.3. With increasing atom density, the photon numbers of all lasing lines all increase exponentially at low atom density, gradually saturate at higher density, and decrease at even higher density. Note that at an atom density exceeding 1.5×10^{19} cm^{-3}, the 45.1-nm land the 46.5-nm lasing keep increasing exponentially, while the 46.9-nm lasing becomes strongly saturated. This may indicate a decreased lower-level population with increasing plasma density via collisional mixing with nearby $3s$ and $3d$ states. At an atom density above 3×10^{19} cm^{-3}, the outputs of all three lines start to decrease with increasing atom density. This may be explained by two effects. First, the increasing atom density provides higher on-axis plasma density, which enhances inverse bremsstrahlung heating and thus increases the expansion velocity of the plasma waveguide. The increase in channel diameter will guide a larger beam diameter, resulting in a reduced intensity and thus a lowered lasing ion fraction. On the other hand, the rate of collisional deexcitation and collisional mixing of the upper level increases with on-axis plasma density, leading to a lower population inversion and thus a lower gain.

Figure 3.17 shows the number of photons for the three Ar^{8+} lasing lines with a pure-gas plasma waveguide as a function of pump polarization ellipticity. The other parameters are the same as in Tab. 3.3. All show roughly no dependence on pump polarization ellipticity, which can be explained by the reasons given in the previous section.

3.3 Multi-Species Parallel X-Ray Lasing in a Mixed-Gas Plasma Waveguide

With a Kr/Ar mixed-gas plasma waveguide, we achieved simultaneous multi-species x-ray lasing. Figure 3.18 shows the x-ray lasing spectrum for a plasma waveguide of mixed Kr and Ar with a partial-pressure ratio of 1 : 1 and a total backing pressure of 400 psi. The pump pulse energy is 240 mJ, the ignitor energy is 45 mJ, the heater energy is 220 mJ, the ignitor-heater separation is 200 ps, and the heater-pump delay is 1.5 ns. Assuming that the relations between backing pressure and atom density measured for pure krypton and pure argon gas jets can be applied to the mixed gas, the Kr and Ar atom densities are estimated to be 9.1×10^{18} cm^{-3} and 1.2×10^{19} cm^{-3}, respectively. Although the optimal conditions for maximized lasing output are different for Kr and Ar plasma waveguides, simultaneous lasing of the two ion species can be obtained at trade-off conditions.

The dependencies of x-ray lasing photon number on backing pressure (atom density), pump energy, and pump polarization for 32.8-nm Kr^{8+} lasing and 46.9-nm Ar^{8+} lasing are shown in Fig. 3.19 - 3.21, respectively. The other parameters are the same as in Fig. 3.18. The behavior of the two lasing lines in the mixed gas is similar to that in the case of pure gas, and it can be explained by the same reason.

Figure 3.22 shows the number of photons for 32.8-nm Kr^{8+} and 46.9-nm Ar^{8+} lasing lines with a mixed-gas plasma waveguide as a function of heater energy. The other parameters are the same as in Fig. 3.18. For a heater energy exceeding 100 mJ, the photon number of 32.8-nm Kr^{8+} lasing decreases with increasing heater energy, whereas that of 46.9-nm Ar^{8+} lasing increases with increasing heater energy. At a short delay of 1.5 ns the guiding efficiency of the pump pulse, and thus the pump intensity, increases with increasing heater energy. Because the ionization intensity threshold of Ar^{8+} is almost twice of that of Kr^{8+}, while the 46.9-nm Ar^{8+} lasing intensity increases as a result of increased Kr^{8+} ion fraction, the 32.8-nm Kr^{8+} lasing intensity

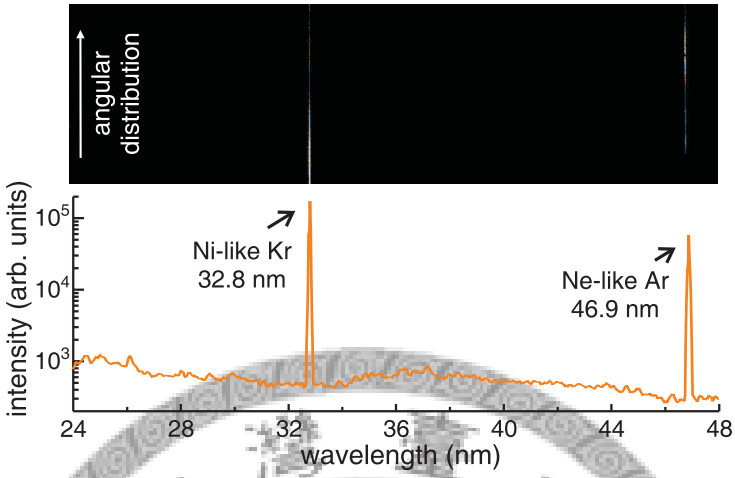

Figure 3.18: X-ray emission spectrum in the propagation direction of the pump pulse for a 240-mJ circularly polarized pump pulse guided in a Kr/Ar mixed-gas plasma waveguide. The total backing pressure of the gas jet is 400 psi and the Kr:Ar partial-pressure ratio is 1 : 1. The ignitor energy is 45 mJ, the heater energy is 220 mJ, the ignitor-heater separation is 200 ps, and the heater-pump delay is 1.5 ns.

decreases as a result of decreased Kr^{8+} ion fraction due to over-ionization to the next ionization stage. Although multi-line coherent soft x-ray source can be produced by other methods, such as high-harmonic generation or soft x-ray lasers by other pumping schemes, few allow control of the relative intensities of different lasing lines. In contrast, the dependence on heater energy provides an easy way to tune the ratio of the intensities of the two lasing lines, which is useful in the application of such a two-color soft-x-ray laser.

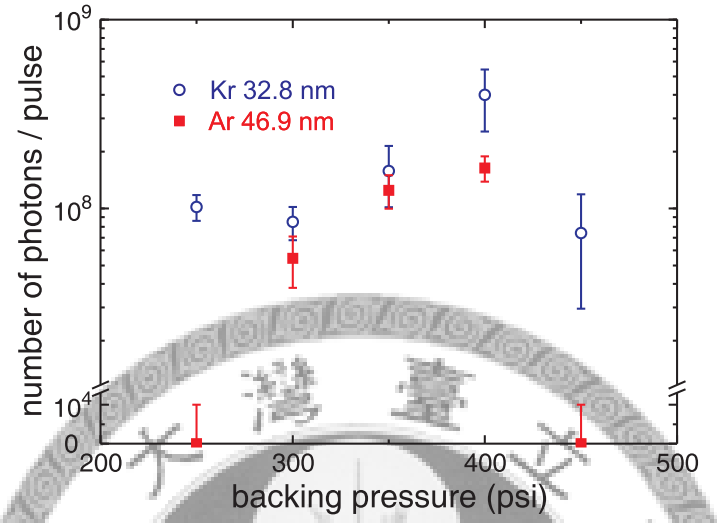

Figure 3.19: Number of photons for 32.8-nm Kr^{8+} and 46.9-nm Ar^{8+} lasing lines respectively with a Kr/Ar mixed-gas plasma waveguide as a function of backing pressure. The other parameters are the same as in Fig. 3.18.

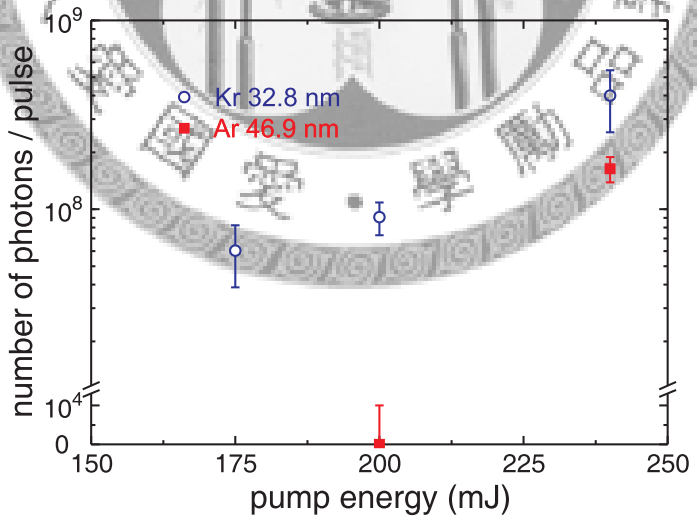

Figure 3.20: Number of photons for 32.8-nm Kr^{8+} and 46.9-nm Ar^{8+} lasing lines respectively with a Kr/Ar mixed-gas plasma waveguide as a function of pump energy. The other parameters are the same as in Fig. 3.18.

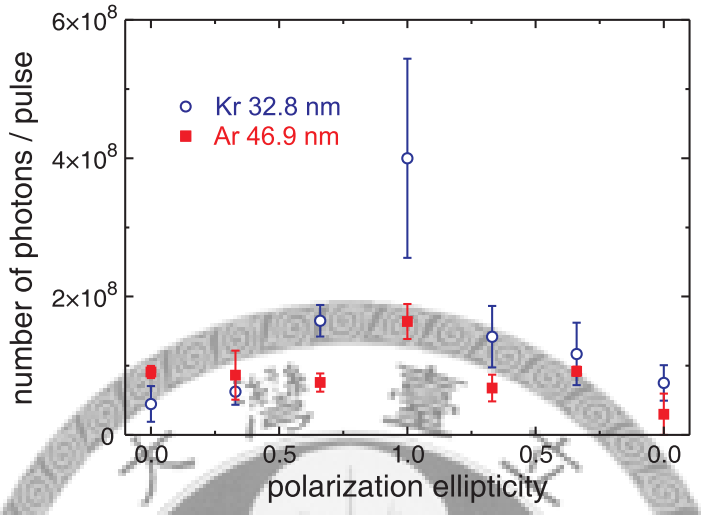

Figure 3.21: Number of photons for 32.8-nm Kr^{8+} and 46.9-nm Ar^{8+} lasing lines respectively with a Kr/Ar mixed-gas plasma waveguide as a function of pump polarization ellipticity. The other parameters are the same as in Fig. 3.18.

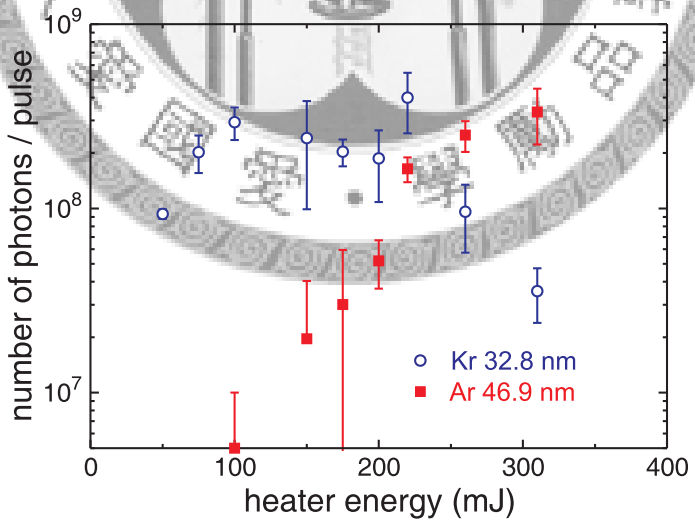

Figure 3.22: Number of photons for 32.8-nm Kr^{8+} and 46.9-nm Ar^{8+} lasing lines respectively with a Kr/Ar mixed-gas plasma waveguide as a function of heater energy. The other parameters are the same as in Fig. 3.18.

Chapter 3. Multi-line Waveguide-Based Optical-Field-Ionization Soft X-Ray Lasers

Chapter 4

Seeding of an Optical-Field-Ionization Soft X-Ray Laser in a Plasma Waveguide by High Harmonic Generation

4.1 Introduction

Until now, the soft x-ray lasers discussed above are all based on amplified spontaneous emission (ASE). An ASE x-ray laser exhibits a large output but has limited waveform quality due to self-seeded amplification from spontaneous emission noise. In addition, ASE lasers are unpolarized [95], and have a relatively long pulse duration (few to tens of picoseconds) associated with the gain duration [96, 43, 97, 26]. Many studies have been devoted to improving the optical quality of soft x-ray lasers. These include the demonstration of double-pass amplification [98] to enhance the spatial coherence or an multistage geometry combined with a polarization-dependent x-ray mirror to demonstrate amplification of a polarized soft x-ray laser beam [95]. However, these improvements focus on only one or two characteristics of x-ray lasers and the enhancement is limited. In contrast, high harmonic generation (HHG) shows a high degree of spatial coherence [99] and has a much shorter pulse duration (less than 10 femtoseconds to attoseconds) due to its broad bandwidth. However, the absolute photon number is limited. Due to the complementary characteristics, it is natural to combine HHG and an ASE soft-x-ray laser by using HHG as a seed and an ASE soft x-ray laser as an amplifier to generate intense soft x-ray pulses with small divergence, short pulse width, enhanced spatial coherence, and controlled polarization.

Moreover, seeded x-ray lasers do not suffer from timing jitter relative to the pump laser, which is important for pump-probe applications. Amplification of an HHG seed was first demonstrated by Ditmire *et al.* in a gallium target, but the amplification factor was low due to strong refraction caused by dense plasma [100]. Recently HHG seeding with high gain was achieved in optical-field-ionization (OFI) x ray-lasers in a krypton gas cell [96, 82, 101]. Later, saturated amplification of HHG seed pulses was achieved in collisonal-ionization x-ray lasers by heating solid targets [102, 103, 104]. In view of the great versatility and high efficiency of OFI soft x-ray lasers based on optically preformed plasma waveguides in gas jets, it is highly desirable to see how HHG seeding will enhance the performance of such lasers. Nevertheless, HHG seeding of a soft x-ray laser is a complex problem, since the two x-ray sources have many distinct characteristics. Several simulations of the behavior of a seeded soft x-ray laser have been performed to this new field [105, 106]. Here, on the experimental side, we demonstrate HHG seeding of a soft x-ray laser in a plasma waveguide, and the detailed optimization and characterization of the seeded soft x-ray laser are reported in the following sections.

4.2 Characteristics of the High Harmonic Generation

HHG is usually produced by nonlinear interaction between an intense laser and gas atoms. The basic process of HHG can be described using the semiclassical three-step model proposed by Corkum and Kulander *et al.* [107, 108]. Figure 4.1 (from [8]) illustrates the concepts associated with each step. First, the outer-shell electron of the atom is ionized by the intense laser field via tunnelling ionization near the laser peak and becomes free with null initial velocity. The freed electron is accelerated by the laser field and moves on a classical trajectory in the laser field. If the field is linearly polarized, then the electron can be accelerated back toward its parent ion and has a certain probability of recombining with it and emitting a high-energy photon. The energy of the emitted photon is determined by the sum of the ionization potential and the instantaneous kinetic energy of the electron at the moment of recombination. The kinetic energy depends on the phase of the electric field at the moment of ionization. According to this semiclassical model, the maximum photon energy (cutoff energy) occurs at a phase of 17° after the peak of the laser cycle (at a phase of 0°) and is given by [107, 109]

$$\hbar\omega_{\max} = I_p + 3.17U_p, \tag{4.1}$$

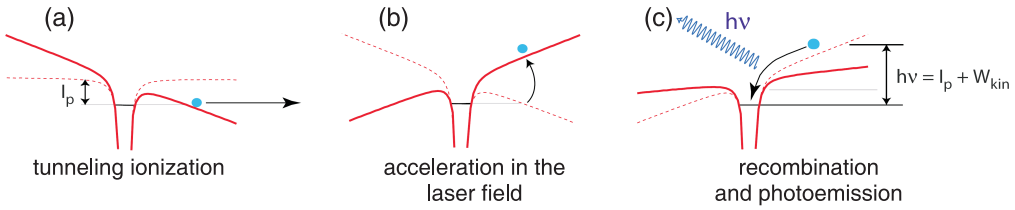

Figure 4.1: Illustration of three-step model: (a) tunnelling ionization of the electron, (b) electron in the laser field, and (c) recombination and emission of a high-energy photon. The energy of the emitted photon is the sum of the ionization potential (I_p) and the instantaneous kinetic energy of the electron at the moment of recombination (W_{kin}) (from Ref[8]).

where I_p is the ionization potential of the atom and U_p is the ponderomotive potential

$$U_p[\mathrm{eV}] = \frac{e^2E^2}{4m_e\omega^2} = 9.33 \times 10^{-14} I[\mathrm{W/cm^2}]\lambda^2[\mu\mathrm{m}^2], \tag{4.2}$$

where e, E, m_e, ω, I, and λ are the electron charge, strength of the electric field, electron mass, laser frequency, laser intensity and laser wavelength, respectively. Usually, the cutoff energy of HHG can extend to the soft x-ray region. For example, for an 800-nm laser pulse with an intensity of 2×10^{14} W/cm^2, the maximum kinetic energy is 38 eV, and the cutoff photon energy is 54 eV for an Ar atom, corresponding to 23-nm x rays. Since this process occurs every half cycle of the electric field, the emitted radiation is produced with the same period; for example, 1.3 fs for an 800-nm laser pulse. These consecutive bursts add coherently and thus result in a discrete spectrum consisting of the odd harmonics of the laser frequency [8].

From the above semiclassical theory, HHG is considered as a coherent process driven by a coherent laser pulse; thus, it should retain most properties of the driving laser. HHG has been proven to have low divergence [110, 111], high spatial and temporal coherence [99, 112, 113], and linear polarization. Moreover, it occurs only during the duration of the driven laser and thus has an ultrashort pulse duration, from sub-10-femtoseconds to attoseconds [9]. The harmonic source meets almost every requirement for a soft x-ray coherent source, but the absolute output is limited by the ionization threshold, resulting in pulse energies typically in the nJ range [10]. In contrast, soft x-ray lasers possesses much higher energies but lacks good properties as a coherent source. Therefore, it is expected that an ultrashort, highly coher-

ent, high-intensity soft x-ray coherent source can be obtained by combining HHG (as a seed) and a waveguide-based x-ray laser (as an amplifier).

4.3 System Design and Configuration

The experimental setup is shown in Fig. 4.2. An 11-mm-diameter 3.8-mJ pulse is used as the pump pulse to produce soft-x-ray seed pulse via HHG. It is focused with an off-axis parabolic mirror (OAP) of 30-cm focal length onto an Ar clustered gas jet. The Ar gas jet is produced by a 1-mm-diameter conical nozzle and a pulsed valve. The atom density is set at 7.1×10^{18} cm^{-3}. The focal spot size of the pulse is 30 μm in full width at half maximum (FWHM) with 87% energy enclosed in a Gaussian-fit profile. The focus is placed at 1.3 mm after the entrance of the Ar gas jet. The beam diameter, laser energy, atom density, and focal position are chosen for maximizing the 25th harmonic. Matching of the central wavelength of the HHG seed to that of the Ni-like Kr 32.8-nm x-ray laser amplifier is achieved by setting the pump pulse of HHG to a duration of 360 fs and a positive chirp [114]. The produced HHG pulse is imaged onto the entrance of the soft-x-ray amplifier by a soft-x-ray multilayer concave mirror of 30-cm focal length and propagates collinearly with the amplifier pump pulse. A reflecting mirror with a hole at its center is used to combine the HHG pulse and the amplifier pump pulse. The orientation of the linearly polarized HHG is controlled by rotating the polarization of its pump pulse with a half-wave plate.

The soft-x-ray amplifier is driven by three pulses. A 235-mJ, 38-fs, circularly polarized pulse is used as the pump pulse for preparation of the lasing ionization stage through optical-field ionization and heating of the plasma electrons to achieve collisional excitation. The other two pulses, referred to as the ignitor and the heater, are used for fabricating a plasma waveguide by using the axicon-ignitor-heater scheme [51, 53]. For this experiment, the ignitor is 45 mJ in energy, 38 fs in duration, and *s*-polarized (vertically polarized), and the heater is 270 mJ in energy, 160 ps in duration, and *p*-polarized (horizontally polarized). After combined by a thin-film polarizer, these two pulses propagate collinearly and are then focused by an axicon of 30° base angle on the Kr clustered gas jet. The line focus overlaps with the propagation path of the amplifier pump pulse in the gas jet. A hole of 5-mm diameter at the center of the axicon allows passage of the amplifier pump pulse and the HHG seed. To increase the efficiency of waveguide fabrication, a convex lens of 40-cm focal length with a hole of 2-cm diameter at the center

is positioned in front of the axicon to concentrate the laser energy in a length (∼1-cm length) matched to the length of the gas jet. The clustered gas jet used for the soft-x-ray amplifier is produced from a slit nozzle. The gas jet profile has a flat-top region of 8-mm length and a boundary of 500-μm length at both edges along the long axis. The atom density is 1.6×10^{19} cm^{-3}. The ignitor-heater separation and heater-pump separation are 200 ps and 2.5 ns, respectively. Under this condition, optimal guiding of the amplifier pump pulse in the plasma waveguide is achieved and the photon number of the ASE soft-x-ray pulse is at maximum. The details about the waveguide-based soft-x-ray amplifier were described in Chapter 2. Figure 4.3(a) shows more details about how the HHG seed, amplifier pump pulse, and ignitor/heater pulses are directed to the gas jet. Maximum amplification of the HHG seed is obtained when the delay between the HHG seed and the amplifier pump pulse is set at 2.0 ps. The relative time delays of the four pulses are shown in Fig. 4.3(b). A flat-field grazing-incidence x-ray spectrometer, consisting of a 1200-line/mm aperiodically ruled grating and a back-illuminated 16-bit x-ray charge-coupled device (CCD) camera, is used to measure the spectrum and horizontal angular profile of the output x-ray pulses, after the latter are reflected by a soft-x-ray multilayer mirror. Two 0.25-μm-thick aluminum filters are used to block the transmitted pump pulse and attenuate x-ray emission. From the known grating reflectivity, filter transmittance, x-ray mirror reflectance, and CCD response, the absolute number of soft-x-ray photons is determined. Mach-Zehnder interferometry with a 38-fs probe pulse is used to measure the plasma density distribution. A relayed imaging system, consisting of a movable wedge, a pair of lens, an objective lens, and a 14-bit CCD camera, is used to measure the beam profile of the pump pulse at the exit of the gas jet. An online imaging system, consisting of an objective lens, a movable aluminum mirror, and a 14-bit CCD camera, is used to do the spatial overlap between the pump beam and waveguide-forming pulses in air and vacuum. A photo of the experimental setup is shown in Fig. 4.4.

4.4 Optimization of the Seeded Soft X-Ray Laser

4.4.1 Spectral Overlap

In a seeding experiment, the HHG seed should be optimized for an output as high as possible to overcome the amplified spontaneous emission in the amplifier. This requires not only the strong emission from each single atom but also that all of the atoms in the gas emit in phase. The phase mismatch

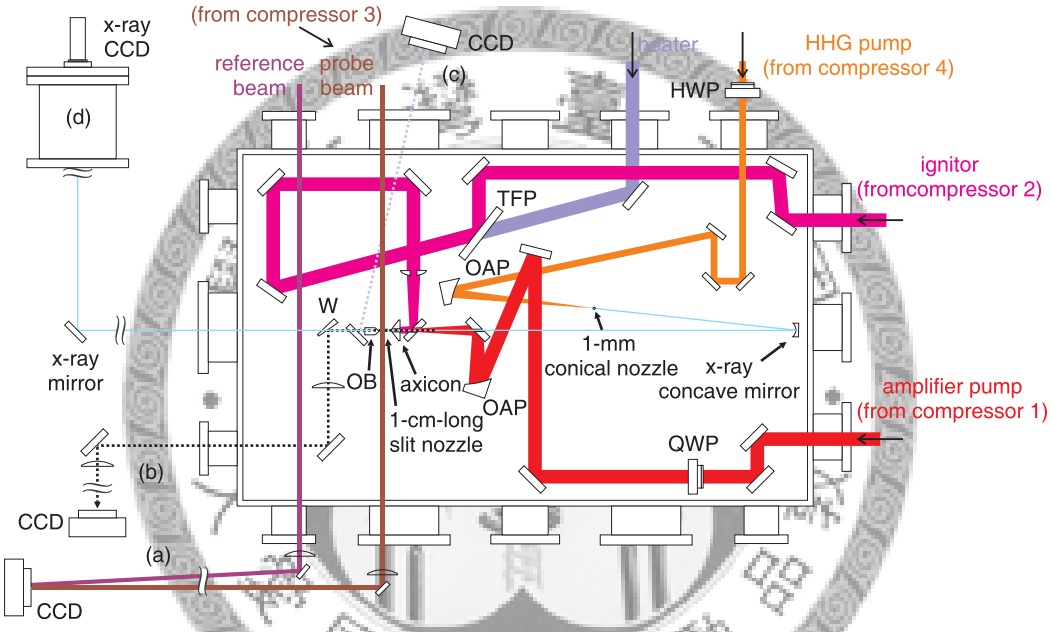

Figure 4.2: Experimental layout of the seeded waveguide-based soft-x-ray laser. OAP: off-axis parabolic mirror, QWP: quarter-wave plate, HWP: half-wave plate, TFP: thin-film polarizer, W: wedge, OB: objective, CCD: charge-coupled device. Four diagnostic tools were used: (a) interferogram, (b) relayed imaging system, (c) on-line imaging system, and (d) flat-field spectrometer.

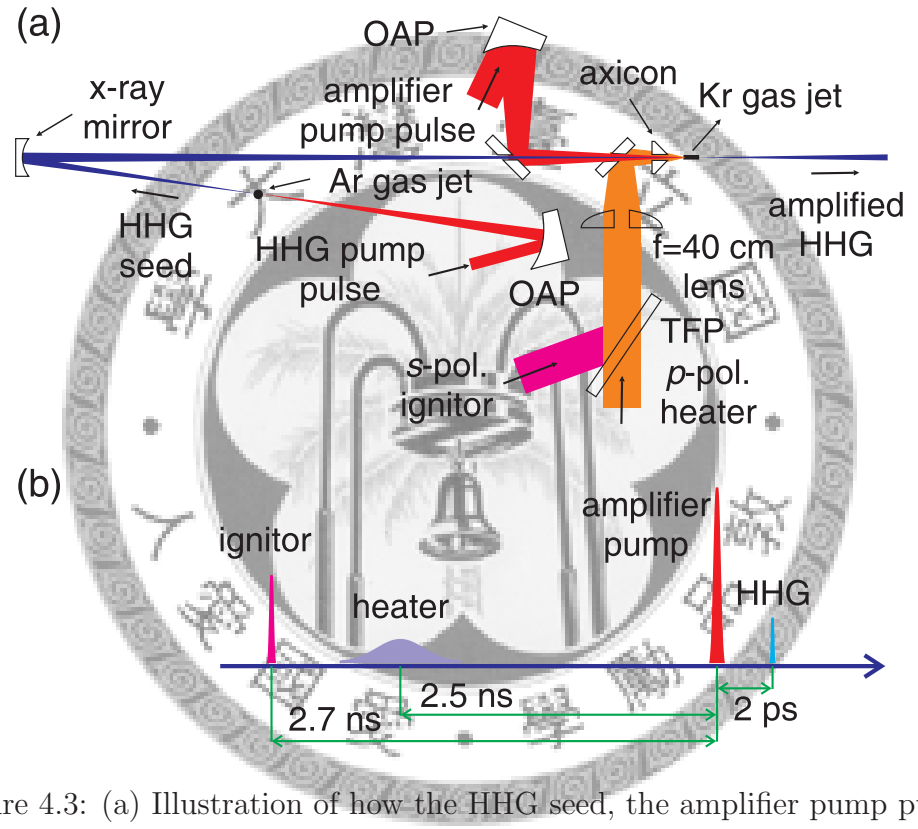

Figure 4.3: (a) Illustration of how the HHG seed, the amplifier pump pulse, and the ignitor/heater pulses are directed to the gas jet. (b) The relative time delays of the HHG seed, the amplifier pump pulse, the ignitor pulse, and the heater pulse.

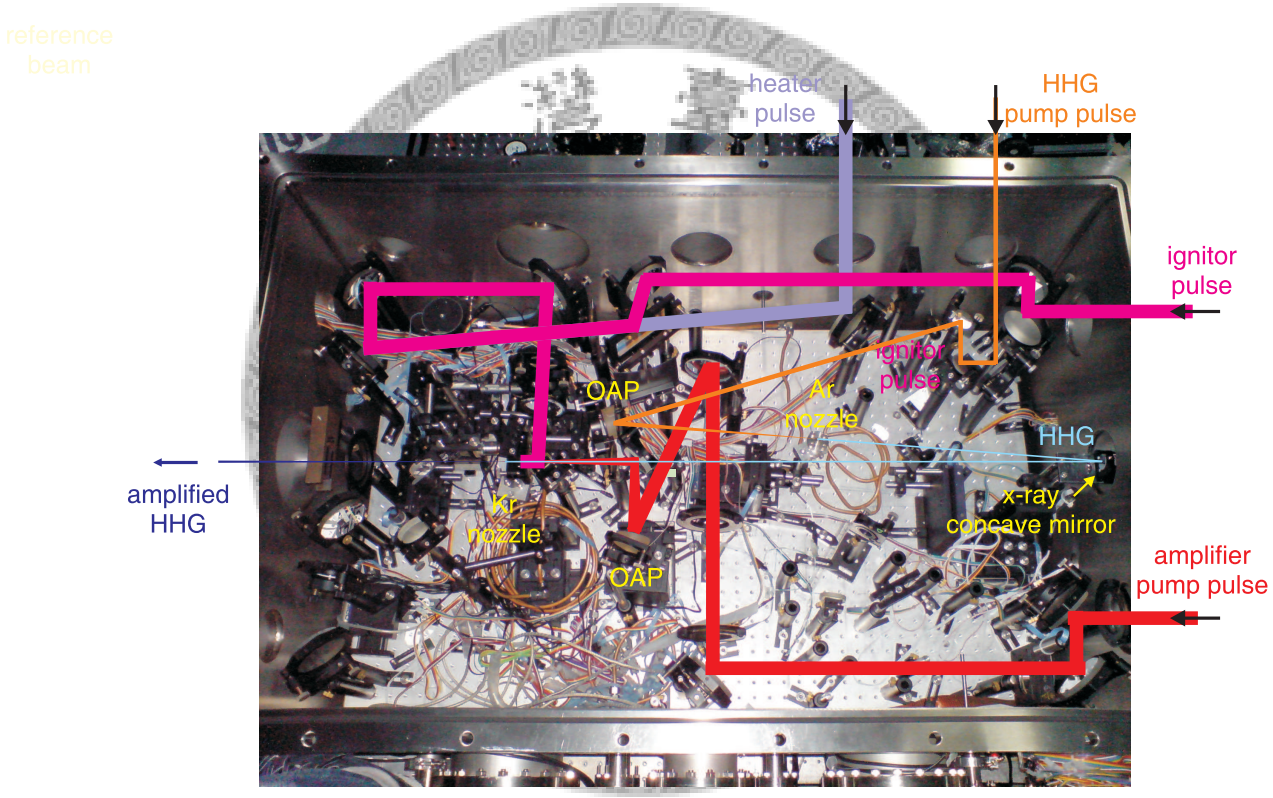

Figure 4.4: Photo of the experimental setup.

comes from the difference between the phase velocities of the fundamental wave and harmonic wave. Three major effects contribute to the dephasing between fundamental and harmonic field: (1) dispersion from the neutral atoms and the free electrons, (2) single-atom response depending on the driving laser intensity , and (3) the curved wave front in the focused driving laser beam (Gouy phase shift) [115]. The third one can be suppressed in a loose focusing geometry (large f-number), and the first two factors can be reduced by regulating the laser energy, laser spot size, and atom density. Besides, the laser pulse will suffer from ionization defocusing, which lowers the laser pulse intensity and thus reduces the effective interaction length. This defocusing effect can also be reduced in a loose focusing geometry, or it can be balanced by beam convergence through placing the focus at different positions with respect to the gas medium.

In addition to maximize the HHG emission, the harmonic frequency also should be matched to the given x-ray lasing line. In this experiment, the fundamental wavelength is 810 nm, so its 25th harmonic (32.4 nm) has a closed match with 32.8-nm Ni-like Kr lasing line. It has been suggested previously that the HHG spectrum could be tuned by changing the intensity or chirp of the fundamental beam. The increase of intensity will induce the ionization blue shift [116, 117], nonadiabatic blue shift [118, 114] or broadening of HHG spectrum [119]. And the laser chirp gives a red or blue shift spectrum, depending on positive of negative chirp. For example, the positively chirped laser pulse give red-shift harmonics because harmonics produced in the leading edge of the fundamental laser come from the red part of the laser spectrum. However, when changing the chirp, several parameters are varied at the same time, such as chirp, pulse duration, and laser intensity.

As mentioned above, several parameters will affect the efficiency of HHG, and they have to be controlled independently in this experiment. For doing this, an individual beam line is used as the driving laser of HHG seed. Hence, the energy and frequency of the 25th harmonic can be optimized by regulating the laser energy, laser chirp, gas pressure, laser focal position, and input beam diameter. After such a complicated optimization among the five parameters, an optimal condition can be found for maximum emission of the 25th harmonic, at which the HHG wavelength is close to but not exactly equal to that of Ni-like Kr lasing line. The final spectral matching is accomplished by tuning the laser chirp. In the following seeding experiments, the daily optimization is the fine adjustment of the wavelength of the 25th harmonic to coincide with that of Ni-like Kr lasing by adjusting the chirp of the driving laser, while the rest of parameters are fixed at this optimal

condition.

4.4.2 Spatial and Temporal Overlap

In the process of laser amplification, spatial and temporal overlap between the seed and the laser amplifier are crucial for extracting maximum energy from the amplifier, especially when strong spontaneous emission competes with the HHG seed in the waveguide-based x-ray amplifier. Note that four pulses with different focusing optics and purposes are involved in this experiment, making the overlap procedure more complicated. During the process, each step in the optimization procedure should be performed in order and with different diagnostic tools depending on the type of pulses.

Overall, this overlap procedure should start from the spatial overlap between the amplifier pump pulse and waveguide-forming pulses (ignitor and heater). Two preset iris pairs are used for aligning these pulses. After this alignment, an angular overlap within 1 mrad between these pulses can be achieved. Next, fine adjustment is achieved by checking the overlap between the amplifier pump pulse and waveguide-forming pulses from the entrance to the end of the gas jet with an online imaging system. Then, the angular overlap between the HHG and amplifier pump pulses is aligned to within 1 mrad by using two irises separated by approximately 1 m, representing a 10 μm error in space between the two beams for a 1-cm-long gas jet. Next, the spatial overlap between the HHG and amplifier pump pulses is further checked at the entrance and exit of the gas jet by using a relayed imaging system.

After doing the spatial overlap, the temporal overlap between the two pulses is checked by observing the near-field profile of the HHG pump pulse with the same relayed imaging system. If the HHG pump pulse arrives after the amplifier pump pulse, the profile of HHG pump pulse will pass through the plasma created by the amplifier pump pulse and then diffract. In contrast, if the HHG pump pulse arrives before the amplifier pump pulse, it will retain the same profile as without the amplifier pump pulse. Note that temporal overlap should be done after the spectral matching procedure. This is because the chirp of the seed pump pulse, one of the controlled parameters for spectral overlap, is varied by changing the distance between the grating pair of the compressor and thus changes the temporal delay between the seed and amplifier pump pulses as well. Moreover, a more precise optimization of spatial and temporal overlap is achieved by maximizing the x-ray output

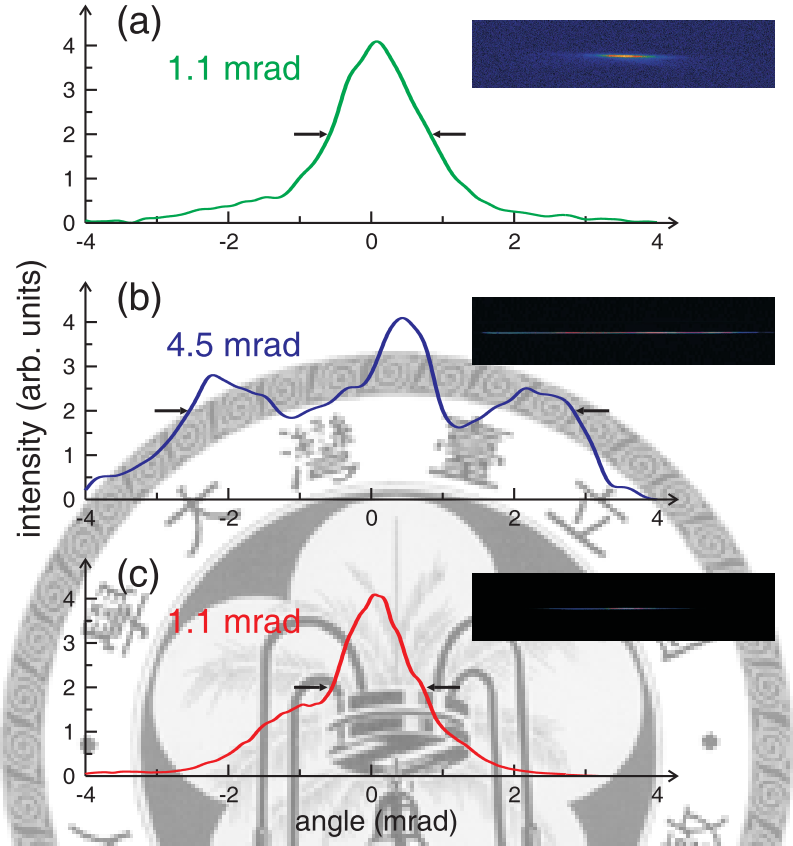

Figure 4.5: Angular profiles of (a) the HHG seed, (b) the Ni-like Kr ASE soft-x-ray laser at 32.8-nm, and (c) the seeded soft-x-ray laser. The insets in (a), (b), and (c) are the CCD raw images of the HHG seed, the Ni-like Kr ASE soft-x-ray laser at 32.8-nm, and the seeded soft-x-ray laser, respectively.

measured by using a flat-field spectrometer, which can be used to characterize the gain duration and transverse gain region. The results will be addressed in the following section.

4.5 Characterization of the Seeded Soft X-Ray Laser

4.5.1 Spectrum and Angular Profile

Figure 4.5 shows the angular profiles of the HHG seed, the ASE soft-x-ray laser, and the seeded soft-x-ray laser. With seeding the divergence of the soft-x-ray laser is greatly reduced from 4.5 mrad to 1.1 mrad in FWHM,

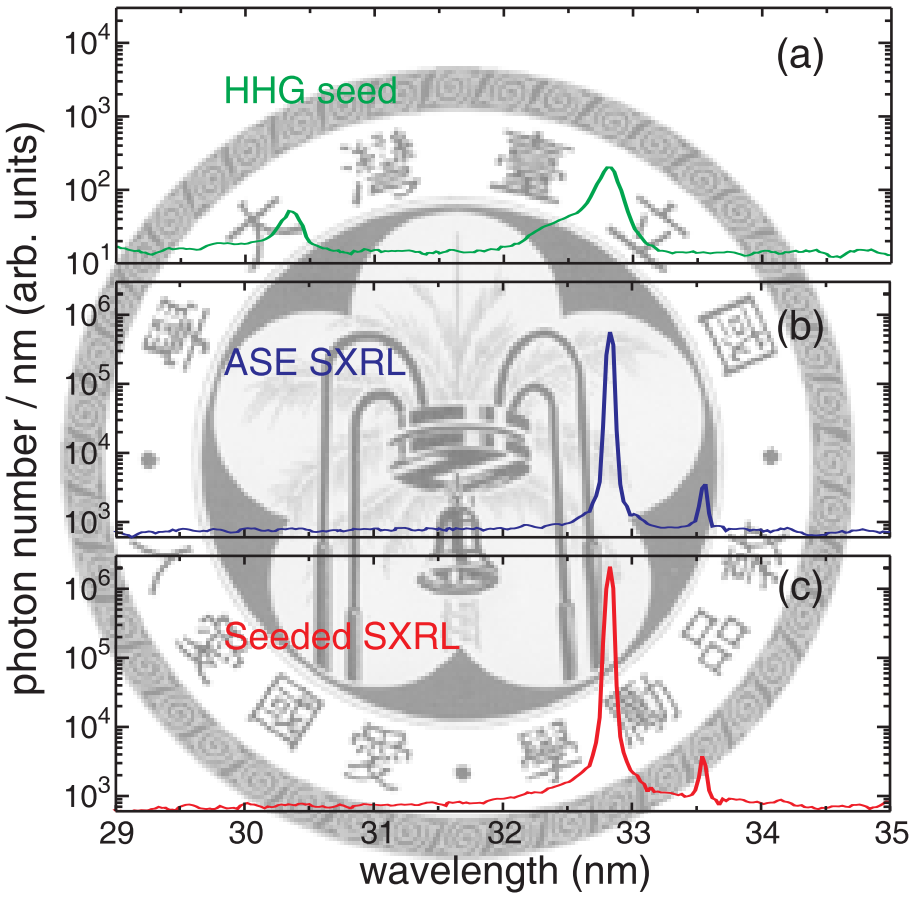

Figure 4.6: X-ray spectra of (a) the HHG seed, (b) the Ni-like Kr ASE soft-x-ray laser at 32.8-nm, and (c) the seeded soft-x-ray laser.

which is about the same as that of the HHG seed. The pointing and angular profile of the seeded soft-x-ray laser follow that of the HHG seed and the fluctuation is negligible ($\approx$ 0.13 mrad). In contrast, the angular profile of the ASE soft-x-ray laser has a much larger fluctuation. The direction of peak intensity changes from shot to shot within the 4.5-mrad divergence angle. These indicate that the output of the soft-x-ray laser is dominated by the amplification of the HHG seed. Since the ASE has a roughly flat-top distribution extending from -2.5 mrad to $+2.5$ mrad and the HHG is mostly distributed from -2 mrad to $+2$ mrad, the intensity of the seeded soft-x-ray laser at $+(-)2.5$ mrad can be used to obtain an upper limit of the contribution from residual ASE in the output of the seeded soft-x-ray laser. The residual ASE contribution is less than 10%. Figure 4.6 shows the spectra for the HHG seed, the ASE soft-x-ray laser, and the seeded soft-x-ray laser. The photon numbers for the HHG seed, ASE, and seeded soft-x-ray lasers are 1×10^7, 1×10^{11}, and 1×10^{11}, respectively. The amplification factor is defined as $(S_{\text{seeded}} - S_{\text{ASE}})/S_{\text{seed}}$, where S_{seeded}, S_{ASE}, and S_{seed} are the photon numbers of the seeded soft-x-ray laser, the residual ASE upon seeding, and the HHG seed, respectively. Since the residual ASE contribution is less than 10%, the amplification factor can be obtained approximately as $S_{\text{seeded}}/S_{\text{seed}}$, which is about 10^4. The absolute photon number of the seeded soft-x-ray laser is about the same as that of the ASE soft-x-ray laser. The energy fluctuation of the seeded soft-x-ray laser is about 10%, which is dominated by that of the soft-x-ray amplifier [53]. The increase in the output of the 32.8-nm lasing line upon seeding observed in Fig. 4.6 is simply a result of the reduction of beam divergence which changes the collection efficiency of the spectrometer grating in the dispersion plane. In contrast, the photon number and beam divergence for the additional lasing line at 33.5 nm do not change with seeding, because the wavelength does not match with the HHG. This indicates that the waveguide-based ASE soft-x-ray laser already reaches the strongly saturated regime, in which the energy stored in the population inversion for most part of the length of the amplifier are efficiently extracted to the laser output even with only the spontaneous emission, so that the photon number cannot be significantly increased upon seeding. According to the measured parameters and assuming a pulse duration which is limited by bandwidth ($\Delta\lambda/\lambda = 10^{-4}$), the peak spectral brightness can be estimated to be 3.3×10^{26} photons/sec/mm^2/mrad^2 in 0.01% bandwidth. With seeding the peak spectral brightness is 500 times higher than the ASE soft x-ray laser.

For comparison, the same experiment with a soft-x-ray amplifier without waveguide is also carried out. In this experiment, we use a 5-mm slit nozzle

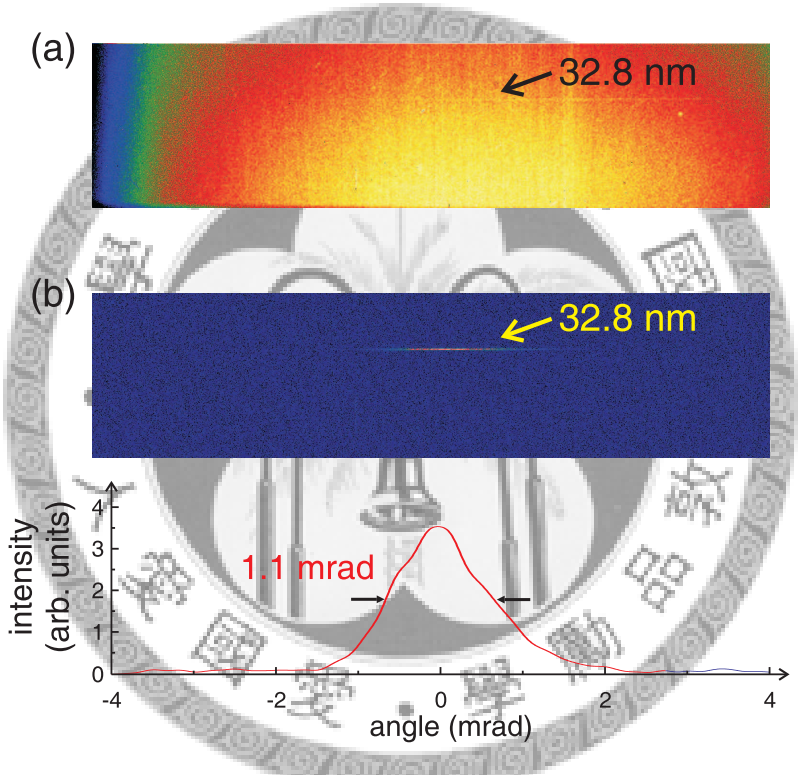

Figure 4.7: Angular profiles of (a) the ASE soft-x-ray laser, and (b) the seeded soft-x-ray laser in the case of without waveguide.

rather than the 1-cm slit nozzle. This is because when there is no plasma waveguide maximum output was obtained with the 5-mm slit nozzle. For the 1-cm slit nozzle, ionization-induced refraction of the pump pulse occurs at the back end of the gas jet, which results in strong re-absorption because of insufficient pumping. The atom density and the focal position of the pump pulse is optimized for maximizing x-ray output [41, 42, 74]. The optimal atom density and focal position are 1×10^{18} cm^{-3} and 1750 μm after the entrance of the cluster jet, respectively. The pump pulse energy is 290 mJ. Figure 4.7 shows the angular profiles of the ASE soft-x-ray laser, and the seeded soft-x-ray laser in the case of without waveguide. Similarly, with seeding the divergence of the soft-x-ray laser is greatly reduced to 1.1 mrad in FWHM, which is about the same as that of the HHG seed. The photon numbers for ASE and seeded soft-x-ray lasers are 6×10^8 and 2×10^9, respectively. The 3-fold increase in photon number upon seeding shows that the non-waveguide-based amplifier is not fully saturated. The HHG seed is amplified by a factor of 200. This is much lower than that of the waveguide-based amplifier.

4.5.2 Measurement of Polarization State

The seeded soft x-ray laser is further characterized by using a soft x-ray polarization analyzer. The analyzer consists of two multilayer soft x-ray mirrors mounted on a motorized rotation stage. The mirror reflectivity is highly polarization dependent. The doubly reflected signal is collected by a micro-channel-plate detector located after the analyzer. The experimental setup for polarization measurement is illustrated in Fig. 4.8. The extinction ratio (energy of s-polarized beam/energy of p-polarized beam) of the analyzer is measured to be better than 19 by using the linearly polarized HHG seed as the light source, and the results are shown in Fig. 4.9. During the polarization measurement, the angle of the polarization analyzer is varied by the motorized rotation stage. Figure 4.10(a) and (c) show the intensities of the HHG seed and the seeded soft x-ray laser as functions of analyzer angle for both p-polarized and s-polarized HHG seed. Figure 4.9(b) shows the intensity of the ASE soft x-ray laser as a function of analyzer angle. As expected, the polarization of the seeded soft x-ray laser follows that of the HHG seed, and the ASE soft x-ray laser is unpolarized.

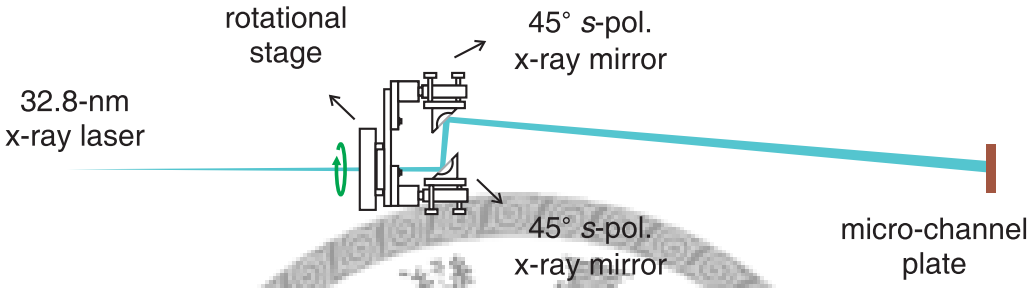

Figure 4.8: Experimental setup of polarization measurement for a 32.8-nm Kr^{8+} x-ray laser. MCP: micro-channel-plate detector

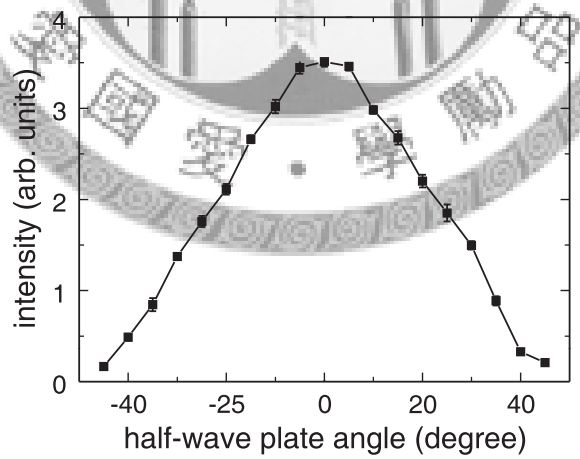

Figure 4.9: Intensity of the HHG seed as a function of half-wave plate angle.

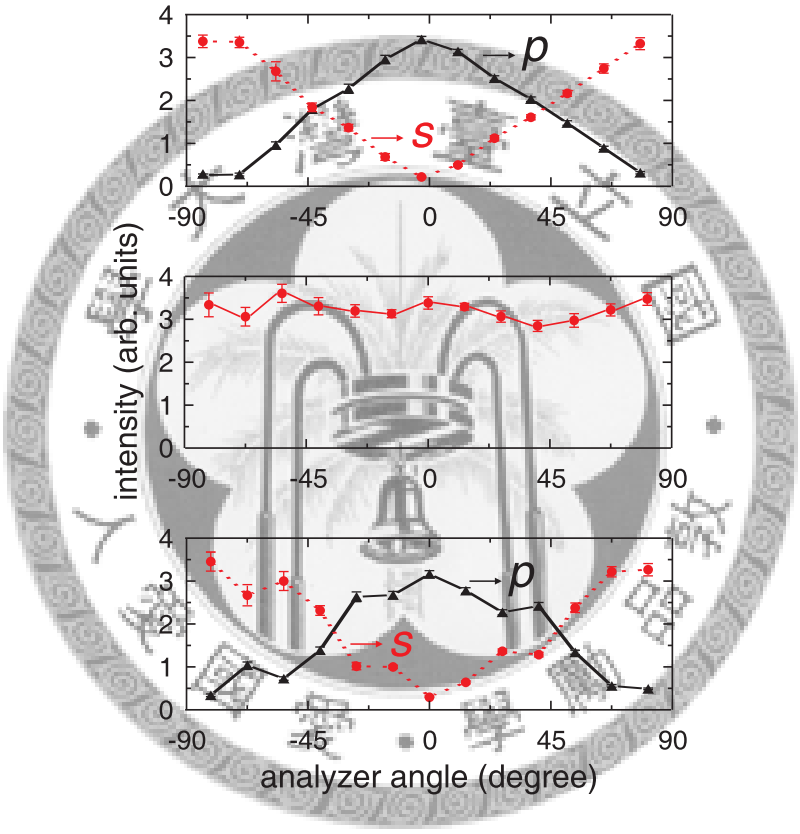

Figure 4.10: (a) Intensity of the HHG seed as a function of analyzer angle. (b) Intensity of the ASE soft x-ray laser as a function of analyzer angle. (c) Intensity of the seeded soft x-ray laser as a function of analyzer angle.

4.5.3 Measurement of Gain Duration

Figure 4.11 shows the angular profiles of the seeded soft-x-ray laser for various time delays between the HHG seed and the amplifier pump pulse, and the inset shows that of the integrated soft-x-ray signal. This provides a measurement of the gain evolution of the soft-x-ray amplifier [96]. High gain can be obtained with a delay between 1 ps and 4 ps and the maximum is at 2.0 ps. In the seeded soft-x-ray amplifier without waveguide, high gain occurs for a delay between 2 ps and 7 ps and the maximum is at 3 ps, as shown in Fig. 4.12. That is, with the plasma waveguide the gain rises and falls faster. This indicates that the electron-ion collisional rate is higher for the waveguide-based soft-x-ray amplifier, which is a result of the much higher on-axis electron density observed with interferometry [53] and possibly higher electron temperature, leading to faster collisional excitation rate and over-ionization rate.

4.5.4 Measurement of Transverse Gain Region

Optimization of spatial overlap between the HHG seed and the waveguide-based amplifier is crucial for extracting maximum energy from the amplifier. For this, the focusing concave mirror for the HHG seed is mounted on a three-axis motorized translation stage. Figure 4.13 shows the angular profile in the horizontal plane for various horizonal positions of the HHG seed focus with respect to the longitudinal axis of the amplifier. When the seed axis and the amplifier axis are overlapped optimally, the intensity of the amplified seed reaches the maximum and the beam divergence shrinks to that of the HHG seed. If the HHG seed is shifted away from the position of optimal overlap, the peak intensity goes down and the beam divergence increases. This measurement shows that the transverse size of the amplifier is about 36 μm FWHM, as shown in Fig. 4.14. When the HHG seed does not overlap with the amplifier, the ASE lasing dominates the output. The dependence on the vertical shift shows roughly the same result, as shown in Fig. 4.15. Figure 4.16 shows the intensity of the amplified seed as a function of the longitudinal position of the seed focus. The maximum amplification is obtained when the focus of the HHG seed is placed at 2 mm behind the entrance of the plasma waveguide. Under this condition, the beam sizes of the HHG seed at various longitudinal positions with respect to the waveguide entrance are measured by using a knife edge mounted on a motorized translation stage. The result is shown in Fig. 4.17. Under the condition of maximum amplification, the beam

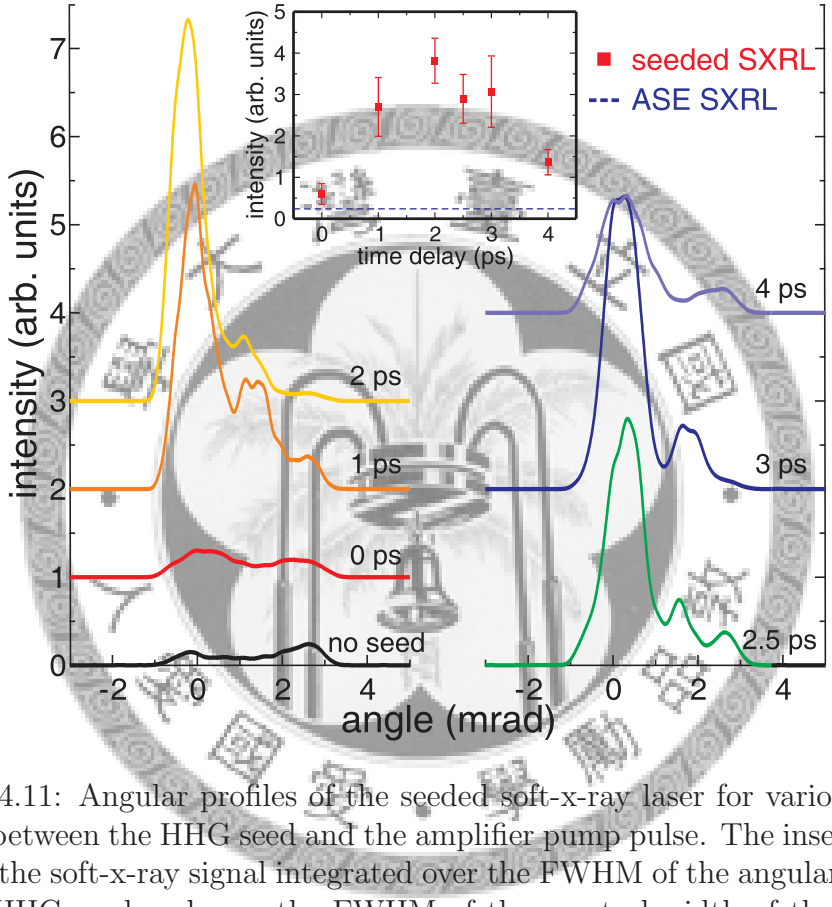

Figure 4.11: Angular profiles of the seeded soft-x-ray laser for various time delays between the HHG seed and the amplifier pump pulse. The inset shows that of the soft-x-ray signal integrated over the FWHM of the angular profile of the HHG seed and over the FWHM of the spectral width of the seeded soft-x-ray laser. The dashed line indicates that of the ASE soft-x-ray laser. The error bars indicate the standard deviation over 5 laser shots. The other parameters are the same as that described for the waveguide-based x-ray amplifier.

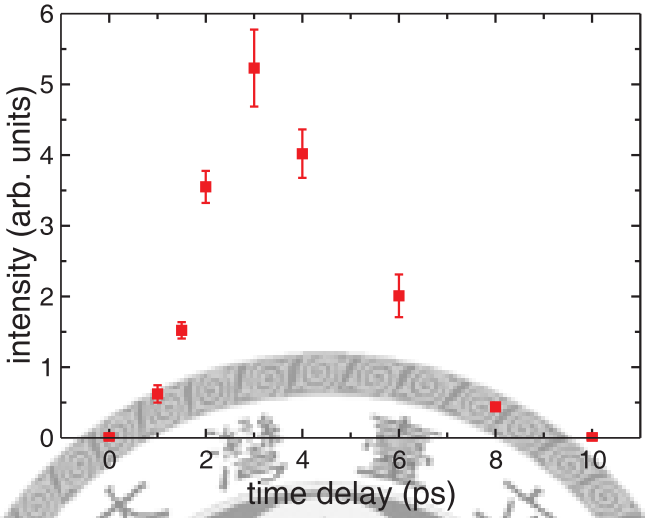

Figure 4.12: Soft-x-ray signal integrated over the FWHM of the angular profile of the HHG seed and over the FWHM of the spectral width of the seeded soft-x-ray laser for various time delays between the HHG seed and the amplifier pump pulse. The error bars indicate the standard deviation over 25 laser shots. The other parameters are the same as that described for the pump-only x-ray amplifier.

sizes of the HHG seed at all positions within the waveguide matches well with the transverse size of the amplifier gain region. This leads to high energy-extraction efficiency whether the seed is guided by the amplifier waveguide or not.

4.5.5 Measurement of Spatial Coherence

The spatial coherence lengths of the seeded soft x-ray laser and the ASE soft x-ray laser are measured by Young's double-slit interferometry, as stated in Sec. 2.6. The slits are all 15-μm wide and are machined by our ultra-short high-intensity laser. Clearly, the seeded soft x-ray laser has a spatial coherence length larger than that without seeding when measured at the same location, but the actual enhancement factor of the coherence length cannot be determined because the fringe visibilities for large slit separations are also degraded by the finite pixel size of the x-ray CCD camera in the current setup. However, the spatial coherence of a laser beam, which affects its focusability of the laser beam, is determined by the ratio of the spatial coherence length to the beam diameter at the location of measurement [120].

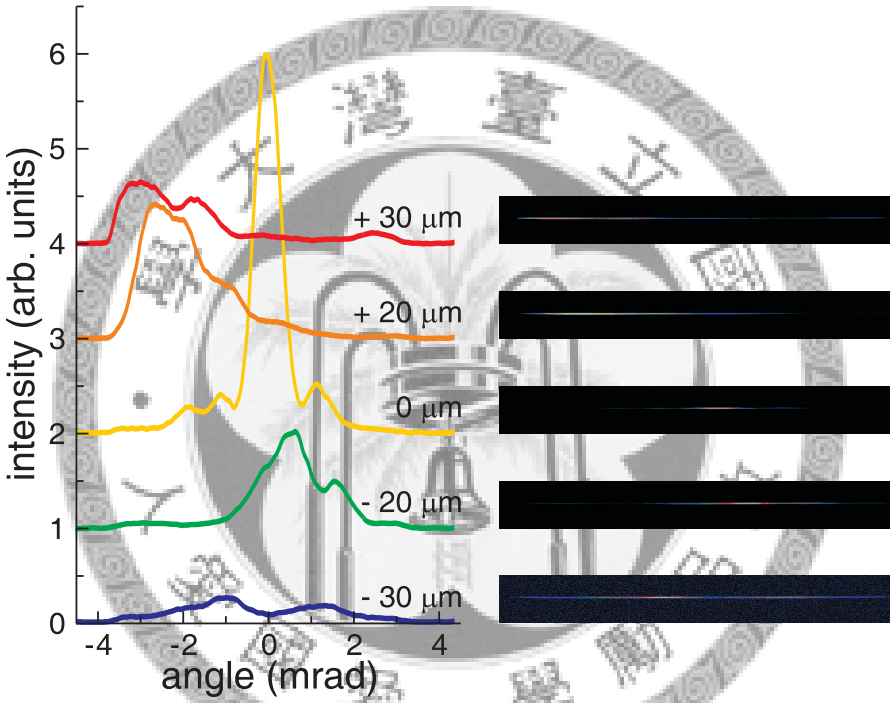

Figure 4.13: Angular profiles in the horizontal plane for various horizonal positions of the HHG-seed focus with respect to the longitudinal axis of the amplifier. The error bars indicate the standard deviation over 5 laser shots. The other parameters are the same as that described in Sec. 4.2.

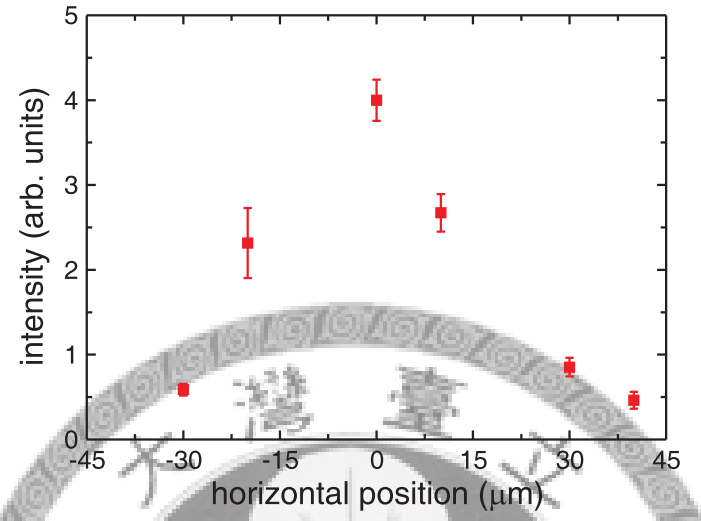

Figure 4.14: Intensity of the amplified seed as a function of horizontal position of the HHG-seed focus. The error bars indicate the standard deviation over 5 laser shots. The other parameters are the same as that described in Sec. 4.2.

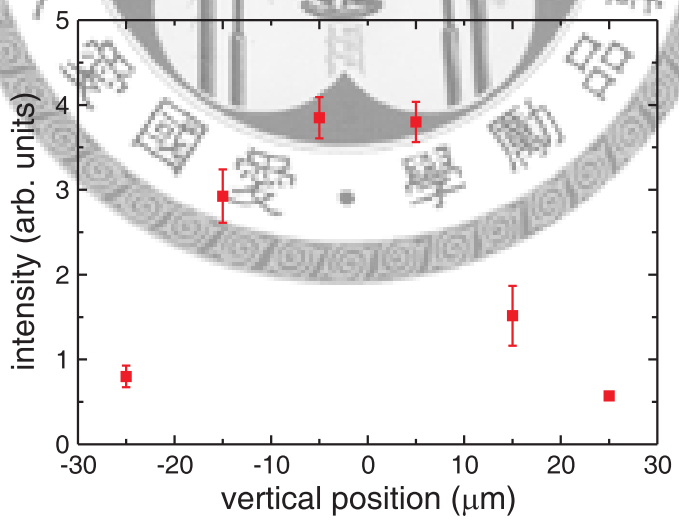

Figure 4.15: Intensity of the amplified seed as a function of vertical position of the HHG-seed focus. The error bars indicate the standard deviation over 5 laser shots. The other parameters are the same as that described in Sec. 4.2.

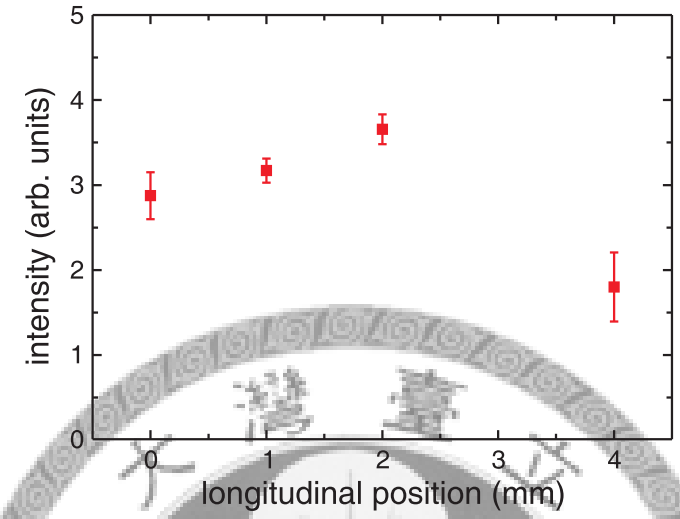

Figure 4.16: Intensity of the amplified seed as a function of longitudinal position of the HHG-seed focus. The error bars indicate the standard deviation over 5 laser shots. The other parameters are the same as that described in Sec. 4.2.

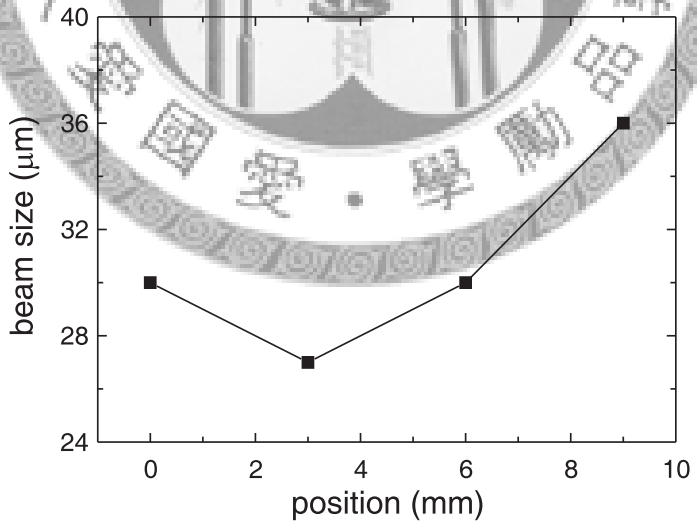

Figure 4.17: Beam size of the HHG seed as a function of longitudinal position with respect to the waveguide entrance when the HHG-seed focus is positioned at 2 mm behind the waveguide entrance.

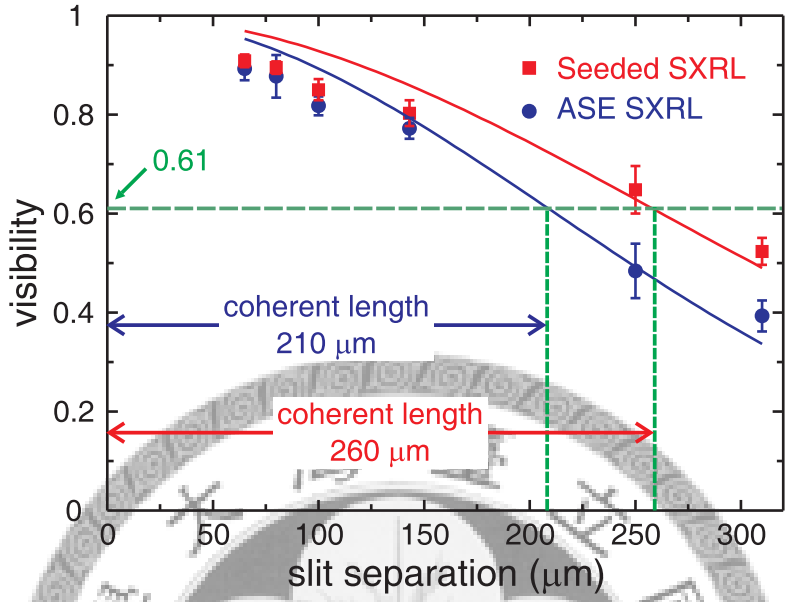

Figure 4.18: Fringe visibilities as functions of slit separation and their Gaussian-fit curves for the seeded soft-x-ray laser (square) and the ASE soft-x-ray laser (circle), respectively.

Therefore, the spatial coherence of the seeded soft x-ray laser is enhanced by at least a factor of four with respect to the ASE soft x-ray laser, in view of the four-fold reduction in beam divergence (beam diameter at the location of measurement), even if the spatial coherence length at this location does not improve much upon seeding.

4.6 Summary

In summary, we report the success of HHG seeding in a waveguide-based OFI soft-x-ray amplifier. By using HHG as a seed and an ASE soft x-ray laser as an amplifier, we can generate intense soft x-ray pulses with small divergence, enhanced spatial coherence, and controlled polarization. With seeding the spectral brightness is increased 500 times and reaches 3.4×10^{26} photons/sec/mm^2/mrad^2 in 0.01% bandwidth. Table 4.1 shows the comparison of our soft x-ray laser with synchrotron radiation in Taiwan. Owing to the good spatiotemporal quality and high spectral density of the seeded soft x-ray lasers, the peak spectral brightness is about 11 orders of magnitude larger than that of synchrotron radiation within 0.01% of the bandwidth,

light source	NSRRC (Taiwan)	(ASE) soft x-ray laser	(HHG seeding) soft x-ray laser
pulse duration	100 ps	5 ps [43]	200 fs†
repetition rate	10^6	10 Hz	10 Hz
wavelength	tunable	discrete set (32.8 nm)	discrete set (32.8 nm)
average spectral brightness at 32.8 nm	9.8×10^{12}	3.9×10^{13}	6.6×10^{14}
peak spectral brightness at 32.8 nm	7.9×10^{14}	7.9×10^{23}	3.3×10^{26}

* spectral brightness: photons/sec/mm^2/mrad^2 in 0.01% bandwidth
† assuming the pulse duration is limited by bandwidth

Table 4.1: Comparison of soft x-ray lasers in this work with synchrotron radiation in Taiwan.

which is very advantageous in applications requiring high photon flux in a narrow bandwidth. In addition, Tab. 4.2 shows the comparison of the seeded waveguide-based soft x-ray laser with other seeded soft x-ray lasers constructed by either different pumping mechanism or target types in the world.

target	amplification method	pumping mechanism	wavelength (nm)	photon number per pulse	divergent angle (mrad)
Kr	ASE [121]	OFI†	32.8	3×10^9	12
(gas cell)	HHG seeding [82]	(no waveguide)		1.5×10^{11}	1
*Kr	ASE [53]	OFI	32.8	1×10^{11}	4.5
(gas jet)	HHG seeding [122]	(with waveguide)		1×10^{11}	1.1
Ti	ASE	GRIP‡	32.6	N.A.	10
(solid slab)	HHG seeding [102]			1×10^{10}	2.2
Mo	ASE [123]	GRIP	18.9	1.4×10^{10}	10
(solid slab)	HHG seeding [103]			7.2×10^9	0.7
Ag	ASE [124]	GRIP	13.9	8.1×10^{10}	10
(solid slab)	HHG seeding [103]			N.A.	0.7
Cd	ASE [125]	GRIP	13.2	3×10^{10}	10
(solid slab)	HHG seeding [104]			N.A.	0.66

* Our soft x-ray laser

† OFI: optical-field ionization

‡ GRIP: grazing-incidence pumping

Table 4.2: Comparison of various soft x-ray lasers in the world.

Chapter 5

Conclusion and Perspective

As mentioned in the beginning of this thesis, the recent rapid progress in technology has opened an opportunity to create the ultrashort coherent x-ray sources. Considering the future needs of these short-wavelength coherent sources for research in academia and industry, it goes without saying that much effort is being devoted to developing them with a compact size, affordable expense, and high operation rate. No doubt, this is the major objective of this thesis.

All experiments here were performed by using a 10-TW 10-Hz table-top laser system. The first accomplishment was the strong enhancement of OFI soft x-ray lasing by using a preformed plasma waveguide prepared by using the axicon ignitor-heater scheme. With a 9-mm-long pure krypton plasma waveguide, 400-fold enhancement was demonstrated for 32.8 nm Kr^{8+} lasing with respect to the case without a plasma waveguide, showing the advantages of plasma waveguide in increasing the gain and the length of an x-ray laser. An output level of 8×10^{10} photons/pulse is reached at an energy conversion efficiency of 2×10^{-6}. The peak spectral brightness can be estimated to be 7.9×10^{23} photons/sec/mm^2/mrad^2 in 0.01% bandwidth, higher than that of synchrotron radiation in Taiwan.

The same guiding technique was further used to achieve various OFI x-ray lasing: Xe^{8+} lasing at 41.8-nm and Ar^{8+} lasing at 46.9-nm. To have a deep insight into the characteristics of waveguide-based OFI soft x-ray lasers, the experimental results in an extensive parameter space are studied. The dependences on heater-pump delay and heater energy show that a higher heater

energy and a shorter heater-pump delay should be used for changing from Xe, Kr, to Ar, consistent with the increase in the required pump intensity for producing the lasing ionization stage. The exponential growth and saturation with increasing pump energy before over-ionization is observed as expected. With a plasma waveguide the restriction on the on-axis ion density set by ionization-induced refraction is removed so that one can obtain a higher gain coefficient. The dependence of lasing output on pump polarization ellipticity becomes less significant with a plasma waveguide, which can be ascribed to strong saturation and significant contribution from other heating mechanisms in addition to above-threshold-ionization heating. The enhancement effect of an optically preformed plasma waveguide is more dramatic for x-ray lasing that requires higher pump intensity and has a smaller gain coefficient. With Ar^{8+} plasma waveguide, besides the strong lasing line at 46.9 nm, two additional lasing lines at 45.1 nm and 46.5 nm are observed. The lasing of these two lines is driven by the self-photopumping mechanism. The strong output of these two lasing lines verifies the high ion density and high gain of the optically preformed plasma waveguide. With a Kr/Ar mixed-gas plasma waveguide multi-species parallel x-ray lasing is also demonstrated, showing the versatility of optically preformed plasma waveguide.

Finally, high harmonic generation (HHG) seeding in a waveguide-based OFI soft-x-ray amplifier was demonstrated. Great reduction in divergence, controlled polarization, and enhanced spatial coherence were achieved in the seeded soft-x-ray laser. With seeding the peak spectral brightness is increased 500 times and reaches 3.3×10^{26} photons/sec/mm^2/mrad^2 within 0.01% of the bandwidth. Such a source can provide a much larger x-ray pulse energy and much narrower bandwidth than high harmonic generation, with much lower cost and much smaller size than x-ray free electron laser. The integration of gas-jet-based high-harmonic seed and gas-jet-based optically-preformed plasma waveguide amplifier should provide a practical soft x-ray tool for scientific research.

The seeded soft x-ray laser retains many excellent properties of HHG; one of them is the polarization state. It is known that linearly polarized driving lasers produce linearly polarized harmonics. In contrast, a circularly polarized laser does not produce circularly polarized harmonics, but rather no harmonics at all. This is because a free electron which is driven by a circularly polarized field does not have a chance to approach and recombine with its parent ion and thus no emission occurs. However, it has been shown that circularly polarized harmonics can be generated by using two-color circularly polarized pump pulses for high harmonic generation [126, 127]. Further-

more, arbitrarily-polarized high-order harmonics can be generated by two-color pump pulses with the appropriate elliptical polarizations. With this change soft-x-ray lasers of arbitrarily polarization can be readily achieved in the future.

Pursuit of shorter wavelength is a non-stop progress in the development of x-ray lasers. The H-like nitrogen ion is a proper candidate for the sub-10-nm soft x-ray lasing [128]. It is desirable because of the short wavelength: 2.5 nm and 13.4 nm; one is in the "water window" region and the other is the common wavelength used for EUV lithography. The laser intensity for the fully ionized nitrogen is greater 3×10^{19} W/cm^2, and it can be achieved with our 100-TW laser system at the National Central University. The main issue is the overheating of the electrons under such a high-intensity laser field. Although the OFI scheme with the linearly polarized pump laser can provide very cold electrons, the high-intensity laser field may induce other important heating source for the electrons of the plasma, such as the Raman instability. However, by mixing nitrogen with the hydrogen gas which can provide the low-temperature electrons may provide a solution for cooling down the over-heated plasma [89]. On the other hand, the Ni-like xenon is another good candidate for pushing soft x-ray laser to the sub-10-nm region [40, 129], because it has a much higher ionization stage (Xe^{26+}) than that of Pd-like xenon ion. As suggested in Ref. [40], Ni-like Xe lasing will require a higher pulse energy or a method of channeling a tightly focused pumping laser beam over a distance longer than its confocal parameter. Combining our 100-TW laser system with the technique of the optically preformed plasma waveguide, these two conditions can be satisfied at the same time. Therefore, generation of 9.98 nm Xe^26+ lasing based on the 100-TW laser system and optically preformed plasma waveguide is highly expected and attainable in the near future.

Chapter 5. Conclusion and Perspective

References

[1] W. Roentgen, Nature **53**, 274 (1896).

[2] T. H. Maiman, "Stimulated optical radiation in ruby," Nature **187**, 493–494 (1960).

[3] US Departement of Energy (DOE) Report (2007).

[4] R. C. Elton, *X-ray lasers* (Academic Press, San Diego, CA, 1990).

[5] J. A. Bearden, "X-ray wavelengths," Rev. Mod. Phys. **39**, 78 (1967).

[6] D. R. Lide, ed., *CRC Handbook of Chemistry and Physics* (CRC Press, Inc., 2000 Corporate Blvd., N.W. ,Boca Raton, Florida 33431, 1993), 74th ed.

[7] Z. Chang, A. Rundquist, H. Wang, M. M. Murnane, and H. C. Kapteyn, "Generation of coherent soft x rays at 2.7 nm using high harmonics," Phys. Rev. Lett. **79**, 2967–2970 (1997).

[8] C. Winterfeldt, C. Spielmann, and G. Gerber, "Colloquium: Optimal control of high-harmonic generation," Rev. Mod. Phys. **80**, 117–140 (2008).

[9] P. M. Paul, E. S. Toma, P. Breger, G. Mullot, F. Auge, P. Balcou, H. G. Muller, and P. Agostini, "Observation of a train of attosecond pulses from high harmonic generation," Science **292**, 1689–1692 (2001).

[10] J.-F. Hergott, M. Kovacev, H. Merdji, C. Hubert, Y. Mairesse, E. Jean, P. Breger, P. Agostini, B. Carré, and P. Salières, "Extreme-ultraviolet high-order harmonic pulses in the microjoule range," Phys. Rev. A **66**, 021,801 (2002).

[11] A. E. Siegman, *Lasers* (University Science Books, 55D Gate Five Road, Sausalito, CA 94965, USA, 1986).

[12] V. Ayvazyan, N. Baboi, J. Bahr, V. Balandin, B. Beutner, A. Brandt, I. Bohnet, A. Bolzmann, R. Brinkmann, O. Brovko, J. Carneiro, S. Casalbuoni, M. Castellano, P. Castro, L. Catani, E. Chiadroni, S. Choroba, A. Cianchi, H. Delsim-Hashemi, G. Di Pirro, M. Dohlus, S. Dusterer, H. Edwards, B. Faatz, A. Fateev, J. Feldhaus, K. Flottmann, J. Frisch, L. Frohlich, T. Garvey, U. Gensch, N. Golubeva, H. Grabosch, B. Grigoryan, O. Grimm, U. Hahn, J. Han, M. Hartrott, K. Honkavaara, M. Huning, R. Ischebeck, E. Jaeschke, M. Jablonka, R. Kammering, V. Katalev, B. Keitel, S. Khodyachykh, Y. Kim, V. Kocharyan, M. Korfer, M. Kollewe, D. Kostin, D. Kramer, M. Krassilnikov, G. Kube, L. Lilje, T. Limberg, D. Lipka, F. Lohl, M. Luong, C. Magne, J. Menzel, P. Michelato, V. Miltchev, M. Minty, W. Moller, L. Monaco, W. Muller, M. Nagl, O. Napoly, P. Nicolosi, D. Nolle, T. Nunez, A. Oppelt, C. Pagani, R. Paparella, B. Petersen, B. Petrosyan, J. Pfluger, P. Piot, E. Plonjes, L. Poletto, D. Proch, D. Pugachov, K. Rehlich, D. Richter, S. Riemann, M. Ross, J. Rossbach, M. Sachwitz, E. Saldin, W. Sandner, H. Schlarb, B. Schmidt, M. Schmitz, P. Schmuser, J. Schneider, E. Schneidmiller, H. Schreiber, S. Schreiber, A. Shabunov, D. Sertore, S. Setzer, S. Simrock, E. Sombrowski, L. Staykov, B. Steffen, F. Stephan, F. Stulle, K. Sytchev, H. Thom, K. Tiedtke, M. Tischer, R. Treusch, D. Trines, I. Tsakov, A. Vardanyan, R. Wanzenberg, T. Weiland, H. Weise, M. Wendt, I. Will, A. Winter, K. Wittenburg, M. Yurkov, I. Zagorodnov, P. Zambolin, and K. Zapfe, "First operation of a free-electron laser generating GW power radiation at 32 nm wavelength," Eur. Phys. J. D **37**, 297–303 (2006).

[13] W. Ackermann, G. Asova, V. Ayvazyan, A. Azima, N. Baboi, J. Baehr, V. Balandin, B. Beutner, A. Brandt, A. Bolzmann, R. Brinkmann, O. I. Brovko, M. Castellano, P. Castro, L. Catani, E. Chiadroni, S. Choroba, A. Cianchi, J. T. Costello, D. Cubaynes, J. Dardis, W. Decking, H. Delsim-Hashemi, A. Delserieys, G. Di Pirro, M. Dohlus, S. Duesterer, A. Eckhardt, H. T. Edwards, B. Faatz, J. Feldhaus, K. Floettmann, J. Frisch, L. Froehlich, T. Garvey, U. Gensch, C. Gerth, M. Goerler, N. Golubeva, H.-J. Grabosch, M. Grecki, O. Grimm, K. Hacker, U. Hahn, J. H. Han, K. Honkavaara, T. Hott, M. Huening, Y. Ivanisenko, E. Jaeschke, W. Jalmuzna, T. Jezynski, R. Kammering, V. Katalev, K. Kavanagh, E. T. Kennedy, S. Khodyachykh, K. Klose, V. Kocharyan, M. Koerfer, M. Kollewe, W. Koprek, S. Korepanov, D. Kostin, M. Krassilnikov, G. Kube, M. Kuhlmann, C. L. S. Lewis, L. Lilje, T. Limberg, D. Lipka, F. Loehl, H. Luna, M. Luong,

M. Martins, M. Meyer, P. Michelato, V. Miltchev, W. D. Moeller, L. Monaco, W. F. O. Mueller, O. Napieralski, O. Napoly, P. Nicolosi, D. Noelle, T. Nunez, A. Oppelt, C. Pagani, R. Paparella, N. Pchalek, J. Pedregosa-Gutierrez, B. Petersen, B. Petrosyan, G. Petrosyan, L. Petrosyan, J. Pflueger, E. Ploenjes, L. Poletto, K. Pozniak, E. Prat, D. Proch, P. Pucyk, P. Radcliffe, H. Redlin, K. Rehlich, M. Richter, M. Roehrs, J. Roensch, R. Romaniuk, M. Ross, J. Rossbach, V. Rybnikov, M. Sachwitz, E. L. Saldin, W. Sandner, H. Schlarb, B. Schmidt, M. Schmitz, P. Schmueser, J. R. Schneider, E. A. Schneidmiller, S. Schnepp, S. Schreiber, M. Seidel, D. Sertore, A. V. Shabunov, C. Simon, S. Simrock, E. Sombrowski, A. A. Sorokin, P. Spanknebel, R. Spesyvtsev, L. Staykov, B. Steffen, F. Stephan, F. Stulle, H. Thom, K. Tiedtke, M. Tischer, S. Toleikis, R. Treusch, D. Trines, I. Tsakov, E. Vogel, T. Weiland, H. Weise, M. Wellhoeffer, M. Wendt, I. Will, A. Winter, K. Wittenburg, W. Wurth, P. Yeates, M. V. Yurkov, I. Zagorodnov, and K. Zapfe, "Operation of a free-electron laser from the extreme ultraviolet to the water window," Nat. Photonics **1**, 336–342 (2007).

[14] *from http://en.wikipedia.org/wiki/.*

[15] J. J. Rocca, "Table-top soft x-ray lasers," Rev. Sci. Instrum. **70**, 3799–3827 (1999).

[16] D. L. Matthews, P. L. Hagelstein, M. D. Rosen, M. J. Eckart, N. M. Ceglio, A. U. Hazi, H. Medecki, B. J. MacGowan, J. E. Trebes, B. L. Whitten, E. M. Campbell, C. W. Hatcher, A. M. Hawryluk, R. L. Kauffman, L. D. Pleasance, G. Rambach, J. H. Scofield, G. Stone, and T. A. Weaver, "Demonstration of a soft x-ray amplifier," Phys. Rev. Lett. **54**, 110–113 (1985).

[17] S. Suckewer, C. H. Skinner, H. Milchberg, C. Keane, and D. Voorhees, "Amplification of stimulated soft-x-ray emission in a confined plasma column," Phys. Rev. Lett. **55**, 1753–1756 (1985).

[18] M. A. Dugury and P. M. Rentzepis, "Some approach to vacuum uv x-ray lasers," Appl. Phys. Lett. **10**, 350–352 (1967).

[19] H. C. Kapteyn, "Photoionization-pumped x-ray lasers using ultrashort-pulse excitation," Appl. Opt. **31**, 4931–4939 (1992).

[20] B. A. Norton and N. J. Peacock, "Population inversion in laser-produced plasmas by pumping with opacity-broadened lines," J. Phys. B **8**, 989–996 (1975).

[21] W. B. Bridges, *"Ionized gas lasers"in Handbook of Laser Science and Technol. Sec. 2* (CRC Press, Inc., 2000 Corporate Blvd., N. W. Boca Raton, Florida 33431, 1982).

[22] M. A. Dunn and J. N. Ross, "The argon ion laser," Prog. Quantum Electron. **4**, 233 (1976).

[23] H. Daido, "Review of soft x-ray laser researches and developments," Rep. Prog. Phys. **65**, 1513–1576 (2002).

[24] Y. V. Afanas'ev and V. N. Shlyaptsev, "Formation of a population inversion of transitions in Ne-like ions in steady-state and transient plasmas," Sov. J. Quantum Electron. **19**, 1606–1612 (1989).

[25] P. V. Nickles, V. N. Shlyaptsev, M. Kalachnikov, M. Schnürer, I. Will, and W. Sandner, "Short pulse x-ray laser at 32.6 nm based on transient gain in ne-like titanium," Phys. Rev. Lett. **78**, 2748–2751 (1997).

[26] J. Dunn, A. L. Osterheld, R. Shepherd, W. E. White, V. N. Shlyaptsev, and R. E. Stewart, "Demonstration of x-ray amplification in transient gain nickel-like palladium scheme," Phys. Rev. Lett. **80**, 2825–2828 (1998).

[27] M. P. Kalachnikov, P. V. Nickles, M. Schnurer, W. Sandner, V. N. Shlyaptsev, C. Danson, D. Neely, E. Wolfrum, J. Zhang, A. Behjat, A. Demir, G. J. Tallents, P. J. Warwick, and C. L. S. Lewis, "Saturated operation of a transient collisional x-ray laser," Phys. Rev. A **57**, 4778–4783 (1998).

[28] R. E. King, G. J. Pert, S. P. McCabe, P. A. Simms, A. G. MacPhee, C. L. S. Lewis, R. Keenan, R. M. N. O. G. J. Tallents, S. J. Pestehe, F. Strati, D. Neely, and R. Allott, "Saturated x-ray lasers at 196 and 73 Å, pumped by a picosecond traveling-wave excitation," Phys. Rev. A **64**, 053,810 (2001).

[29] P. B. Corkum and N. H. Burnett, in "Short-Wavelength Coherent Radiations: Genearion and Applications," , vol. 2, R. W. Falcone and J. Kirz, eds. (OSA, 1988), vol. 2, p. 225.

[30] V. N. Shlyaptsev, J. Dunn, S. Moon, R. Smith, R. Keenan, J. Nilsen, K. Fournier, J. Kuba, A. L. Osterheld, J. J. G. Rocca, B. M. Luther, Y. Wang, , and M. C. Marconi, in "Numerical studies of transient and capillary x-ray lasers and their applications," , vol. 5197 of *Proc. SPIE* (2003), vol. 5197 of *Proc. SPIE*, p. 221.

[31] R. Keenan, J. Dunn, P. K. Patel, D. F. Price, R. F. Smith, and V. N. Shlyaptsev, "High-repetition-rate grazing-incidence pumped x-ray laser operating at 18.9 nm," Phys. Rev. Lett. **94**, 103,901 (2005).

[32] J. J. Rocca, V. Shlyaptsev, F. G. Tomasel, O. D. Cortázar, D. Hartshorn, and J. L. A. Chilla, "Demonstration of a discharge pumped table-top soft-x-ray laser," Phys. Rev. Lett. **73**, 2192–2195 (1994).

[33] R. J. J, D. P. Clark, J. L. A. Chilla, and V. N. Shlyaptsev, "Energy extraction and achievement of the saturation limit in a discharge-pump table-top soft x-ray amplifier," Phys. Rev. Lett. **77**, 1476–1479 (1996).

[34] L. I. Gudzenko and L. A. Shelepin, Sov. Phys. Doki. **10**, 147 (1965).

[35] G. J. Pert, "Models of collitional-radiative recombination," J. Phys. B **23**, 619–650 (1990).

[36] S. Suckewer and P. Jaeglé, "X-ray laser: past, present, and future," Laser Phys. Lett. **6**, 411–436 (2009).

[37] Y. Nagata, K. Midorikawa, S. Kubodera, M. Obara, H. Tashiro, and K. Toyoda, "Soft-x-ray amplification of the Lyman-α transition by optical-field-induced ionization," Phys. Rev. Lett. **71**, 3774–3777 (1993).

[38] D. V. Korobkin, C. H. Nam, and S. Suckewer, "Demonstration of soft x-ray lasing to ground state in Li III," Phys. Rev. Lett. **77**, 5206–5209 (1996).

[39] B. E. Lemoff, C. P. J. Barty, and S. E. Harris, "Femtosecond-pulse-driven, electron-excited XUV lasers in eight-times-ionized noble gases," Opt. Lett. **19**, 569–571 (1994).

[40] B. E. Lemoff, G. Y. Yin, C. L. Gordon III, C. P. J. Barty, and S. E. Harris, "Demonstration of a 10-Hz femtosecond-pulse-driven XUV laser at 41.8 nm in Xe IX," Phys. Rev. Lett. **74**, 1574–1577 (1995).

[41] H.-H. Chu, H.-E. Tsai, M.-C. Chou, L.-S. Yang, J.-Y. Lin, C.-H. Lee, J. Wang, and S.-Y. Chen, "Collisional excitation soft x-ray laser pumped by optical field ionization in a cluster jet," Phys. Rev. A **71**, 061,804 (2005).

[42] M.-C. Chou, P.-H. Lin, T.-S. Hung, J.-Y. Lin, J. Wang, and S.-Y. Chen, "Experimental investigation of the parameter space for optical-field-ionization cluster-jet x-ray lasers," Phys. Rev. A **74**, 023,804 (2006).

[43] S. Sebban, R. Haroutunian, P. Balcou, G. Grillon, A. Rousse, S. Kazamias, T. Marin, J. P. Rousseau, L. Notebaert, M. Pittman, J. P. Chambaret, A. Antonetti, D. Hulin, D. Ros, A. Klisnick, A. Carillon, P. Jaeglé, G. Jamelot, and J. F. Wyart, "Saturated amplification of a collisionally pumped optical-field-ionization soft x-ray laser at 41.8 nm," Phys. Rev. Lett. **86**, 3004–3007 (2001).

[44] A. Butler, A. J. Gonsalves, C. M. McKenna, D. J. Spence, S. M. Hooker, S. Sebban, T. Mocek, I. Bettaibi, and B. Cros, "Demonstration of a collisionally excited optical-field-ionization xuv laser driven in a plasma waveguide," Phys. Rev. Lett. **91**, 205,001 (2003).

[45] A. Butler, A. J. Gonsalves, C. M. McKenna, D. J. Spence, S. M. Hooker, S. Sebban, T. Mocek, I. Betttaibi, and B. Cros, "41.8-nm Xe^{8+} laser driven in a plasma waveguide," Phys. Rev. A **70**, 023,821 (2004).

[46] T. Mocek, C. M. McKenna, B. Cros, S. Sebban, D. J. Spence, G. Maynard, I. Bettaibi, V. Vorontsov, A. J. Gonsavles, and S. M. Hooker, "Dramatic enhancement of xuv laser output using a multimode gas-filled capillary waveguide," Phys. Rev. A **71**, 013,804 (2005).

[47] T. Mocek, S. Sebban, I. Bettaibi, P. Zeitoun, G. Faivre, B.Cros, G. Maynard, A. Butler, C. M. McKenna, D. J. Spence, A. J. Gonsavles, S. M. Hooker, V. Vorontsov, S. Hallou, M. Fajardo, S. Kazamias, S. L. Pape, P. Mercére, A. S. Morlens, C. valentin, and P. Balcou, "Progess in optical-field-ionization soft x-ray lasers at LOA," Laser Part. Beams **23**, 351–356 (2005).

[48] B. Cros, T. Mocek, I. Bettaibi, G. Vieux, M. Farinet, J. Dubau, S. Sebban, and G. Maynard, "Characterization of the collisionally pumped optical-field-ionized soft-x-ray laser at $41.8nm$ driven in capillary tubes," Phys. Rev. A **73**, 033,801 (2006).

[49] C. G. Durfee III, J. Lynch, and H. M. Milchberg, "Development of plasma waveguide for high-intensity laser pulses," Phys. Rev. E **51**, 2368–2389 (1995).

[50] P. Volfbeyn, E. Esarey, and W. P. Leemans, "Guiding of laser pulses in plasma channels created by the ignitor-heater technique," Phys. Plasmas **6**, 2269–2277 (1999).

[51] Y.-F. Xiao, H.-H. Chu, H.-E. Tsai, C.-H. Lee, J.-Y. Lin, J. Wang, and S.-Y. Chen, "Efficient generation of extended plasma waveguides with the axicon ignitor-heater scheme," Phys. Plasmas **11**, L21–L24 (2004).

[52] H. M. Milchberg, C. G. Durfee III, and J. Lynch, "Application of a plasma waveguide to soft-x-ray lasers," J. Opt. Soc. Am. B **12**, 731–737 (1995).

[53] M.-C. Chou, P.-H. Lin, C.-A. Lin, J.-Y. Lin, J. Wang, and S.-Y. Chen, "Dramatic enhancement of optical-field-ionization collisional-excitation x-ray lasing by an optically preformed plasma waveguide," Phys. Rev. Lett. **99**, 063,904 (2007).

[54] P.-H. Lin, M.-C. Chou, C.-A. Lin, H.-H. Chu, J.-Y. Lin, J. Wang, and S.-Y. Chen, "Optical-field-ionization collisional-excitation x-ray lasers with an optically preformed plasma waveguide," Phys. Rev. A **76**, 053,817 (2007).

[55] L. V. Keldysh, "Ionization in the field of a strong electromagnetic wave," Sov. Phys. JETP **20**, 1307–1314 (1965).

[56] P. B. Corkum, N. H. Burnett, and F. Brunel, "Above-threshold ionization in the long wavelength limit," Phys. Rev. Lett. **62**, 1259–1262 (1989).

[57] N. H. Burnett and P. B. Corkum, "Cold-plasma production for recombination extreme-ultraviolet lasers by optical-field-induced ionization," J. Opt. Soc. Am. B **6**, 1195–1199 (1989).

[58] L. D. Landau and E. M. Lifshitz, *Quantum Mechanics* (Pergamon, London, 1978).

[59] A. M. Perelomov, V. S. Popov, and M. V. Terent'ev, "Ionization of atoms in an alternating electric field," Sov. Phys. JETP **23**, 924–928 (1965).

[60] M. V. Ammosov, N. B. Delone, and V. P. Krainov, "Tunnel ionization of complex atoms and atomic ions in an alternating electromagnetic field," Sov. Phys. JETP **64**, 1191–1196 (1986).

[61] T. Tajima and J. M. Dawson, "Optimization of laser propagation in optical-field-ionization plasmas for x-ray laser generation," Phys. Rev. Lett. **43**, 267–270 (1979).

[62] C. G. Wahlstrom, S. Borgstrom, J. Larsson, and S. G. Pettersson, "High order harmonic generation in laser-produced ions using a near-infrared laser," Phys. Rev. A **51**, 585–591 (1995).

[63] P. E. Young, H. A. Baldis, R. P. Drake, E. M. Campbell, and K. G. Estabrook, "Direct evidence of poderomotive filamentation in a laser-produced plasma," Phys. Rev. Lett. **61**, 2336–2339 (1988).

[64] A. Braun, G. Korn, X. Liu, D. Du, J. Squier, and G. Mourou, "Self-channeling of high-peak-power femtosecond laser pulses in air," Opt. Lett. **20**, 73–75 (1995).

[65] W. L. Kruer, *The physics of laser plasma interactions* (Addison-Wesley Publishing Company, 1988).

[66] C. D. Decker, W. B. Mori, J. M. Dawson, and T. Katsouleas, "Non-linear collisional absorption in laser-driven plasmas," Phy. Plasma **1**, 4032–4042 (1994).

[67] J. H. Mcleod, "The axicon: A new type of optical element," J. Opt. Soc. Am. **44**, 592–597 (1954).

[68] V. V. Korobkin, L. Y. Polonskii, V. P. Poponin, and L. N. Pyatnitskii, "Focusing of Gaussian and super-Gaussian laser beams by axicons to obtain continuous laser sparks," Sov. J. Quantum Electron. **16**, 178–182 (1986).

[69] A. G. Sedukhin, "Beam-preshaping axicon focusing," J. Opt. Soc. Am. A **15**, 3057–3066 (1998).

[70] H. N. Tsai, "The preliminary development of x-ray lasers driven in plasma waveguides," Master Thesis - National Taiwan University (2005).

[71] M. C. Chou, "Experimental study of optical-field-ionization collisional-excitation soft x-ray lasers," Ph.D. Thesis - National Chung Cheng University (2007).

[72] T. Kita, T. Harada, N. Nakano, and H. Kuroda, "Mechanically ruled aberration-corrected concave gratings for a flat-field grazing-incidence spectrograph," Appl. Opt. **22**, 512–513 (1983).

[73] N. Nakano, H. Kuroda, T. Kita, and T. Harada, "Development of a flat-field grazing-incidence xuv spectrometer and its application in picosecond xuv spectroscopy," Appl. Opt. **23**, 2386–2392 (1984).

[74] J. Y. Lin, "Optimization of laser propagation in optical-field-ionization plasmas for x-ray laser generation," Appl. Phys. B **86**, 25–29 (2007).

[75] K. A. Goldberg, P. Naulleau, P. Denham, S. B. Rekawa, K. Jackson, E. H. Anderson, and J. A. Liddle, "At-wavelength alignment and testing of the 0.3 NA MET optics," J. Vac. Sci. Tech. B **22**, 2956–2961 (2004).

[76] Y. Liu, A. Barty, E. Gullikson, J. S. Taylor, J. A. Liddle, and O. Wood, "A dual-mode actinic euv mask inspection tool," in "Proc. SPIE in Emerging Lithographic Technologies IX," (2005), pp. 660–669.

[77] W. Chao, B. D. Harteneck, J. A. Liddle, E. H. Anderson, and D. T. Attwood, "Soft x-ray microscopy at a spatial resolution better than 15 nm," Nature **435**, 1210–1213 (2005).

[78] M. C. Marconi, J. L. A. Chilla, C. H. Moreno, B. R. Benware, and J. J. Rocca, "Measurement of the spatial coherence buildup in a discharge pumped table-top soft x-ray laser," Phy. Rev. Lett. **79**, 2799–2802 (1997).

[79] J. Yang, D. Fan, S. Wang, and Y. Gu, "Moiré technique for spatial coherence measurements of soft-x-ray lasers," J. Opt. Soc. Am. A **17**, 790–793 (2000).

[80] R. A. Bartels, A. Paul, H. Green, H. C. Kapteyn, M. M. Murnane, S. Backus, I. P. Christov, Y. Liu, D. Attwood, and C. Jacobsen, "Generation of spatially coherent light at extreme ultraviolet wavelengths," Science **4297**, 376–378 (2002).

[81] Y. Liu, Y. Wang, M. A. Larotonda, B. M. Luther, J. J. Rocca, and D. T. Attwood, "Spatial coherence measurements of a 13.2 nm transient nickel-like cadmium soft x-ray laser pumped at grazing incidence," Opt. Exp. **14**, 12,872–12,879 (2006).

[82] P. Zeitoun, G. Faivre, S. Sebban, T. Mocek, A. Hallou, M. Fajardo, D. Aubert, P. Balcou, F. Burgy, D. Douillet, S. Kazamias, G. de Lacheźe-Murel, T. Lefrou, S. le Pape, P. Mercére, H. Merdji, A. S. Morlens, J. P. Rousseau, and C. Valentin1, "A high-intensity

highly coherent soft x-ray femtosecond laser seeded by a high harmonic beam," Nature **431**, 426–429 (2004).

[83] B. J. Thompson and E. Wolf, "Two-beam interference with partially coherent light," J. Opt. Soc. Am. **47**, 895–902 (1957).

[84] H. A. Bethe and E. E. Salpeter, *Quantum Mechanics of One- and Two-Electron Atoms* (Plenum, New York, 1977).

[85] S. Augst, D. Strickland, D. D. Meyerhofer, S. L. Chin, and J. H. Eberly, "Tunneling ionization of noble gases in a high-intensity laser field," Phy. Rev. Lett. **63**, 2212–2215 (1989).

[86] B. M. Penetrante and J. N. Bardsly, "Residual energy in plasmas produced by intense subpicosecond lasers," Phys. Rev. A **43**, 3100–3113 (1991).

[87] *Calculated using atomic physics code, http://aphysics2.lanl.gov/cgi-bin/ION/runlanl08d.pl.*

[88] R. D. Cowan, *The Theory of Atomic Structure and Spectra* (University of California Press, 1981).

[89] M. J. Grout, K. A. Janulewicz, S. B. Healy, and G. J. Pert, "Optical-field induced gas mixture breakdown for recombination x-ray lasers," Opt. Commun. **141**, 213–220 (1997).

[90] H. Fiedorowicz, A. Bartnik, Y. Li, P. Lu, and E. Fill, "Demonstration of soft x-ray lasing with neonlike argon and nickel-like xenon ions using a laser-irradiated gas puff target," Phys. Rev. Lett. **76**, 415–418 (1996).

[91] J. Nilsen, H. Fiedorowicz, A. Bartnik, Y. Li, P. Lu, and E. E. Fill, "Self-photopumped neonlike x-ray laser," Opt. Lett. **21**, 408–410 (1996).

[92] J. Nilsen, "Lasing on the $3d \rightarrow 3p$ neonlike x-ray laser transitions driven by a self-photon-pumping mechanism," Phys. Rev. A **53**, 4539–4546 (1996).

[93] H. Fiedorowicz, A. Bartnik, J. Dunn, R. F. Smith, J. Hunter, J. Nilsen, A. L. Osterheld, and V. N. Shlyapsev, "Demonstration of a neonlike argon soft-x-ray laser with a picosecond-laser-irradiated gas puff target," Opt. Lett. **26**, 1403–1405 (2001).

[94] A. V. Vinogradov, I. I. Sobelman, and E. A. Yukov, "Possibility of constructing a far-ultraviolet laser utilizing transitions in multiply charged ions in an inhomogeneous plasma," Sov. J. Quantum Electron. **5**, 59–63 (1975).

[95] B. Rus, C. L. S. Lewis, G. F. Cairns, P. Dhez, P. Jaeglé, M. H. Key, D. Neely, A. G. MacPhee, S. A. Ramsden, C. G. Smith, and A. Sureau, "Demonstration of amplification of a polarized soft-x-ray laser beam in a neonlike germanium plasma," Phys. Rev. A **51**, 2316–2327 (1995).

[96] T. Mocek, S. Sebban, G. Maynard, P. Zeitoun, G. Faivre, A. Hallou, M. Fajardo, S. Kazamias, B. Cros, D. Aubert, G. de Lachéze-Murel, J. P. Rousseau, and J. Dubau, "Absolute time-resolved x-ray laser gain measurement," Phys. Rev. Lett. **95**, 173,902 (2005).

[97] A. Klisnick, J. Kuba, D. Ros, R. Smith, G. Jamelot, C. Chenais-Popovics, R. Keenan, S. J. Topping, C. L. S. Lewis, F. Strati, G. J. Tallents, D. Neely, R. Clarke, J. Collier, A. G. MacPhee, F. Bortolotto, P. V. Nickles, and K. A. Janulewicz, "Demonstration of a 2-ps transient x-ray laser," Phys. Rev. A **65**, 033,810 (2002).

[98] M. Nishikino, M. Tanaka, K. Nagashima, M. Kishimoto, M. Kado, T. Kawachi, K. Sukegawa, Y. Ochi, N. Hasegawa, and Y. Kato, "Demonstration of a soft-x-ray laser at 13.9 nm with full spatial coherence," Phys. Rev. A **68**, 061,802(R) (2003).

[99] P. Saliéres, T. Ditmire, K. S. Budil, M. D. Perry, and A. LHuillier, "Spatial profiles of high-order harmonics generated by a femtosecond Cr:LiSAF laser," J. Phys. B **27**, L217–L222 (1994).

[100] T. Ditmire, M. H. R. Hutchinson, M. H. Key, C. L. S. Lewis, A. MacPhee, I. Mercer, D. Neely, M. D. Perry, R. A. Smith, J. S. Wark, and M. Zepf, "Amplification of xuv harmonic radiation in a gallium amplifier," Phys. Rev. A **51**, R4337–R4340 (1995).

[101] J. P. Goddet, S. Sebban, A. S. Morlens, J. Gautier, J. P. Rosseau, F. Burgy, P. Zeitoun, C. Valentin, , C. Hauri, G. Maynard, A. Boudaa, J. P. Caumes, H. Merdji, T. Mocek, M. Kozlova, and K. Jakubczak, "Demonstration of a spatial filtering amplifier for high-order harmonics," Opt. Lett. **32**, 1498–1500 (2007).

[102] Y. Wang, E. Granados, M. A. Larotonda, M. Berrill, B. M. Luther, D. Patel, C. S. Menoni, and J. J. Rocca, "High-brightness injection-

seeded soft-x-ray-laser amplifier using a solid target," Phys. Rev. Lett. **97**, 123,901 (2006).

[103] Y. Wang, E. Granados, F. Pedaci, D. Alessi, B. Luther, M. Berrill, and J. J. Rocca, "Phase-coherent, injection-seeded table-top soft-x-ray lasers at 18.9 nm and 13.9 nm," Nat. Photonics **2**, 94–98 (2008).

[104] M. B. B. L. E. G. F. Pedaci, Y. Wang and J. J. Rocca, "Highly coherent injection-seeded 13.2 nm tabletop soft x-ray laser," Opt. Lett. **31**, 491–493 (2008).

[105] I. R. Al'miev, O. Larroche, D. Benredjem, J. Dubau, S. Kazamias, C. Moeller, and A. Klisnick, "Dynamical description of transient x-ray lasers seeded with high-order harmonic radiation through Maxwell-Bloch numerical simulations," Phys. Rev. Lett. **99**, 123,902 (2007).

[106] H. Huang and G. J. Tallents, "The output of a laser amplifier with simultaneous amplified spontaneous emission and an injected seed," Laser Part. Beams **27**, 393–398 (2009).

[107] P. B. Corkum, "Plasma perspective on strong field multiphoton ionization," Phys. Rev. Lett. **71**, 1994–1997 (1993).

[108] K. C. Kulander, K. J. Schafer, and J. L. Krause, *Dynamics of Short-Pulse Excitation, Ionization and Harmonic Conversion.*

[109] M. Lewenstein, P. Balcou, M. Y. Ivanov, A. L'Huillier, and P. B. Corkum, "Theory of high-harmonic generation by low-frequency laser fields," Phys. Rev. A **49**, 2117–2132 (1994).

[110] P. Saliéres, T. Ditmire, M. D. Perry, A. L'Huillier, and M. Lewenstein, "Angular distributions of high-order harmonics generated by a femtosecond laser," J. Phys. B: At. Mol. Opt. Phys. **29**, 4771–4786 (1996).

[111] Y. Tamaki, J. Itatani, M. Obara, and K. Midorikawa, "Optimization of conversion efficiency and spatial quality of high-order harmonic generation," Phys. Rev. A **62**, 063,802 (2000).

[112] T. Ditmire, E. T. Gumbrell, R. A. Smith, J. W. G. Tisch, D. D. Meyerhofer, and M. H. R. Hutchinson, "Spatial coherence measurement of soft x-ray radiation produced by high order harmonic generation," Phys. Rev. Lett. **77**, 4756–4759 (1996).

[113] T. Ditmire, J. Tisch, E. Gumbrell, R. Smith, D. Meyerhofer, and M. Hutchinson, "Spatial coherence of short wavelength high-order harmonics," Appl. Phys. B **65**, 313–328 (1997).

[114] K.-H. H. J.-H. K. I. W. C. H. T. Kim, D. G. Lee and C. H. Nam, "Continuously tunable high-order harmonics from atoms in an intense femtosecond laser field," Phys. Rev. A **67**, 051,801(R) (2003).

[115] T. Brabec and F. Krausz, "Intense few-cycle laser fields: Frontiers of nonlinear optics," Rev. Mod. Phys. **72**, 545–591 (2000).

[116] C. Altucci, R. Bruzzese, C. de Lisio, M. Nisoli, S. Stagira, S. De Silvestri, O. Svelto, A. Boscolo, P. Ceccherini, L. Poletto, G. Tondello, and P. Villoresi, "Tunable soft-x-ray radiation by high-order harmonic generation," Phys. Rev. A **61**, 021,801 (1999).

[117] Z. Fangchuan, L. Zhong, Z. Zhinan, Z. Zhengquan, L. Ruxin, and X. Zhizhan, "Spectral splitting of high-order harmonic emissions from ionizing gases," Phys. Rev. A **65**, 033,808 (2002).

[118] H. J. Shin, D. G. Lee, Y. H. Cha, K. H. Hong, and C. H. Nam, "Generation of nonadiabatic blueshift of high harmonics in an intense femtosecond laser field," Phys. Rev. Lett. **83**, 2544–2547 (1999).

[119] X. He, M. Miranda, J. Schwenke, O. Guilbaud, T. Ruchon, C. Heyl, E. Georgadiou, R. Rakowski, A. Persson, M. B. Gaarde, and A. L'Huillier, "Spatial and spectral properties of the high-order harmonic emission in argon for seeding applications," Phys. Rev. A **79**, 063829 (2009).

[120] A. T. Friberg and J. Turunen, "Imaging of gaussian schell-model sources," J. Opt. Soc. Am. A **5**, 713–720 (1988).

[121] S. Sebban, T. Mocek, D. Ros, L. Upcraft, P. Balcou, R. Haroutunian, G. Grillon, B. Rus, A. Klisnick, A. Carillon, G. Jamelot, C. Valentin, A. Rousse, J. P. Rousseau, L. Notebaert, M. Pittman, and D. Hulin, "Demonstration of a Ni-like Kr optical-field-ionization collisional soft x-ray laser at 32.8 nm," Phys. Rev. Lett. **89**, 253,901 (2002).

[122] P.-H. Lin, M.-C. Chou, M.-J. Jiang, P.-C. Tseng, H.-H. Chu, J.-Y. Lin, J. Wang, and S. yuan Chen, "Seeding of a soft-x-ray laser in a plasma waveguide by high harmonic generation," Opt. Lett. **34**, 3562–3564 (2009).

[123] B. M. Luther, Y. Wang, M. A. Larotonda, D. Alessi, M. Berrill, M. C. Marconi, J. J. Rocca, and V. N. Shlyaptsev, "Saturated high-repetition-rate 18.9-nm tabletop laser in nicke-llike molybdenum," Opt. Lett. **30**, 165–167 (2005).

[124] Y. Wang, M. A. Larotonda, B. M. Luther, D. Alessi, M. Berrill, V. N. Shlyaptsev, and J. J. Rocca, "Demonstration of high-repetition-rate tabletop soft-x-ray lasers with saturated output at wavelengths down to 13.9 nm and gain down to 10.9 nm," Phys. Rev. A **72**, 053,807 (2005).

[125] J. J. Rocca, Y. Wang, M. A. Larotonda, B. M. Luther, M. Berrill, and D. Alessi, "Saturated 13.2 nm high-repetition-rate laser in nickellike cadmium," Opt. Lett. **30**, 2581–2583 (2005).

[126] H. Eichmann, A. Egbert, S. Nolte, C. Momma, B. Wellegehausen, W. Becker, S. Long, and J. K. McIver, "Polarization-dependent high-order two-color mixing," Phys. Rev. A **51**, R3414–R3417 (1995).

[127] D. B. Milošević, W. Becker, and R. Kopold, "Generation of circularly polarized high-order harmonics by two-color coplanar field mixing," Phys. Rev. A **61**, 063,403 (2000).

[128] S. Hulin, T. Auguste, P. D'Oliveira, P. Monot, S. Jacquemot, L. Bonnet, and E. Lefebvre, "Soft-x-ray laser scheme in a plasma created by optical-field-induced ionization of nitrogen," Phys. Rev. E **61**, 5693–5700 (2000).

[129] P. Lu, T. Kawachi, M. Kishimoto, K. Sukegawa, M. Tanaka, N. Hasegawa, M. Suzuki, R. Tai, M. Kado, K. Nagashima, H. Daido, and Y. Kato, "Demonstration of a transient-gain nickel-like xenon-ion x-ray laser," Opt. Lett. **27**, 1911–1913 (2002).